

Radiation Damage Effects and Performance of Silicon Strip Detectors using LHC Readout Electronics

ausgeführt am Europäischen Zentrum für Teilchenphysik CERN, Genf

von

Petra Riedler

DISSERTATION

zur Erlangung eines Grades des Doktors der
Naturwissenschaften

Universität Wien
Oktober 1998

Abstract

Future high energy physics experiments as the ATLAS experiment at CERN, will use silicon strip detectors for fast and high precision tracking information. The high hadron fluences in these experiments cause permanent damage in the silicon. Additional energy levels are introduced in the bandgap thus changing the electrical properties such as leakage current and full depletion voltage V_{fd} . Very high leakage currents are observed after irradiation and lead to higher electronic noise and thus decrease the spatial resolution. V_{fd} increases to a few hundred volts after irradiation and eventually beyond the point of stable operating voltages.

Prototype detectors with either p-implanted strips (p-in-n) or n-implanted strips (n-in-n) were irradiated to the maximum expected fluence in ATLAS. The irradiation and the following study of the current and V_{fd} were carried out under ATLAS operational conditions. The evolution of V_{fd} after irradiation is compared to models based on diode irradiations. The qualitative behaviour of V_{fd} as a function of time is well described by these models although quantitative differences are observed between the different detectors. For the first time an annealing study is carried out on full size detectors showing that compared to diodes additional effects have to be taken into account. These properties include surface effects, geometric effects and process parameters.

Measurements of V_{fd} on irradiated detectors show a temperature and frequency dependence indicating an influence of deep radiation induced damage levels. The obtained value of V_{fd} after irradiation can no longer be regarded as an absolute value due to the temperature and frequency dependence.

The leakage current after irradiation is dominated by bulk effects. Although currents from the edge regions are much smaller than from the active area, guard rings are necessary to allow stable operation at high voltages after irradiation. It is shown that full size detectors with optimised guard ring design allow stable operation up to more than 400 V after irradiation. Parameters influencing the the guard ring performance before irradiation are illustrated on prototype detectors.

In general no systematic difference between p-in-n and n-in-n detectors in leakage current, stability and the time dependence of V_{fd} is observed during this study. These results and the results from a testbeam with these detectors led to the change of the ATLAS detector baseline from n-in-n to p-in-n detectors.

Non-irradiated and irradiated prototype detectors connected to fast analogue frontend electronics designed for LHC are tested with β -sources and in a pion-testbeam. They show full functionality even after irradiation to the maximum expected fluence in ATLAS. At V_{fd} the observed signal to noise ratio (S/N) has not saturated which is attributed to the ballistic deficit caused by charge collection times in the order of the shaping time of the readout electronics. A calculation of the S/N increase after depletion as a function of charge collection time is in good agreement with the data. Between irradiated and non-irradiated detectors a decrease in S/N is observed. At sufficiently high voltages above V_{fd} the difference is explained by a noise increase due to higher leakage current while just above V_{fd} less signal is registered. The results presented illustrate that even after the maximum expected fluence ATLAS prototype detectors can be operated efficiently with LHC readout electronics.

Kurzfassung

Zukünftige Hochenergie-Experimente, wie zum Beispiel das ATLAS Experiment am CERN verwenden Silizium-Streifendetektoren aufgrund der schnellen Ladungssammelzeit und der extrem guten Ortsauflösung zur Spurrekonstruktion. Die hohe Strahlenbelastung, insbesondere durch Hadronen, in diesen Experimenten verursacht permanente Strahlenschäden im Silizium. Zusätzliche Energieniveaus werden in der Bandlücke induziert und verursachen eine Änderung der elektrischen Eigenschaften. Nach der Bestrahlung beobachtet man einen starken Anstieg des Leckstromes, der wiederum zu höherem elektronischen Rauschen führt. Die Verarmungsspannung V_{fd} steigt durch die Bestrahlung auf einige Hundert Volt an.

Detektor Prototypen mit p-implantierten (p-in-n) und n-implantierten (n-in-n) Streifen wurden zur maximal erwarteten Fluenz in ATLAS bestrahlt. Die Bestrahlung und die darauffolgende Studie des Leckstromes und von V_{fd} wurden unter den für ATLAS vorgesehenen Betriebsbedingungen ausgeführt. Der zeitliche Verlauf von V_{fd} nach der Bestrahlung wird mit Modellen verglichen, die auf den Daten von Dioden-Bestrahlungen beruhen. Das qualitative Verhalten von V_{fd} wird von diesen Modellen sehr gut beschrieben, wenn gleich auch quantitative Unterschiede zwischen den einzelnen Detektoren beobachtet werden. Zum ersten Mal wurde eine solche Studie an Prototyp Strip-Detektoren ausgeführt. Es zeigt sich, daß im Vergleich zu den Modellen und Daten der Dioden-Bestrahlungen, noch weitere Effekte in Betracht genommen werden müssen. Dazu gehören Oberflächen-Effekte, geometrische Effekte und Parameter des Herstellungsprozesses.

Messungen von V_{fd} an bestrahlten Detektoren sind temperatur- und frequenzabhängig, was auf den Einfluß von strahlungsinduzierten Energieniveaus in der Nähe der Bandmitte zurückzuführen ist. Aufgrund dieser Abhängigkeit kann der gemessene Wert von V_{fd} nicht mehr als Absolutwert betrachtet werden.

Nach der Bestrahlung ist der Leckstrom dominiert von Volumeffekten. Ströme von den Rändern sind im allgemeinen viel kleiner als aus dem Bereich des aktiven Volumens. Die Verwendung von Guard-Ringen ist für einen stabilen Betrieb extrem wichtig. Es wird gezeigt, daß Detektoren mit optimiertem Guard-Ring Design über 400 V hinaus stabil betrieben werden können. Verschiedene für die Funktionalität der Guard-Ringe verantwortlichen Parameter werden anhand von Messungen an Prototyp-Detektoren besprochen.

Im allgemeinen konnte kein systematischer Unterschied im Strom, der Stabilität und dem zeitlichen Verlauf von V_{fd} zwischen p-in-n und n-in-n Detektoren gefunden werden. Dieses Resultat und die Ergebnisse von einem Testbeam führten unter anderem dazu, daß das ATLAS Detektor-Design von n-in-n auf p-in-n Detektoren geändert wurde.

Bestrahlte und nicht-bestrahlte Prototyp-Detektoren wurden mit für LHC entwickelter analoger Ausleseelektronik getestet. Die Detektoren bleiben auch nach Bestrahlung zur maximal erwarteten Fluenz voll betriebsfähig. Auch nach voller Verarmung des Detektors steigt das Signal zu Rausch Verhältnis (S/N) weiter an. Die Ursache dafür ist das ballistische Defizit, das bei Ladungssammelzeiten im Bereich der charakteristischen Anstiegszeit des Verstärkers auftritt. Eine Berechnung des S/N-Anstiegs für Spannungen größer als V_{fd} als Funktion der Ladungssammelzeit ist in guter Übereinstimmung mit den Messdaten. Der Vergleich zeigt eine Verringerung von S/N beim bestrahlten Detektor. Bei Spannungen weit über V_{fd} ist der Unterschied auf höheres elektronisches Rauschen zurückzuführen, verursacht durch einen höheren Leckstrom. Bei geringeren Spannungen wird zusätzlich weniger Signal registriert. Die präsentierten Ergebnisse zeigen, daß auch nach Bestrahlung die ATLAS Prototyp-Detektoren mit LHC Ausleseelektronik effizient betrieben werden können.

Contents

1	Introduction	1
1.1	Experiments at the LHC	2
1.2	Silicon Detectors in LHC Experiments	4
1.3	Radiation Environment in the ATLAS Inner Detector	6
2	Silicon Strip Detectors	11
2.1	Current Voltage Characteristics	12
2.2	Capacitance Voltage Characteristics	15
2.3	Silicon Strip Detectors	17
2.3.1	Process and Layout of Silicon Strip Detectors	17
2.4	Setup for Static Measurements	23
2.4.1	Leakage Current Measurements	24
2.4.2	Capacitance Measurements	25
3	Radiation Damage in Silicon	27
3.1	The NIEL Hypothesis	28
3.2	Surface Damage	30
3.3	Changes in Detector Properties	31
3.3.1	Leakage Current	32
3.3.2	Effective Doping and Full Depletion Voltage	34
3.3.3	Interstrip Resistance	38
3.3.4	Interstrip Capacitance	38
3.3.5	Bias Resistors	39
3.4	Radiation Damage Models	39
3.4.1	The Hamburg Model	39
3.4.2	The Ziock-Parameterisation	41
3.5	Results from ATLAS Prototype Detectors	44
3.5.1	Detector Baseline	44
3.5.2	Pre-Irradiation Results and Detector Irradiation	46
3.5.3	Annealing Study of Irradiated Prototype Detectors	50
3.5.4	Conclusions	69

4	Frontend Readout Systems for ATLAS	71
4.1	Charge Collection and Signal Readout	72
4.1.1	Charge Sensitive Preamplifier	79
4.1.2	Ballistic Deficit	84
4.1.3	Spatial Resolution and Noise	86
4.2	Readout Systems	89
4.3	Analog and Binary Readout Systems	90
4.3.1	Analog Readout	90
4.3.2	Binary Readout	92
4.4	The SCT32A Analog Frontend Chip	93
4.4.1	SCT-A Layout and Functionality	93
4.4.2	Noise Performance	97
4.4.3	Source- and Pulse-Setup for the SCT32A in the Labor- atory	98
4.5	Results from an ATLAS prototype detector using the SCT32A	102
4.5.1	Source Tests	104
4.5.2	Testbeam Results	110
4.6	Source tests with an irradiated ATLAS prototype detector using the SCT32A	118
4.7	Conclusions	126
A	Basic Properties of Silicon Detectors	129
A.1	Intrinsic and Doped Silicon	130
A.2	The p-n Junction	133
B	Source Tests with Small Test Detectors	137
	Bibliography	147
	Acknowledgements	149

Chapter 1

Introduction

Contents

1.1 Experiments at the LHC	2
1.2 Silicon Detectors in LHC Experiments	4
1.3 Radiation Environment in the ATLAS Inner Detector	6

Collider experiments such as the **L**arge **E**lectron **P**ositron accelerator (LEP) experiments, have led to a more detailed investigation of the standard model. However, not all aspects of the standard model have been explained in existing experiments. The search for the Higgs boson whose existence explains the spontaneous symmetry breaking in the electroweak interaction is one of the aims of future experiments. As the production rate of the Higgs is very low, experiments are only feasible if the accelerator is operated at very high luminosities. The **L**arge **H**adron **C**ollider (LHC) at CERN (European Particle Physics Laboratory) is one of these future projects. It will be placed in the existing LEP tunnel at CERN and will collide proton beams at 14 TeV centre-of-mass energy every 25 ns. The initial luminosity will be 10^{33} particles $\text{cm}^{-2}\text{s}^{-1}$ being increased to 10^{34} particles $\text{cm}^{-2}\text{s}^{-1}$ after two years. Under these conditions it will be possible to study the origin of spontaneous symmetry breaking in the electroweak interaction of the standard model, to investigate heavy quarks such as the recently discovered top-quark and to test supersymmetric theories.

Using CERNs existing accelerator infrastructure to preaccelerate the particles, the superconducting structures of the LHC will accelerate two proton beams to 7-on-7 TeV. The beams will counter-rotate for several hours, colliding at the experimental sites until the beam quality degrades and the machine has to be refilled. To bend the 7 TeV beams with the radius of the existing LEP tunnel (~ 4.2 km), magnetic fields of 8.36 T are needed. Magnetic fields of this strength can only be produced over large volumes



Figure 1.1: Aerial view of the CERN site indicating LEP and the SPS accelerator rings, (CERN Photo Service).

by using superconducting magnets. The installation of the first dipoles is scheduled to start in 2002. In parallel the installation of the different experiments will be carried out so that the first physics runs are expected for the year 2005.

1.1 Experiments at the LHC

Four different experiments are planned for the LHC. Two general-purpose p - p detectors, **A Toroidal LHC ApparatuS** (ATLAS) and **Compact Muon Solenoid** (CMS), are planned to cover as many discoveries of the LHC as possible. Their layout is similar in the sense that they are both barrel type detectors with a multisubdetector system. However, both detectors have their special features. In the following a short characterisation of the experiments planned for LHC is given, with special emphasis on the ATLAS detector.

The CMS detector is based on a solenoid to optimise the muon detection system. It will be using a redundant muon system so that a muon track sees four stations over most of the solid angle. A superconducting solenoid will provide a 4 T magnetic field to guarantee good momentum resolution for high momentum muons. The 3 m radius of the solenoid will allow the full calorimetry to be located inside the solenoid. To detect the Higgs boson

via its two photon decay a precise electromagnetic calorimeter is needed. Due to the electromagnetic calorimeter being located inside the solenoid, electrons from W and Z decays can be used for in situ calibration providing high precision [1]. An inner detector consisting of silicon strip and pixel detectors and microstrip gas chambers will give information on primary and secondary vertices and provide points for the track reconstruction.

The overall concept for the ATLAS detector tries to optimise detection systems for both low and high luminosities [2, 3]. The detector will have a diameter of approximately 22 m and an overall length of about 42 m, see figure 1.2. A superconducting solenoid of 2.3 m diameter will provide a 2 T magnetic field. Large superconducting air-core toroids consisting of separate coils will be arranged in an eight-fold symmetry outside the calorimeters. Already at low luminosities the LHC will be a high rate beauty- and top-factory. The main emphasis in B -Physics is the precise measurement of CP-violation in the B -system, which at the moment can only be studied in kaon decays. This requires precise secondary vertex determination, provided by the inner detector, consisting of silicon strip and pixel detectors and transition radiation trackers (TRT). A more detailed description of the inner detector is given in section 1.3. The electromagnetic calorimeter (ECAL) is mainly used for good di-photon mass resolution of an intermediate Higgs decaying into two photons. In ATLAS the ECAL will be a liquid Argon calorimeter [2]. The hadron calorimeter (HCAL) surrounds the ECAL and acts in conjunction with it to measure the energies and directions of particle jets. In the barrel region the HCAL consists of iron absorbers with scintillator plates. At larger rapidity where higher radiation resistance is required, the HCAL is based on the use of liquid argon [2]. Outside the HCAL the muon detection system is installed to provide information on muons from Higgs, W , Z and $t\bar{t}$ and directly from p - p collisions [3].

A third experiment at LHC, LHC-B, is dedicated to the investigation of CP-violation and rare decays [3]. Although the observed CP violation in kaon decays can be accommodated in the standard model, there is evidence that it is partially or entirely due to new physics, a point which is also supported by cosmology [4]. The LHC-B experiment chose a forward geometry since the production of b -quarks is peaked in the forward direction.

The LHC will not only be able to accelerate proton beams, but also to collide heavy ions, such as lead, at a centre of mass energy of about 5.5 TeV/nucleon. The fourth experiment planned for the LHC, **A Large Ion Collider Experiment** (ALICE), is dedicated to study the physics of heavy ion collisions [5]. A main goal is to observe the quark-gluon plasma, a new phase of matter.

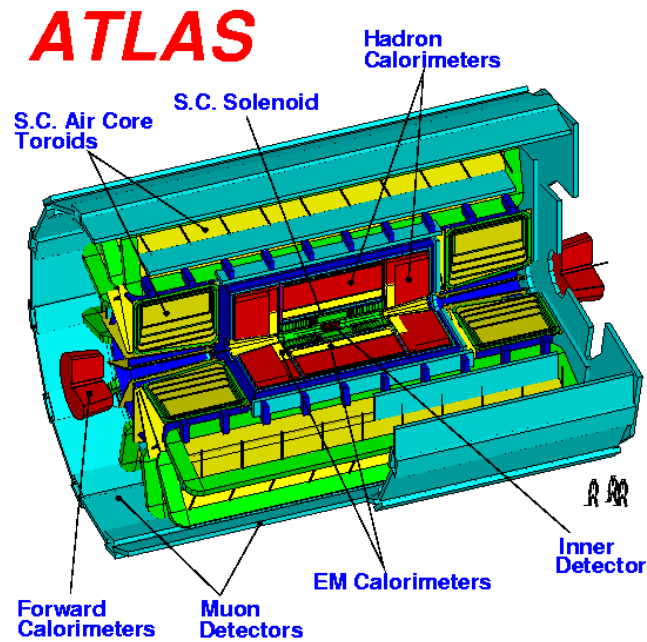


Figure 1.2: Schematic of the ATLAS detector at LHC.

1.2 Silicon Detectors in LHC Experiments

Silicon detectors are used in all four LHC experiments as tracking detectors, to provide fast, high precision information on space points. With their high granularity they are the ideal tool to directly observe the decay of heavy particles, such as the beauty or the top quark [6] via its beauty decay. Silicon diodes are usually implanted p-n junctions which are reversed biased to deplete the active volume from free charge carriers. When charged particles pass through the device electron-hole pairs are produced. The charge is moving in the electric field inducing a current signal on the electrodes of the device. This signal is then read out using amplifiers, see figure 1.3.

Figure 1.4 shows a picture of a prototype silicon strip detector developed for the ATLAS detector at CERN. In silicon strip detectors the p^+ electrode

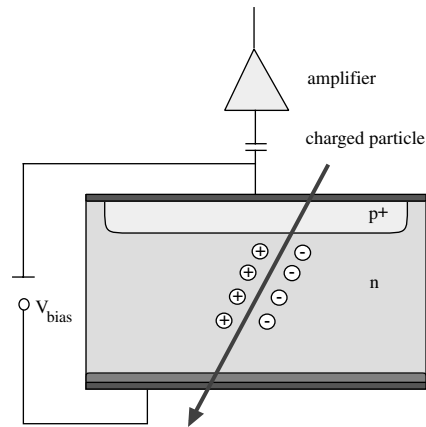


Figure 1.3: Schematic sketch of p-in-n detector.

is divided into parallel strips of approximately 10 to 20 μm width. Displayed are the different metal-lines on top of the highly p-doped strips in one corner of the detector. The rectangles are bonding pads to wire bond the individual strips to the input channels of a readout chip. A guard ring structure of highly p-implanted rings with metal on top is surrounding the strips. On this detector the pitch of the strips is 80 μm . A schematic cross-section of a strip detector is shown in figure 3.11 in chapter 3.

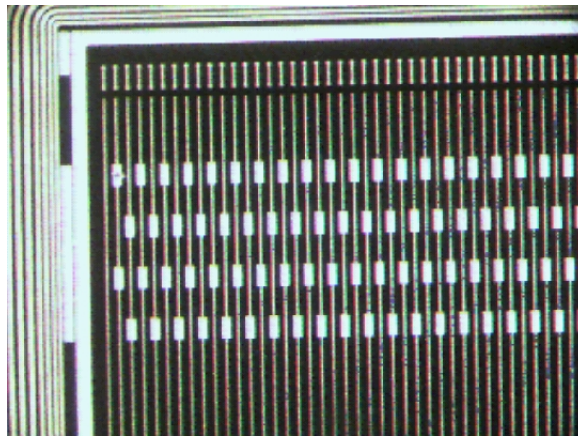


Figure 1.4: Picture of a prototype silicon strip detector developed for the ATLAS experiment.

A more detailed description of the functionality of a p-n junction and silicon strip detectors is given in the appendix A and chapter 2. Practically all high energy physics experiments use the advantages of silicon detectors

to improve their tracking information. In the following a few of these points are listed.

- Silicon detectors can be produced on thin wafers ($\sim 300 \mu\text{m}$). They add very little mass to the overall detector mass thus minimising multiple scattering.
- The energy needed to produce an electron-hole pair in silicon is approximately ten times smaller than in gaseous detectors.
- The time for the full charge to be collected at the electrodes is extremely small; e.g. in $300 \mu\text{m}$ well depleted silicon the collection time for electrons and holes is approximately 10-20 ns.
- With optimised detector design and attached electronics it is possible to reach spatial resolutions in the order of $1 \mu\text{m}$ [7].

The properties and characteristics of silicon detectors are discussed in more detail in chapter 2.

1.3 Radiation Environment in the ATLAS Inner Detector

The ATLAS inner detector consists of approximately 64 m^2 of silicon strip detectors. The work contained in this thesis was carried out within the ATLAS **S**emi**C**onductor **T**racker (SCT) collaboration. In the following a description of the SCT design, with special focus on the strip detector part and the radiation levels expected is given. Detailed information on the silicon trackers of the other experiments at LHC can be found in [1, 4, 5].

A sketch of the inner detector is shown in figure 1.5. Silicon pixel detectors will cover the regions closest to the interaction region, followed by silicon strip detectors. In the outer parts of the inner detector the tracking information is provided by the **T**ransition **R**adiation **T**rackers (TRT). The silicon strip detectors will be arranged in 4 barrels and 18 end-cap wheels. The barrels will have a length of 1.4 m and will be placed at radii of 300, 373, 447 and 520 cm, respectively. The forward wheels will be placed between 0.8 and 2.8 m on either side of the centre of the detector. Both the barrel and the forward part will be built of a few thousand modules, each consisting of 4 detectors connected to frontend-electronics. A summary of the dimensions of the silicon strip part of the SCT is given in table 1.1.

Due to the high luminosities at the LHC the SCT will be exposed to very high hadron and gamma fluences. Monte Carlo simulations, such as FLUKA and DTUJET, have been used [8, 9] to determine the expected fluences. The radiation in the inner detector is due to several sources, dominated by particles coming directly from p - p collision. Further sources are

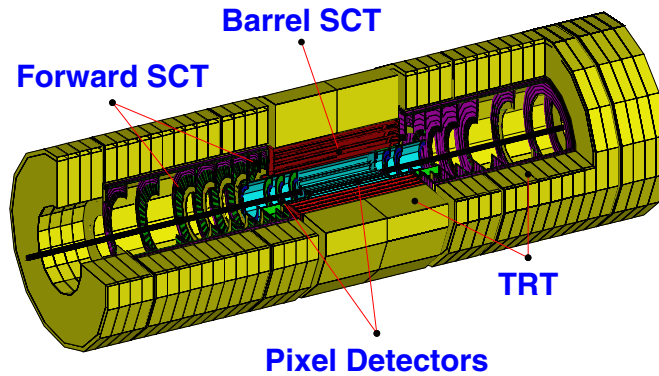


Figure 1.5: Sketch of the ATLAS inner detector.

local beam losses, beam-gas interactions and albedo neutrons from the calorimeters. The high radiation environment will cause damage in the silicon and activation of detector parts. The damage is mainly caused by high-energetic hadrons. Activation is due to spallation products from energetic hadrons and neutron capture.

The interaction of high-energetic hadrons in material can be classified in two groups: neutral particles and charged particles.

Neutral particles, e.g. neutrons, have two ways to interact in matter, either by absorption or by scattering. Absorption of neutrons by a nucleus results in an unstable compound nucleus in an excited state. Transition to the ground state can be carried out via several processes (emission of gammas, alphas, neutrons or protons). Neutron scattering occurs in two processes: inelastic and elastic scattering. In the inelastic process part or all of the kinetic energy of the neutron is used to excite the nucleus, which decays with emission of a gamma ray. In the case of elastic scattering the nucleus can be displaced from the lattice site. For silicon the neutron energy must be at least 110 eV, therefore thermal neutrons will not cause displacement damage [10].

	Barrel	Forward
Total Area (m ²)	34.4	26.7
Modules	2112	1976
Channels	3244032	3035136

Table 1.1: Overview of the dimensions of the silicon strip detector part of the SCT

Charged hadrons can interact with the electrons of a nucleus causing ionisation or excitation of the electrons. The energy-loss of charged hadrons due to ionisation is described by the Bethe-Bloch formula [11]. If the incident particle is scattered by the electric field of the nucleus and sufficient energy is transferred, then the nucleus can be displaced from its lattice site.

For electrons passing through matter with energies above a critical value ($E_c > 580 \text{ MeV}/Z$) radiative effects dominate the energy loss. The electron is accelerated or decelerated and a bremsstrahlung photon is emitted. Below E_c the ionisation, as for charged hadrons, is the major source for energy loss.

Photons interact with matter in three ways: the photoelectric effect, where the photon is completely absorbed and an electron emitted from the shell; Compton scattering, where only part of the photon energy is absorbed and an electron emitted; and finally pair-production, where a photon produces an electron-positron pair by interacting with the nucleus field. For photon energies below $\sim 0.06 \text{ MeV}$ the photoelectric process dominates, then the Compton effect takes over. At energies above $\sim 1 \text{ MeV}$ pair production is the dominating process.

A more detailed discussion of radiation damage mechanisms in silicon and the macroscopic effects of radiation is given in chapter 3. The consequence of radiation damage in the ATLAS silicon tracker is a decrease in performance which will limit the achievable physics results. Generally, high hadron fluences cause an increase in the leakage current and the full depletion voltage of the silicon detectors. The leakage current contributes to the parallel noise of the attached frontend electronics and does therefore limit e.g. the spatial resolution [6]. The full depletion voltage can increase beyond the stable operation point of the detector where current breakdown occurs. Additionally the high depletion voltage leads to higher power dissipation limited by the given range of the available power supplies and the cooling power provided.

Table 1.2 summarises the simulated fluences for the silicon strip detectors integrated over the 10 years of operation at z-values of 75 cm for the barrel and 83 cm for the forward part, which will be the most exposed parts as shown in simulations. Each forward disk is built of three concentric rings of modules, where module 1 corresponds to a module on the innermost ring.

	Total Hadron Fluence after 10 years [10^{14} 1MeV equivalent n/cm ²]
Barrel 1	1.40
Barrel 2	1.03
Barrel 3	0.85
Barrel 4	0.77
Forward Module 1	1.43
Forward Module 2	1.23
Forward Module 3	0.91

Table 1.2: Simulated fluences for the four barrels at $z=75\text{cm}$ and for the first forward disk at $z=83\text{cm}$ for the ATLAS SCT [8].

The simulations have shown that the main damage to silicon detectors will arise from charged hadrons and neutrons. At lower radii pions are of main concern, while at larger radii neutrons are dominating. As has been described above, hadrons can lose energy by ionisation or scattering, causing displacement. Ionisation damage will mostly occur in the silicon dioxide, while displacement of atoms causes bulk damage. According to [12] the damage constants are independent of the particle type and energy if normalised to the non-ionising energy loss. Therefore all data in table 1.2 are given in the equivalent fluence of 1 MeV neutrons [8].

Due to uncertainties in the simulations the fluences have an estimated error of $\pm 50\%$ [8]. Therefore the design values have been set to 1.5 times the maximum of the total hadron fluence. For the barrel detector the design value is 2.1×10^{14} 1 MeV n/cm² and for the forward detectors it is 2.15×10^{14} 1 MeV n/cm².

Generally the ATLAS silicon strip detectors will have to provide excellent performance in a harsh radiation environment ($\sim 2 \times 10^{14}$ 1 MeV n/cm²) over 10 years of LHC operation. A better understanding of the radiation mechanisms, the influences of external parameters, such as design, process, etc., and the time evolution of the characteristics of the damaged detectors will show where the limits in performance are. A series of irradiation tests were carried out to measure the damage expected after 10 years. Results of these studies are presented in this thesis. Additionally, results of a testbeam and source tests with fast readout electronics connected to irradiated and non-irradiated ATLAS prototype detectors are presented.

Chapter 2

Silicon Strip Detectors

Contents

2.1	Current Voltage Characteristics	12
2.2	Capacitance Voltage Characteristics	15
2.3	Silicon Strip Detectors	17
2.3.1	Process and Layout of Silicon Strip Detectors . . .	17
	Coupling of Strips	18
	Biasing Schemes	19
	Guard Rings	20
	Strip Resistance	23
	Interstrip Capacitance	23
2.4	Setup for Static Measurements	23
2.4.1	Leakage Current Measurements	24
2.4.2	Capacitance Measurements	25

Standard silicon strip detectors are based on the junction formed by highly p-doped (p^+) silicon with a lightly doped n-bulk. In principle a silicon strip detector is formed by subdividing the p^+ layer of a diode into parallel strips. The basic properties of doped silicon and a description of the p-n junction and its functionality is given in appendix A. In the following the current-voltage (I-V) and the capacitance-voltage (C-V) characteristics of reverse biased p^+ -n junctions are discussed and examples are presented. I-V and C-V measurements are standard tools to characterise the static properties of silicon strip detectors. I-V measurements provide information on the quality of the diode, such as the amount of leakage current, the stability and breakdown characteristics. From C-V measurements one can obtain the full depletion voltage which defines the operating conditions in terms of voltage. C-V measurements are also used to determine the capacitance in

between strips. The interstrip capacitance dominates the load capacitance of a strip as seen from an amplifier. Leakage Current and total capacitance finally limit the noise performance and so ultimately the survival and required spatial resolution of the detector. The production and layout of silicon strip detectors are discussed with special emphasis on guard rings. They are essential for high voltage operation after radiation induced damage. Finally, a short description of the setup used to carry out the static measurements is given.

2.1 Current Voltage Characteristics

In an ideal partially depleted p-n junction without external bias a drift current flows in the electric field of the depletion region and a diffusion current due to a concentration gradient in the undepleted region. For a junction in thermal equilibrium these currents cancel each other out and the total current is zero. Applying a voltage to the pn-junction disturbs the balance between diffusion and drift current of electrons and holes. If the junction is forward biased the potential across the junction is decreased and thus the drift current in the electric field is reduced. More electrons and holes diffuse into the p and the n-part of the junction, respectively. In the case of a reverse biased junction the potential is increased and the diffusion current is reduced [13].

In an ideal junction no net current is created in the depletion region. All the currents are originating from the neutral regions. A further assumption is that the depletion region ends abruptly. In the forward direction the current increases strongly at a constant rate for biases above $V=3kT/q$. In the reverse direction the current saturates at a value I_S and remains constant with increasing voltage.

Figure 2.1 shows the leakage current measured on a p^+ -n diode in forward and reverse direction. Note the different axes for the currents in forward and reverse direction. The leakage current in the reverse direction is only a few tens of pico-amperes for this diode while in forward direction the current increases to $200 \mu A$ at $-0.5 V$. The measured diode I-V characteristic reflects qualitatively the same behaviour as an ideal junction.

The diode measured is based on a junction of a thin layer of highly doped p-type silicon on n-bulk silicon. In order to have a complete circuit, electrodes have to be fitted onto the two sides of the junction. In general an ohmic contact cannot be formed by depositing metal onto the lightly doped semiconductor bulk material because this contact results in the creation of a rectifying junction with a depletion zone extending into the semiconductor. To prevent this formation a highly doped silicon layer has to be placed between the metal contact and the lightly doped bulk. According to equa-

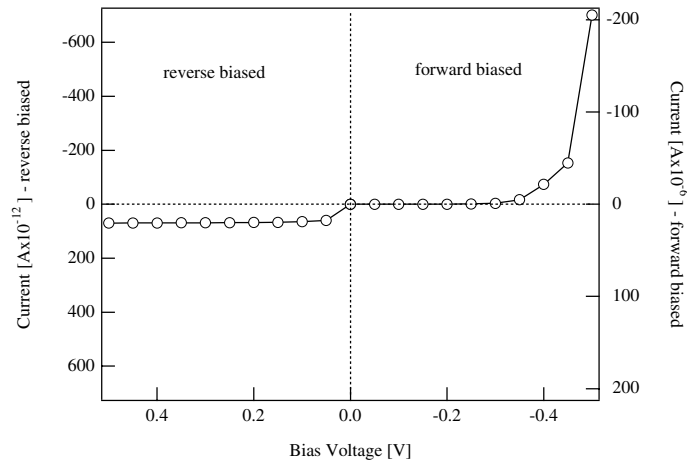


Figure 2.1: Leakage current measured in forward and reverse direction on a p^+ - n diode. Note that the current in reverse direction is displayed on the left axis while the current in forward direction is displayed on the right axis.

tions A.12 and A.13 the depletion depth is then practically zero [14]. A thin layer of highly doped n-type (n^+) silicon is implanted before an electrode is deposited on the n-side of the junction. Aluminium contacts can then be fitted to the junction as displayed in figure 2.2.

The ideal diode does not take into account the generation and recombination of carriers in the depleted zone of the junction. The dominant process for generation-recombination is the electron and hole emission into conduction and valence band, respectively, through generation-recombination centres. These centres are located in the forbidden band gap caused by defects in the lattice or impurities. The capture processes are negligible for a reverse biased junction as their rate depends on the carrier concentration

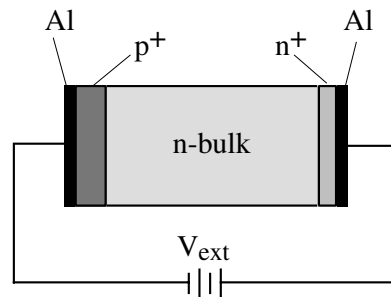


Figure 2.2: Schematic of a p^+ - n junction with electrodes fitted to the junction sides.

which is very small in the depleted layer. The generation of free carriers is therefore dominating. Only those generation centres which have electron energy levels close to the centre of the band gap contribute significantly to the generation current [13]. The generation rate can be derived from the Shockley-Read-Hall theory. The generation current I_{gen} is then

$$I_{gen} = \frac{qn_i W}{\tau_g} \quad (2.1)$$

where τ_g is the generation lifetime, q is the electron charge and W is the depletion width. I_{gen} is implicitly temperature dependent via the intrinsic carrier concentration n_i . Using equation A.4 the current increases by a factor of two every 8.6 K with a bandgap energy of 1.12 eV. The temperature dependency of the generation current can be described using equation A.4.

$$I_{gen} \propto \exp(-E_g/2kT) \quad (2.2)$$

From equation 2.1 I_{gen} is directly proportional to the depletion width W , which increases with the square root of the externally applied voltage (see appendix A). Thus the generation current increases with applied bias voltage and remains constant when the detector is fully depleted.

For a reverse biased p⁺-n junction the total current can be approximated by the sum of the diffusion current in the neutral regions and the generation current in the depletion region. At temperatures below 175 °C the generation current dominates and thus the current increases with the square-root of the applied bias. It is therefore possible to estimate the full depletion voltage from simple I-V measurements. A more accurate determination can be derived from capacitance-voltage measurements described in the following section.

If sufficient high voltage is applied onto the reverse biased junction, the junction will break down and conduct a very large current. The breakdown is another deviation from the ideal junction behaviour. Breakdown can occur either as *Zener breakdown* (or tunneling effect) or *avalanche breakdown*.

Tunneling occurs at very high fields, about 10⁶V/cm and higher. A valence electron can make a transition from the valence band to the conduction band by tunneling through the barrier. Even though its energy might not be high enough to overcome the barrier there is a finite probability that tunneling occurs. To reach sufficiently high fields for Zener breakdown very high doping concentrations, both in the p and the n-region, are required (>5×10¹⁷cm⁻³). In general the doping concentrations used in the bulk material of silicon detectors are not high enough to allow Zener breakdown [13].

In avalanche breakdown the carriers gain enough energy from the electric field to produce new electron-hole pairs by ionisation. The newly created electrons and holes now gain energy from the field and create further

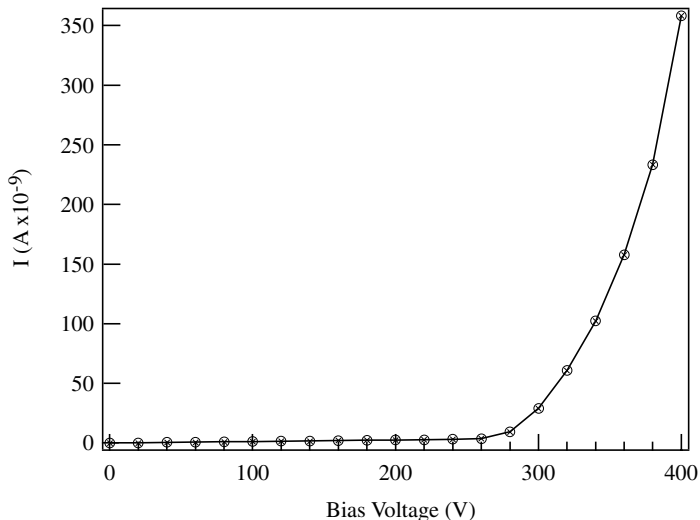


Figure 2.3: Leakage current of a p⁺-n diode indicating soft breakdown at higher voltages.

charge pairs which continue this process. The breakdown voltage is primarily controlled by the doping of the lightly doped bulk region. In practice the junctions can be manufactured so that the breakdown only occurs at voltages higher than the operation voltage by reducing high field regions. Figure 2.3 shows the reverse leakage current measured for the same diode as in figure 2.2 to higher bias voltages. Breakdown is indicated around 280V. Sharp implant edges are regions with high electric fields and thus a source for avalanche breakdown. Therefore in the design of a detector sharp edges are avoided to allow stable current conditions at high voltages.

A further deviation from the ideal junction current are *surface currents*. Surface currents can be due to surface contamination, high interface charge densities or the depletion region extending too close to the physical edge. These currents can be limited in the fabrication process, by careful handling and by placing guard rings, which are diodes surrounding the detector diode (see also section 2.3.1). However, it is very difficult to quantify surface currents and to predict as they depend on the production process and hence are manufacturer dependent.

2.2 Capacitance Voltage Characteristics

The depletion layer between the two sides of a p-n junction depends on a voltage dependent charge [13]. The depletion capacitance can therefore be defined as $C_j = dQ/dV$. If the voltage applied to the junction is changed by

an amount of dV the charge increment dQ appears on either side of the junction as a result to the wider depletion width W [15]. This causes an increase in the electric field by an amount of $dE=dQ/\epsilon_S$. The depletion capacitance C_j for a junction cross-section A is given as

$$C_j = \frac{\epsilon_S A}{W}. \quad (2.3)$$

where ϵ_S is the permittivity of silicon. This corresponds exactly to the capacitance of a parallel plate capacitor with spacing W . Equation 2.3 assumes that only the increment of the space charge in the depletion layer contributes to the capacitance, which is a good approximation for a reverse biased junction.

For silicon strip detectors the geometrical capacitance of a parallel plate capacitor with the same thickness and electrode sizes as the silicon detector sets a lower limit to the capacitance of the device. Additional effects, such as surface charge layers can lead to a somehow higher body capacitance [16]. However, the expected capacitance for a parallel plate capacitor of the dimensions given by the silicon detector is an excellent approximation and estimation of the expected capacitance.

For a reverse biased p^+ - n junction W can be substituted using equation A.14.

$$C_j = A \sqrt{\frac{\epsilon_S q N_D}{2(V_{ext} - V_{bi})}} \quad (2.4)$$

V_{ext} is the externally applied bias and V_{bi} is the so called built-in voltage, see also appendix A. From equation 2.4 one can derive the impurity concentration N_D by plotting $1/C^2$ versus $(V_{ext}-V_{bi})$. The slope gives the impurity concentration. In the case of a p^+ - n junction $N_D \sim N_{eff}$, where N_{eff} is the effective doping concentration N_D-N_A .

The capacitance decreases with increasing bias voltage until W is equal to the full width of the junction. If the junction is fully depleted the capacitance remains constant. The voltage at which the capacitance becomes constant defines the full depletion voltage V_{fd} . Graphically, V_{fd} can be defined by plotting $1/C^2$ versus V_{ext} and fitting a line to the region of decreasing capacitance and a line to the region of constant capacitance. V_{fd} is then defined by the intersection of the lines.

Figure 2.4 shows the capacitance of a silicon diode measured as a function of voltage.

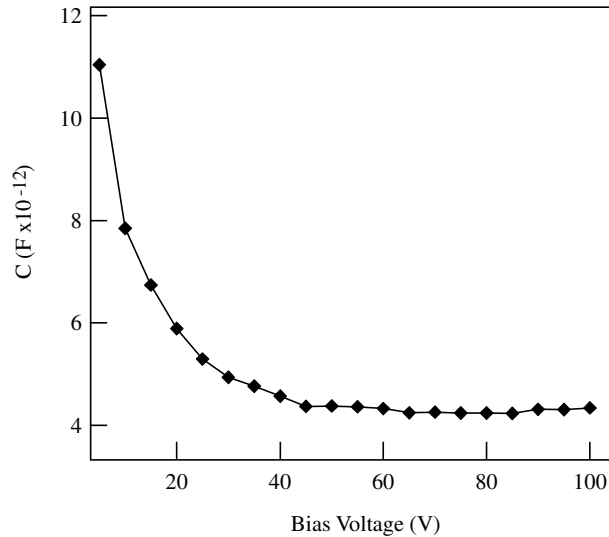


Figure 2.4: Measured capacitance of a p^+ -n diode as a function of voltage.

2.3 Silicon Strip Detectors

The p-n junction represents the basic element of a silicon detector which may be implemented in various geometries. Diodes, which are basically p-n junctions, are the simplest form, but during the last decade a lot of work has been invested to develop more complicated structures, such as silicon strip detectors or pad detectors. In figure 1.4 one corner of a silicon strip detector developed for ATLAS is shown. In the following section the layout and production of silicon strip detectors are discussed.

2.3.1 Process and Layout of Silicon Strip Detectors

The most common form of a silicon strip detector is a p^+ -n junction where the p^+ side has been divided into many small parallel strips. The individual strips act as many thin diodes and allow very good spatial resolution of passing tracks. The use of planar technology enables the precise construction of these diodes, with widths in the order of $10 \mu\text{m}$ to a few millimetres [15, 17].

The production of a p^+ -n silicon strip detector starts with a high purity, lightly n-doped wafer. The standard thickness of such wafers is $300 \mu\text{m}$. Going to thinner wafers decreases the production yield as more wafers are damaged during handling. The standard resistivity of these wafers is 4-6 $\text{k}\Omega\text{cm}$. The crystal orientation is mostly $\langle 111 \rangle$ or $\langle 100 \rangle$.

By placing the wafer in a furnace in an oxygen atmosphere a silicon dioxide layer is grown on the crystal surface. The wafer is now fully pas-

sivated and protected against impurities, moisture and mechanical damage. To grow thick layers of oxide water vapour is added to the atmosphere. This oxide is then referred to as wet oxide contrary to dry oxide which is grown in a water free atmosphere. The advantages of wet oxide is the faster growing rate, but on the other hand it tends to contain more imperfections than dry oxide.

Selected areas of the oxide are then removed by using photolithographic and etching techniques. By ion implantation or diffusion doping atoms are placed in the bulk material. Accuracies to $1\ \mu\text{m}$ can be reached by using appropriate masks. Each mask contains the pattern for one layer of the device. Using ion implantation, ions selected by a mass spectrometer are accelerated and fired at the wafer. The advantage of ion implantation is the high doping uniformity and the good control of the process. On the other hand the bombardment causes severe damage to the silicon crystal and heating is needed to anneal these defects. The diffusion process is less time consuming and does not result in lattice damage, but the doping distribution is not so well defined.

In order to have an electrical contact to the silicon metal is deposited onto the wafer. Desired patterns are generated by wet or plasma etching using appropriate masks. The pattern visible in picture 1.4 is the Aluminium pattern on the p^+ -side of the detector. Finally the detector can be passivated with a silicon dioxide or a polyimide layer to protect it against humidity and mechanical damage.

This sequence of oxidation, opening of windows, implantation, metalisation and passivation is a simplified description of the process needed to produce a silicon strip detector and only lists the main steps.

Coupling of Strips

Figure 2.5 shows the schematic cross-section of a p^+ -n silicon strip detector. There are two ways to couple a strip to the channel of the readout electronics. If the aluminium is placed directly on top of the implant, this is referred to as a *dc coupled* strip. The disadvantage of this technique is that the leakage current can flow directly into the amplifier. As the dark current can vary from strip to strip and as a function of time, large pedestal variations have to be expected. If the current is sufficiently high it can drive the electronics into saturation. One possible solution is the design of a current sink in the amplifier. The second possibility is to place a dielectric layer between the aluminium and the implant, which is referred to as an *ac coupled* strip. This can be compared to introducing a capacitor between the strip and the readout electronics, preventing the current flowing into the amplifier. The insulating layer can be dry silicon dioxide or silicon nitride or a combination of both. Usually the coupling oxide has a thickness of 200-300 nm [6].

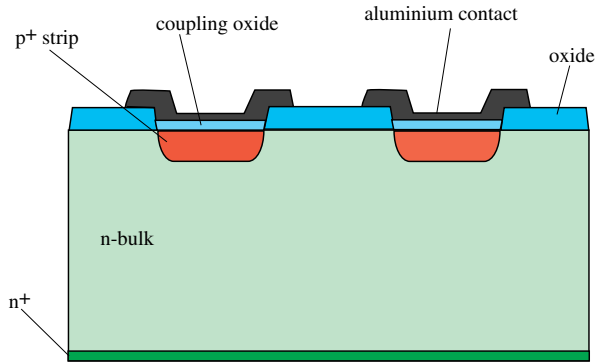


Figure 2.5: Schematic cross-section of an ac coupled p^+ -n detector.

Biasing Schemes

To ensure that all strips of a detector are at the same potential they have to be connected to a common line. This line is a p^+ implant running across all strips on one side of the detector and is referred to as the biasline. A bias resistor connecting the strip implant to the biasline has to be sufficiently high to insulate the strips from each other and not to be a significant source of electronic noise as will be discussed in chapter 4. Polysilicon deposited in the small gap between the strip and the biasline can provide bias resistors of up to about $50\text{ M}\Omega$. *Polysilicon resistors* are often shaped in a meander pattern to optimise the space available. The production of polysilicon resistors necessitates several additional photolithographic steps to pattern the resistor and to provide contacts. This adds to the production costs of a silicon strip detector which are approximately proportional to the number of masks.

Another technique is the *reach through biasing* of the strip. The p^+ -biasline, the n-bulk material and the p^+ -strip represent a p-n-p field effect transistor. If a negative voltage is applied to the biasline one of the two p^+ -n junctions becomes forward biased and the other reverse biased. With increasing voltage a depletion region grows around the backward biased junction, represented by the biasline and the n-bulk. At the so called punch-through voltage the depletion region will reach the strip. The punch-through voltage depends on the bulk doping concentration, the gap between biasline and strip and the oxide charge present. Another variation of the punch through biasing is the **Field OXide Field Effect Transistor** biasing (FOX-FET) [18]. A metal line is placed on top of the oxide in the gap between the biasline and the strip. Applying a voltage to this metal line, the gate, allows control of the voltage drop between biasline and strip. The resistance between the strip and the biasline depends on the I-V characteristic of the biasing structure. The so called dynamic resistance is defined as $R = \delta V_{strip} / \delta I$, where I is the current flowing from the strip to the biasline.

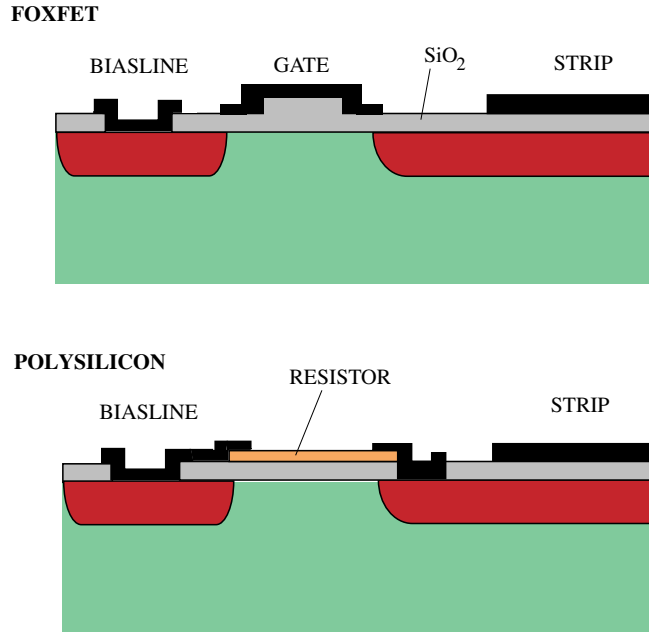


Figure 2.6: Schematic view of a FOXFET structure and a polysilicon bias structure.

Very high resistances of up to $G\Omega$ can be reached with this technique [19]. When irradiated the dynamic resistance and the punch-through voltage decrease due to Si-SiO₂ interface traps [20]. A further complication is that after irradiation additional noise from the FOXFET structure has been observed, leading to degradation of the detector performance [21].

In figure 2.6 a schematic view of a FOXFET structure and a polysilicon bias structure is shown.

Guard Rings

As discussed in section 2.1 breakdown currents limit the operation voltage of a silicon detector. The permanent oxide charges and the related electron accumulation layer restrict the growth of the depletion layer along the surface, resulting in increased fields around the implant edges. Another source for high currents is the depletion region extending to the cutting edge of the detector, which is a high generation-recombination region due to lattice damage. Depletion to the edge is enhanced if negative charges are present on the oxide surface, e.g. due to moisture. Figure 2.7 shows the depletion region around a p⁺-implant with positive charges in the oxide. Note the increased density of equipotential lines close to the implant edge.

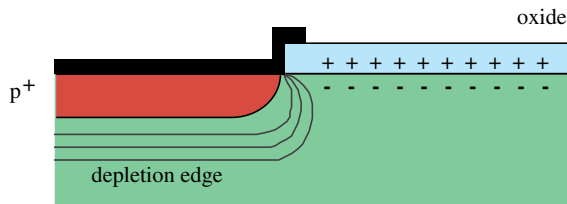


Figure 2.7: Influence of the oxide charge on the depletion width along the surface.

Guard rings on an p^+ -n strip detector are p^+ -rings surrounding the strip region. In figure 1.4 a multiple guard ring structure is visible surrounding the strips. As the bias voltage on the detector is increased the depletion region surrounding the active area meets the first guard ring by a punch-through mechanism. Thus the high fields close to the surface are considerably reduced. As the bias is further increased the depletion region punches through to the next guard ring. In this way a degraded potential is created. By contacting the innermost guard ring the current arising from the edge regions can be separated from the active area providing a better noise level for the readout strips. Guard rings therefore reduce high field regions, degrade the potential so that the outermost guard ring is ideally at the backplane potential and decouple current from the edge regions [22, 23].

When designing a guard ring structure several parameters have to be taken into consideration: the distance between the guard rings, the oxide charge, the bulk doping concentration and the width of the guard rings. A further important parameter is the passivation of the detector.

Recently the development of multi-guard structures up to about 20 guard rings has been realised to allow high voltage operation even after irradiation. The detector displayed in figure 1.4 was designed by SINTEF as an ATLAS prototype p^+ -n detector and has an optimised guard ring design to allow operation after irradiation. The leakage current measurement displayed in figure 2.3 was carried out on a diode with a multi guard structure produced at SINTEF. Due to the multi guard structure breakdown does not occur until about 280V.

Another example shows that the guard ring characteristic can be improved by passivating the detector. Figure 2.8 and figure 2.9 show the guard ring leakage currents of ATLAS prototype p-in-n detectors. All detectors were produced in the same batch and under the same conditions. Figure 2.8 displays the guard ring currents of non-passivated detectors, while figure 2.9 shows the the guard ring currents of detectors which have been passivated with polyimide. Note that on some detectors from the non-passivated set the guard ring starts to break down at around 300 V, while on the passivated detectors a much more uniform behaviour is shown. On the passivated

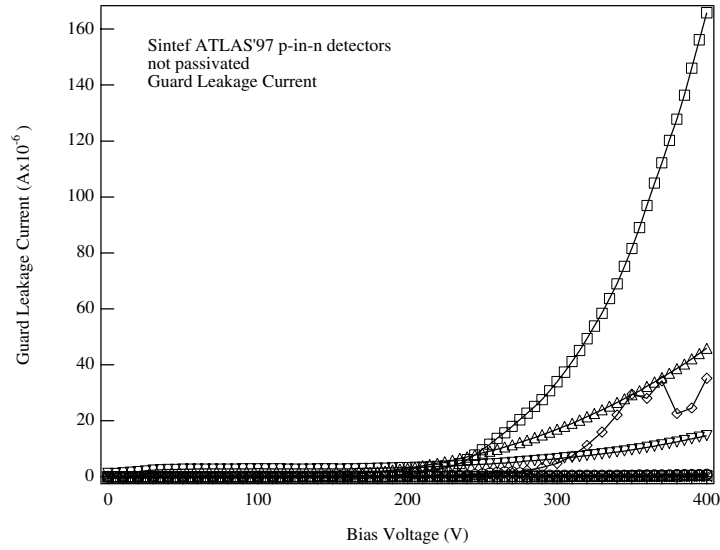


Figure 2.8: Guard ring leakage currents of non-passivated ATLAS prototype detectors.

detectors all detectors show stable currents up to 450-500 V and the measurement could be carried out up to 600 V.

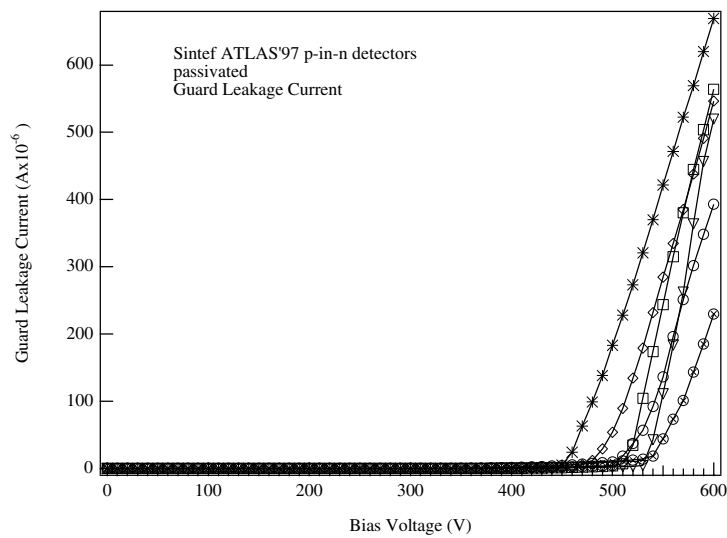


Figure 2.9: Guard ring leakage currents of ATLAS prototype detectors passivated with polyimide.

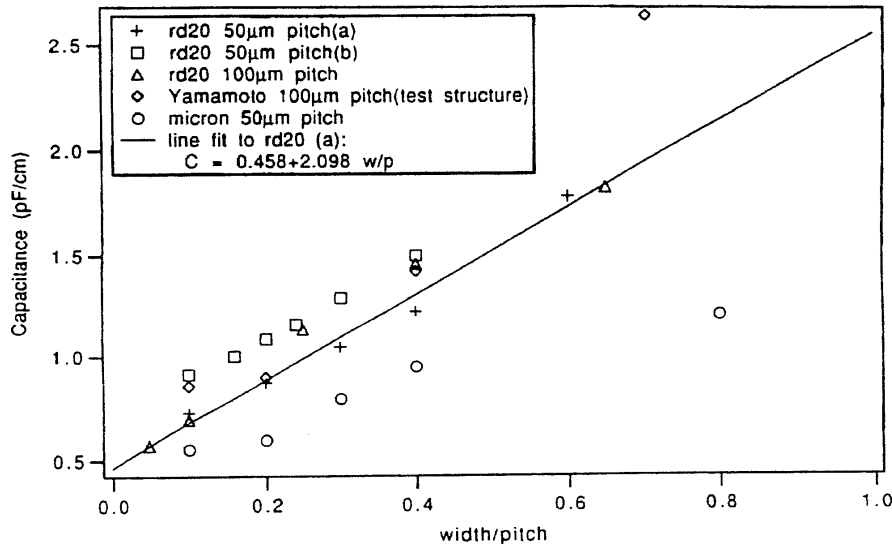


Figure 2.10: Correlation between interstrip capacitance and the ratio of strip width to strip pitch from measurements on different structures [24].

Strip Resistance

Due to the process positive charges are located in the oxide and the oxide-silicon interface. This leads to an electron accumulation layer just beneath the oxide. The strips are ohmically separated by this electron layer with interstrip resistances in the order of several hundred $M\Omega$ [6].

Interstrip Capacitance

The interstrip capacitance is a very important parameter as it dominates the single strip capacitance seen by the amplifier, and thus has the most important effect on the noise performance of the system. The interstrip capacitance depends roughly linearly on the ratio of strip width to strip pitch, as can be seen in figure 2.10. Deviations from the fit can be put down to different process conditions. The interstrip capacitance depends also on the number of intermediate strips and generally increases if more intermediate strips are present.

2.4 Setup for Static Measurements

Static measurements on silicon strip detectors characterise their quality and give information on process parameters. The two most basic static meas-

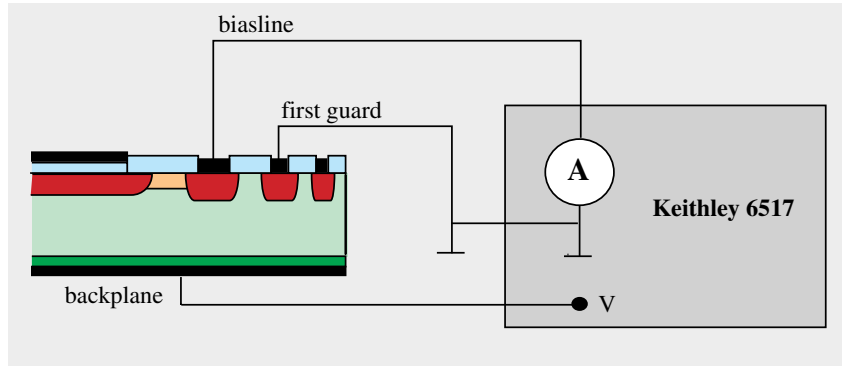


Figure 2.11: Setup to measure the leakage current from the active volume.

Measurements are the measurement of the total leakage current and the body capacitance. Further measurement parameters can be the measurement of the interstrip capacitance, the interstrip resistance, the coupling capacitance or the aluminium resistance.

The measurements are carried out on a probe-station with manipulators. These manipulators are equipped with thin needles with peak radii in the order of $2\ \mu\text{m}$ to contact single strips or pads on the detector. The backside of the detector is placed on a metallic chuck, usually aluminium, coated with conductive elastomer. A vacuum pump pulls the detector to the chuck thus forming good electrical contact to the backside. Generally the probe station is housed in a light tight box.

2.4.1 Leakage Current Measurements

The leakage current can be measured by introducing an ammeter into the bias path of the detector. Shown in figure 2.11 is a schematic setup to measure the leakage current from the active volume. The ammeter is connected to the biasline. The contact to the innermost guard ring is grounded and thereby allows separation of the current arising from the active volume and from the edge region. In the same way the current from the edge region can be measured by exchanging the contacts to the ammeter.

The bias voltage is supplied via a high voltage source from Keithley which includes an ammeter. The accuracy depends on the measurement range. It is in the order of 1% for low currents (up to 2 nA), and for currents up to 2mA in the order of 0.1%. To automatise the measurements the Keithley instrument is connected to a Macintosh computer via a GPIB bus. A LabView program carries out the measurements and acquires the data. The current is strongly temperature dependent, as can be seen in equation 2.2, and thus a constant temperature has to be maintained throughout the measurements. In addition a pt100 sensor placed near the chuck monitors the temperature.

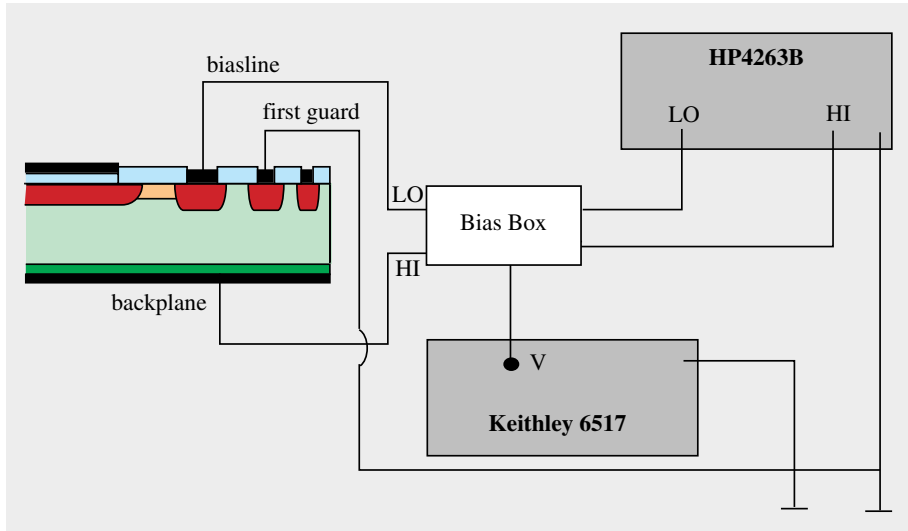


Figure 2.12: Setup to measure the body capacitance of the active volume.

To carry out stability measurements of the current another LabView program was developed which ramps the voltage up to a given value and takes measurements at this voltage every few seconds. Thus the time evolution of current can be monitored.

2.4.2 Capacitance Measurements

A C-V analyser or LCR-Meter is used to measure the body capacitance of a detector. A small AC signal is applied on top of the bias voltage to measure the complex impedance represented by the detector. Assuming one of two different models for the device under test, either a parallel model with a capacitor and a resistor in parallel, or a series model with capacitor and resistor in series, the LCR-meter calculates internally the capacitance of the detector. An LCR-meter from Hewlett-Packard (HP4263B) is used to carry out the measurements presented here. The AC signal amplitude can be varied between 50 mV and 1 V in steps of 50 mV. The frequency of the applied signal can be set to 100 Hz, 120 Hz, 1 kHz, 10 kHz or 100 kHz. For non-irradiated detectors the C-V measurement is not sensible to the measurement frequency, but the frequency is an important parameter for irradiated detectors.

The stray capacitance introduced by the setup can be compensated for by the instrument, thus providing a very high level of precision. After correction the instruments accuracy is in the order of 0.5 pF at 100 Hz measurement frequency. In figure 2.12 the schematic setup to measure the body capacitance of a strip detector is displayed. As the HP4263B does not provide

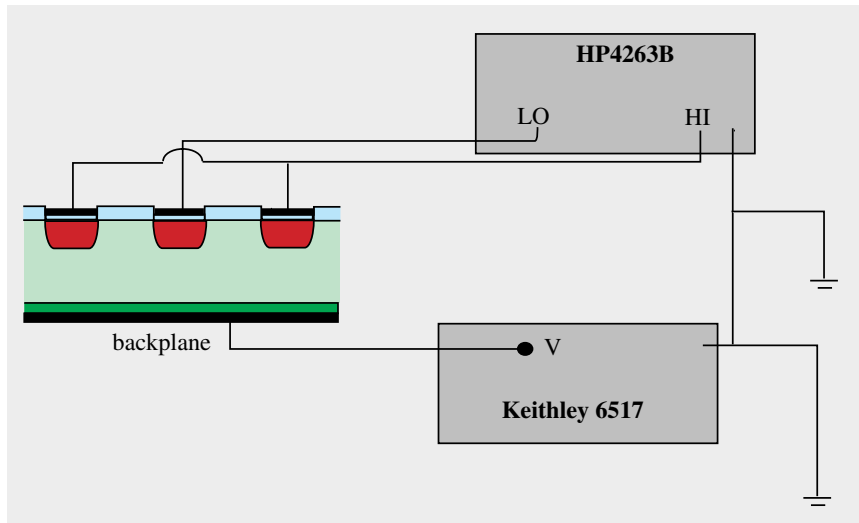


Figure 2.13: Setup to measure the interstrip capacitance to the next neighbours.

a high voltage bias source, the voltage source of the Keithley 6517 is used. To couple the voltage into the HI-path and also to protect the input of the LCR-meter from high voltage a bias box is used. It consists mainly of protection diodes and decoupling capacitors. Attention has to be paid to a $100.9 \text{ k}\Omega$ resistor in series with the supplied voltage. For high leakage currents the applied voltage has to be corrected for the voltage drop across this resistor. During the measurement of the body capacitance the guard ring is grounded in order to have a well defined volume.

The schematic setup to measure the interstrip capacitance to the nearest neighbours is displayed in figure 2.13. During the measurement the guard ring and the biasline is connected to ground. In the ideal case all other strips are connected to ground. However this is in most cases not possible, e.g. with many readout strips on a detector.

Chapter 3

Radiation Damage in Silicon

Contents

3.1	The NIEL Hypothesis	28
3.2	Surface Damage	30
3.3	Changes in Detector Properties	31
3.3.1	Leakage Current	32
3.3.2	Effective Doping and Full Depletion Voltage	34
3.3.3	Interstrip Resistance	38
3.3.4	Interstrip Capacitance	38
3.3.5	Bias Resistors	39
3.4	Radiation Damage Models	39
3.4.1	The Hamburg Model	39
3.4.2	The Ziock-Parameterisation	41
3.5	Results from ATLAS Prototype Detectors	44
3.5.1	Detector Baseline	44
3.5.2	Pre-Irradiation Results and Detector Irradiation	46
	SINTEF Detectors	46
	Detector Irradiation	49
3.5.3	Annealing Study of Irradiated Prototype Detectors	50
	C-V Measurements	54
	Leakage Current Measurements	59
	Annealing of the Full Depletion Voltage	65
3.5.4	Conclusions	69

Radiation damage in silicon can be divided into two effects: **surface damage** and **bulk damage**. In both cases ionisation and dislocation of atoms takes place. While ionisation in the bulk is not damaging, it creates

fixed positive charges in the SiO_2 and the SiO_2 -Si interface. On the other hand displacement damage is the reason for permanent bulk damage while displacement in the surface can be neglected.

A short overview of the surface damage is given in section 3.2. Changes in the interstrip resistance, the interstrip capacitance and the polysilicon bias resistors can be related to surface damage.

Bulk damage plays the major role in radiation damage as it causes changes in basic detector properties such as the leakage current and the effective doping concentration. These changes are the main limiting factors for operation at high fluences. The bulk damage is believed to scale with the **Non Ionising Energy Loss** (NIEL) in silicon. An introduction to this hypothesis is given in the following section. The effect of radiation on the leakage current and the effective doping concentration is discussed and experimental results are presented. Furthermore, the model developed by the Hamburg group [25, 26] and the parameterisation by Ziock [27] are presented shortly in section 3.4.

Finally, results from ATLAS prototype detectors before and after irradiation are presented and discussed.

3.1 The NIEL Hypothesis

The interaction of radiation with the silicon lattice depends not only on the particle type but also on the energy of the particles. Generally, charged particles lose a significant part of their energy by ionisation. The energy loss which is not due to ionisation (NIEL) occurs for high-energetic charged particles mainly by Rutherford-scattering and for neutrons mainly by elastic scattering with the silicon nucleus [28] and is the reason for permanent bulk damage.

As introduced in section 1.3 the NIEL can cause displacement damage in a silicon crystal. If sufficient energy is transferred a silicon atom is displaced from its lattice site and a so called **Primary Knock-on Atom** (PKA) is produced. The PKA can have enough energy to start moving through the lattice. It will lose energy by ionisation and by collisions with other atoms displacing them and producing vacancy-interstitial pairs (V-I pairs). Some of these V-I pairs will recombine immediately after their production. Mueller, Wilsey and Rosen [29] have carried out Monte Carlo studies to investigate the structure of damage cascades in silicon. Figure 3.1 shows the damage cascade caused by a 50 keV PKA in silicon from [29].

Their result reflects only the primary damage, not taking into account annealing effects due to recombination and diffusion. The simulated damage cascades reach lengths of a few hundred nanometers. The initial portion of the track is less damaged than the final one which ends in a so called terminal cluster where a silicon atom loses its last 5-10 keV. In the initial

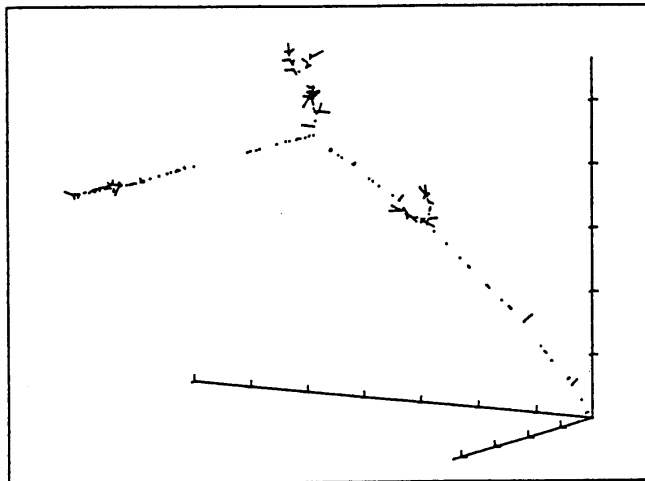


Figure 3.1: Simulated damage cascade of a 50 keV PKA from [29]. The cascade starts at the origin in an arbitrary direction. The axes are the spatial co-ordinates.

portion mainly point-like defects are produced. Cluster sizes as predicted by [29] are in the range of ≈ 5 nm with big portions of the cluster not being directly damaged. High energetic PKAs can end in more than one terminal cluster, most likely 2-3 clusters as shown in the simulations.

The basic assumption of the NIEL hypothesis is that the displacement damage scales with the amount of energy imparted in displacing collisions. The kinetic energy E_R of a PKA transferred during the collisions depends on the energy and mass of the incident particle and the silicon atom mass. The amount of transferred energy is described by the Lindhard partition function $P(E_R)$ and takes into account the charge of the lattice atom. In this way it is possible to define the displacement damage cross section $D(E)$, in units of [MeV·mb], for each particle type with an energy E .

The NIEL for a material with atomic mass A is directly proportional to $D(E)$ [28].

$$\text{NIEL} = \frac{dE}{dx}(E) |_{n.i.} = \frac{N_A}{A} D(E) \quad (3.1)$$

By defining a hardness factor κ which accounts for the particle energy and type it is possible to express an equivalent fluence ϕ_{eq} . Due to historical reasons Φ_{eq} is usually expressed for 1 MeV neutrons.

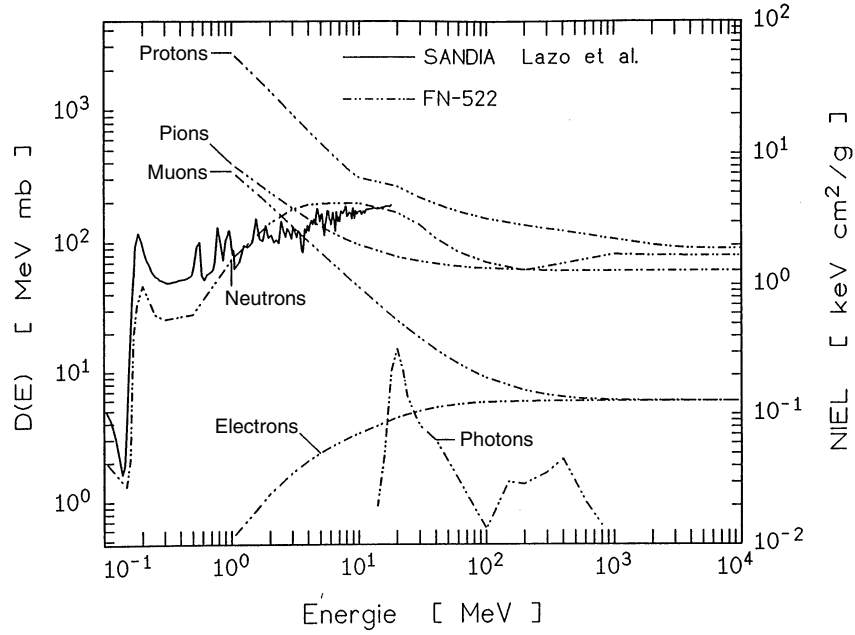


Figure 3.2: NIEL in silicon as a function of particle energy (broken lines), and displacement damage cross section for neutrons (full line) from [28].

$$\kappa = \frac{\int_E \Phi(E)D(E)dE}{D_n(1\text{MeV}) \int_E \Phi(E)dE} \quad (3.2)$$

$$\Phi_{eq} = \kappa\phi \quad (3.3)$$

Figure 3.2 shows the non ionising energy loss in silicon as a function of energy of the incident particle. Additionally, the displacement damage cross section for neutrons is given.

3.2 Surface Damage

As mentioned in the introduction to this chapter the ionisation in the silicon dioxide (SiO_2) and the interface to the bulk may lead to permanent damage.

Figure 3.3 shows schematically the process that leads to permanent damage in the oxide. Electron-hole pairs are created by an ionising particle

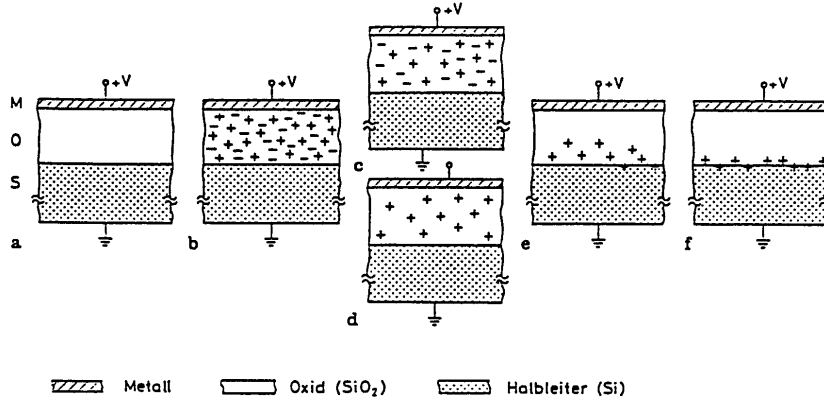


Figure 3.3: Schematic illustration of the introduction of fixed positive oxide charges in SiO_2 by ionisation from [28].

(b). Many of these pairs recombine immediately (c). Due to their high mobility in SiO_2 the electrons are soon collected at the positive electrode ($\mu_e \approx 20 \text{ cm}^2/\text{Vs}$). The holes which have a much smaller mobility in SiO_2 ($\mu_h \approx 2 \times 10^{-5} \text{ cm}^2/\text{Vs}$) are left behind and start moving slowly to the SiO_2 -Si interface (d) and (e). Finally the wholes are trapped at the interface in deep traps (f). Permanent positive oxide charges are now present at the interface and will lead to the creation of an electron accumulation layer in the bulk directly underneath the oxide. Positive oxide charges are normally already present in non-irradiated detectors due to the fabrication process. By irradiation more and more positive charges in the oxide are induced which leads to changes in some detector parameters such as interstrip resistance or interstrip capacitance.

In conjunction with the introduction of positive oxide charges, interface states are created at the SiO_2 -Si border. These states are additional energy levels in the silicon close to the SiO_2 -Si interface and influence the generation current properties of the material.

3.3 Changes in Detector Properties

Many experimental results have illustrated that the static properties of silicon detectors change significantly with irradiation. Most importantly, the leakage current and the depletion voltage are affected. Other radiation influenced parameters are e.g. the interstrip capacitance and the appearance of pin-holes in the coupling dielectric layer of ac-coupled detectors.

3.3.1 Leakage Current

The leakage current is an important property of silicon detectors. If the leakage current per strip is too high the parallel electronic noise will increase significantly and thus decrease the performance, see also section 4.1.1. High currents can lead to thermal runaway and unstable operational conditions. The bulk leakage current in a detector originates from generation centres in the forbidden band gap as described in section 2.1. It is well established that radiation induces more defect centres in the forbidden band gap which can then act as additional defect centers [28]. The additional leakage current is mainly due to defect centres located close to the mid band gap. The bulk leakage current increases linearly with the fluence. A proportionality constant α has been defined to describe the increase of the volume leakage current as a function of fluence.

$$\Delta I_{vol} = \alpha \phi \quad (3.4)$$

ΔI_{vol} is defined as the change in volume leakage current due to irradiation. The damage constant α is strongly temperature dependent due to the temperature dependence of the leakage current. α reaches a stable value of 2.5×10^{17} A/cm at 20 °C after irradiation [30]. An important effect is the annealing of the leakage current. After irradiation the leakage current decreases as a function of time. Within the first two weeks at room temperature $\approx 50\%$ decreases have been reported. Thus α decreases with increasing time and tends to stabilise at longer times. The rate of the annealing is also temperature dependent, which has been shown experimentally. The annealing rate increases with temperature. The kinetics of this temperature dependence have so far not been studied in detail.

Shown in figure 3.4 and 3.5 are the bias leakage current and the guard leakage current of a diode before and after irradiation.

The diode is 360 μm thick and has an active area of $3 \times 3 \text{ mm}^2$. Two guard rings surround the active area of which the innermost one is contacted. The diode was irradiated with 24 GeV protons to a total fluence of 3×10^{14} p/cm². After irradiation the diode was stored for 3 months at -10 °C. The leakage current measurement after irradiation was carried out at -10 °C and scaled to 20 °C according to equation 2.2. The measurement before irradiation was carried out at 20 °C. Before irradiation the leakage current of biasline and guard behave very similarly and are in the order of a few nano-amperes. Breakdown occurs at around 200 V.

After irradiation the behaviour has changed dramatically. The current level has increased to approximately 60 μA . Neither current shows any sign of breakdown up to almost 400 V. The biasline leakage current increases up to approximately 250V and then remains constant. This indicates that current originating from the bulk is now dominating the biasline leakage current and

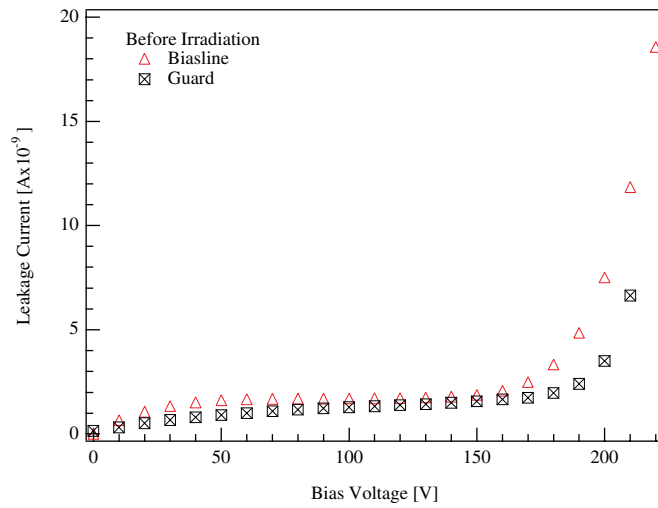


Figure 3.4: Diode leakage current before irradiation at 20 °C.

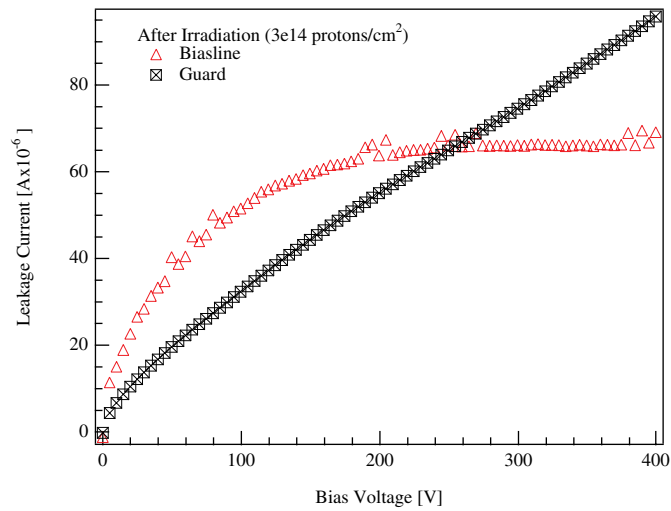


Figure 3.5: Diode leakage current after irradiation with 24 GeV protons to 3×10^{14} p/cm² scaled to 20 °C.

other contributions, such as surface currents play a less important role. From C-V measurements a full depletion voltage of 260 V at 100Hz measurement frequency was determined. This is in agreement with the full depletion voltage estimated from the I-V characteristic to be around 250 V. The guard ring leakage current has changed its behaviour completely and increases almost linearly with bias voltage.

Generally, after high radiation doses the surface effects in the leakage current of the active area are less important in comparison with bulk effects. The high leakage current in the active area after irradiation is due to additional radiation induced generation centres in the band gap. The behaviour of the guard ring current depends largely on the design and production.

Due to the strong temperature dependence of the leakage current, see 2.2, the significant increase in the current due to irradiation can be suppressed by operating the detector at lower temperatures. Accordingly the ATLAS silicon detectors are planned to be operated at -7 °C.

3.3.2 Effective Doping and Full Depletion Voltage

In a non-irradiated detector the effective doping concentration N_{eff} is determined by shallow dopants in the material (see also appendix A). In the case of n-type silicon this is usually provided by boron atoms. By radiation further energy levels are introduced in the forbidden band gap. Most of them are located close to the midband-gap and are referred to as deep levels. Experimentally it has been shown that these levels are mainly acceptor levels. Due to the deep level acceptors negative space charges accumulate in the depletion region and cause n-type silicon to become less n-type with increasing fluence. As a result N_{eff} decreases until the so called inversion fluence. At this point the negative space charge compensates the positive space charge of the donor impurities. With further increasing fluence the material behaves more and more p-type under bias. The inversion is not the physical removal of the donors in the n-silicon but an increase of acceptors. If a bias voltage is applied this change is reflected in the measured N_{eff} . Type inversion can thus only be observed if the sample is under bias. Figure 3.6 shows N_{eff} as a function of 1 MeV neutron fluence for two different detectors. The inversion was found to occur at around 2×10^{13} 1 MeV neutrons/cm² [30].

The effective doping concentration can be parameterised as shown in equation 3.5. The two terms represent the compensation of donors and the creation of acceptors due to radiation [31]:

$$N_{eff}(\phi) = N_{eff,0} \exp(-c\phi) - \beta\phi \quad (3.5)$$

ϕ is the fluence, $N_{eff,0}$ represents the initial doping concentration.

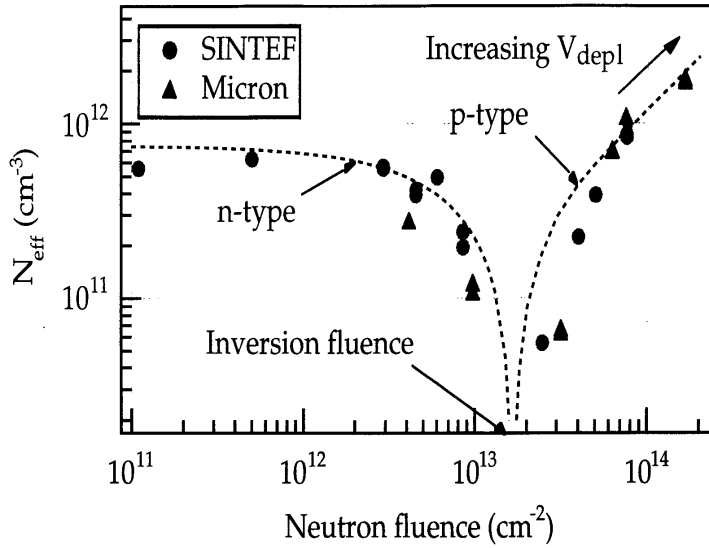


Figure 3.6: N_{eff} as a function of neutron fluence for two high resistive n-type diodes from [30].

As a result of the inversion the junction of a p^+n detector moves to the backside (n^+) from where the detector now starts to deplete. The detector remains fully functional even after inversion. An important consequence is that if the detector is underdepleted charges produced by a traversing particle will have to move through a layer of non depleted silicon before being collected at the strips. This will lead to a lower and broader registered signal. Principally p^+n detectors (also referred to as p -in- n detectors) should be operated fully depleted after inversion to be fully efficient.

To overcome this problem the production of n -in- n detector was proposed for the ATLAS inner detector. These detectors have n^+ -implanted strips on n -bulk material with a p^+ -implantation on the backside which forms the diode. After type inversion the n -bulk material will behave as p -type silicon. But as the strips are heavily n -implanted, the junction is now the strip side. In this way it is possible to operate the detector with reduced collected charge. Results on prototype n -in- n detectors for ATLAS are presented and discussed in section 3.5.

Attempts to understand the change of N_{eff} and the creation of deep level acceptors have been undertaken during the last years. **Depp Level Transient Spectroscopy (DLTS)** and **Thermally Stimulated Current (TSC)** measurements have given first informations on the defects present in irradiated material. The majority of the produced vacancy-interstitial pairs in the terminal cluster recombine immediately. Di-vacancies or multi-vacancy

complexes may also be created. Those vacancies and interstitials which escape the initial recombination can diffuse through the crystal and react with other defects or impurity atoms, such as oxygen or carbon. A primary list of possible reactions has been established by [32] and been further developed into a kinetics model which tries to describe the evolution of defects [33, 34]. The defect complex V_2O has been identified to be a candidate for a deep level acceptor state which may be responsible for the macroscopically observed changes.

After irradiation N_{eff} changes as a function of time. Two phases can be distinguished:

- Immediately after irradiation N_{eff} decreases with time until a minimum is reached. This is referred to as **beneficial annealing**. The decay of active radiation induced acceptor sites back into neutral sites is believed to be responsible for the decrease of N_{eff} .
- After N_{eff} has reached a minimum it starts to increase with time. This is thought to be related to the creation of deep acceptor levels by diffusion of defects and consequent reactions between defects. It is referred to as **reverse** or **anti-annealing**. Generally, the reverse annealing takes place much more slowly than the beneficial annealing. On the other hand the changes in N_{eff} are larger.

Displayed in figure 3.7 is the annealing of two diodes irradiated to two different fluences at room temperature. Clearly visible are the two phases of the annealing, the beneficial and the reverse annealing.

Both annealing phases have been shown to be extremely temperature dependent. Below 0 °C the process of reverse annealing is almost halted. At higher temperatures the process is accelerated which leads in the end to a very high full depletion voltage (V_{fd}) which is directly proportional to the effective doping concentration N_{eff} .

The slowing down of annealing at low temperatures is illustrated in figure 3.8.

The diode is a standard p^+ - n diode of 360 μm thickness. Two guard rings surround the active area of $3 \times 3 \text{ mm}^2$. The innermost guard ring is grounded during the measurements. The diode has been irradiated in a 24 GeV proton beam at CERN to a total fluence of $2 \times 10^{14} \text{ p/cm}^2$. The irradiation was carried out in two days during which the diode was not biased. Immediately after irradiation the depletion voltage was measured at room temperature in a probe station. After the measurement the diode was stored at -10 °C in a freezer. This procedure was repeated throughout a month and the evolution of the full depletion voltage is displayed in figure 3.8. The measurement time at room temperature was at any point less than 15 minutes and thus annealing effects at room temperature can in a first approach be neglected.

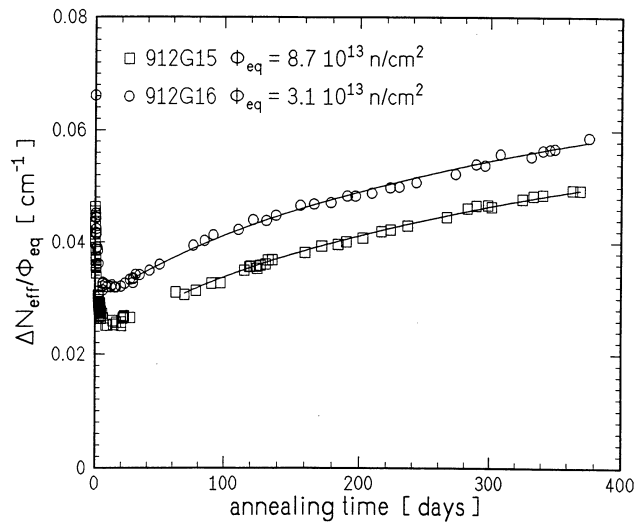


Figure 3.7: Annealing of N_{eff} of two irradiated diodes at room temperature from [26].

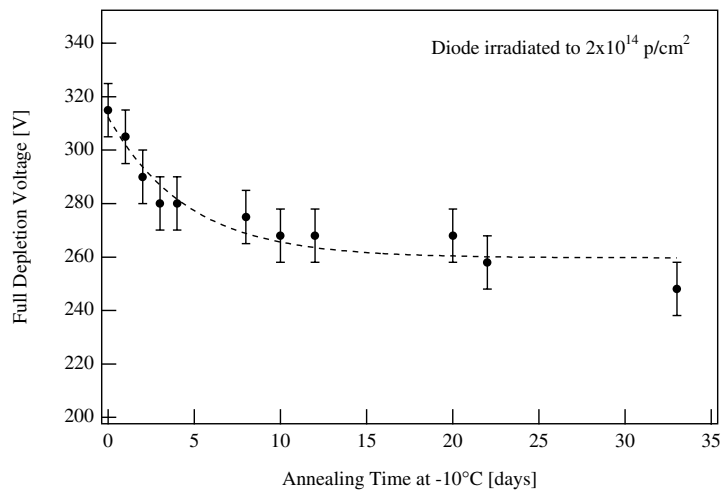


Figure 3.8: Annealing of the full depletion voltage at $-10^{\circ}C$ of a diode irradiated to 2×10^{14} protons/cm².

The annealing is clearly slowed down and after a month there is no sign of reverse annealing yet.

As a result of reverse annealing the full depletion voltage V_{fd} can eventually increase beyond the stable operation voltage of the detector. High bias voltages due to reverse annealing can reach values below the stable operation point of the detector where current breakdown occurs. Therefore it was suggested to operate the inner detector of ATLAS at low temperatures. This will halt the effect of reverse annealing and additionally decrease the radiation induced leakage current. The suggested operating temperature is $-7\text{ }^{\circ}\text{C}$ [8]. However, the yearly maintenance periods where the inner detector has to be warmed to room temperatures will significantly increase V_{fd} . The planned warm-up scenario and results of an annealing study on irradiated prototype detectors are presented in section 3.5.

3.3.3 Interstrip Resistance

After type inversion the n-bulk material behaves as p-type silicon which influences the interstrip resistance that is separating the strips from each other. Measurements carried out on detectors with p^+ implanted strips after neutron and proton irradiations have shown a decreased interstrip resistance with changes of approximately one to two orders of magnitude observed after irradiation to 1×10^{14} neutrons/cm² [35]. The irradiated devices still remain functional with sufficient interstrip resistance values (3-5 M Ω after 1×10^{14} neutrons/cm²). It is believed that the material is not inverted at the surface. The presence of positive charges located in the oxide layer above the strip causes the formation of an electron accumulation layer underneath the silicon-oxide interface. The strips are also ohmically separated by this inversion layer.

3.3.4 Interstrip Capacitance

Investigations of the effect of radiation on the interstrip capacitance have been carried out by the RD20 collaboration [35] using electrons, gammas, protons and neutrons. During the electron irradiation an increase of the interstrip capacitance of approximately 20% was observed up to 1 Mrad total dose. With further increasing dose the interstrip capacitance remained almost constant. This has been verified for several different strip geometries. A very similar behaviour has been observed in gamma irradiations up to 2 Mrad. An increase of about 10-20% has been observed for 500 krad proton irradiations. The presence of additional oxide charges and the related electron accumulation layer leads to a deformation of the electric field between the strips and thus to a change of the interstrip capacitance.

3.3.5 Bias Resistors

Polysilicon resistors have been shown to be relatively radiation hard. However, irradiation studies carried out with photons and protons have shown increases in the resistor values of 15% with 1 Mrad gammas and 10% with 2×10^{14} p/cm² [36]. The increase is believed to be related to the production of fixed oxide charges underneath and on top of the resistor.

3.4 Radiation Damage Models

The change in the effective doping concentration is well described by the creation of acceptors and the compensation of donors. Time-independent and time-dependent changes in N_{eff} are observed. The change in N_{eff} can thus be described as

$$\Delta N_{eff}(\phi, t, T) = N_{eff,0} - N_{eff} = N_b(\phi, t, T) + N_c(\phi) + N_Y(\phi, t, T) \quad (3.6)$$

where $N_{eff,0}$ denotes the original effective doping concentration, N_b describes the beneficial annealing or short term annealing, N_c is related to the time-independent change in N_{eff} and N_Y describes the reverse annealing or long term annealing.

This assumption has been confirmed by many experimental data [25, 27] and is the basis for the Hamburg model and the Zioc parametrization described in the following sections.

3.4.1 The Hamburg Model

The model developed by a group from the University of Hamburg describes the time and temperature dependence of the reverse annealing observed on highly irradiated detectors [26, 25]. The basic idea is that the reverse annealing is produced by the transformation of originally electrically inactive defects into acceptor like states. As a consequence, ΔN_{eff} is expected to saturate at a given level when all inactive defects have been transformed.

The stable radiation induced doping concentration N_c is independent of the annealing time and is parameterised as

$$N_c(\phi) = N_{c,0} \left[1 - \exp(-c\phi) \right] + g_c \phi \quad (3.7)$$

The right hand term implies the introduction of acceptor like states as a function of fluence. The exponential term describes the compensation of the original donor concentration which can be identified with $N_{c,0}$. However, for

Parameter	Value
c	$2.29 \times 10^{-13} \text{ cm}^2$
$N_{c,0}$	$1.96 \times 10^{11} \text{ cm}^{-3}$
g_c	$1.77 \times 10^{-2} \text{ cm}^{-1}$
g_Y	$4.60 \times 10^{-2} \text{ cm}^{-1}$
k_0	$1.9 \pm 1.2 \times 10^{16} / \phi \text{ cm}^3/\text{s}$

Table 3.1: Parameters used by the Hamburg model [8, 25].

fluences ϕ_{eq} larger than 10^{13} n/cm^2 the exponential term can be neglected and N_c can be simplified to:

$$N_c(\phi) \approx N_{c,0} + g_c \phi \quad (3.8)$$

To parameterise the reverse annealing a second order approach is used. Electrically inactive defects X_1 and X_2 are assumed which interact with each other forming an electrical active defect Y. The concentrations $N_{X1,0}$ and $N_{X2,0}$ of the inactive defects are proportional to the fluence. For simplicity it is assumed that $N_{X1,0} = N_{X2,0} = N_{X,0}$. The creation of the active defect Y leads to a decay of $N_{X,0}$. The concentration of the defect Y can thus be described as

$$N_Y(t) = N_{X,0} \left[1 - \frac{1}{1 + k N_{X,0} t} \right] \quad (3.9)$$

k is the rate constant of the decay and is defined as

$$k = k_0 \exp(-E_a/k_B T) \quad (3.10)$$

E_a is the activation energy, k_B is the Boltzmann constant, and k_0 is a constant related to the phonon frequency in the lattice. Via k the active defect concentration N_Y is strongly temperature dependent.

N_Y will saturate at the concentration level $N_{X,0}$ for $t \rightarrow \infty$. $N_{X,0}$ can therefore be identified with $N_{Y,\infty} = g_Y \phi$, where g_Y is referred to as the reverse annealing introduction rate.

The parameters used by the Hamburg model and the experimentally determined values are given in table 3.1.

Recent studies [25, 30] have indicated that the reverse annealing could possibly be due to a first order process. This is under investigation and has not yet been completely confirmed.

3.4.2 The Ziock-Parameterisation

The Ziock parametrisation [27] is based on experimental results from irradiations of silicon diodes. A set of photo-diodes and standard diodes was irradiated with 800 MeV and 647 MeV protons to different fluences. The maximum fluence achieved was 1.5×10^{14} p/cm². The full depletion voltage was determined with C-V measurements carried out at 10 kHz at different annealing temperatures and times. The Ziock parametrisation describes the annealing of the full depletion voltage V_{fd} in a simple model in terms of two annealing time constants which depend exponentially on the temperature. This exponential dependence is based on the annealing results obtained at different temperatures. The short term (beneficial) annealing depends on the time constant τ_S . It can be related to the exponential decay of radiation induced acceptors to neutral defects. The beneficial annealing of V_{fd} at time t after the end of the irradiation is described by:

$$V_{fd}(t) = V_Z + V_S \exp(-t/\tau_S) \quad (3.11)$$

V_Z is related to the fraction of the acceptor concentration after irradiation which is stable, V_S is related to the meta stable acceptor concentration which decays with time and τ_S is the short term annealing constant.

Extracting τ_S from a series of measurements at various temperatures between -10 °C and 21 °C yields an exponential expression as a function of temperature.

$$\tau_S(T) = 70 \cdot \exp(-0.175 \cdot T) \quad (3.12)$$

V_Z and V_S depend on the fluence ϕ and can be expressed as:

$$\begin{aligned} V_Z &= \nu_Z \phi \text{ where } \nu_Z = 1.06 \times 10^{-12} \text{ Vcm}^2 \\ V_S &= \nu_S \phi \text{ where } \nu_S = 1.34 \times 10^{-12} \text{ Vcm}^2 \end{aligned} \quad (3.13)$$

The constants ν_Z and ν_S have been determined from measurements at different fluences.

The reverse annealing part (long term annealing) is described by the following expression:

$$V_{fd}(t) = V_Z + V_A \left[1 - \exp(-t/\tau_L) \right] \quad (3.14)$$

V_A is related to a concentration of defects that can become active acceptor sites and is defined as $V_A = \nu_A \phi$, where $\nu_A = 3.8 \times 10^{-12}$ V/cm². τ_L is the long term annealing constant and is defined as:

Temperature (°C)	τ_L (days)	τ_S (days)
-15	89359	966.3
-10	41790	402.8
-7	26487	238.3
+22	323	1.5
+23	277	1.3
+25	204	0.9

Table 3.2: Short and long term annealing time constants at various temperatures.

$$\tau_L(T) = 9140 \cdot \exp(-0.152 \cdot T) \quad (3.15)$$

Table 3.2 shows the short and the long term time constants at different temperatures. The long term constants are generally much bigger than the short term constants which leads to a long term constant of almost 73 years in the case of -7 °C, the operational temperature of ATLAS.

The exponential behaviour of the anti-annealing can therefore be approximated in the short term by a linear dependence of τ_L .

$$V_{fd}(t) \approx V_Z + \frac{V_A t}{\tau_L} \quad (3.16)$$

An assumption of the Ziock parametrisation is that V_S , V_Z and V_A are independent of the temperature and depend linearly on the fluence. Comparing this to the Hamburg model the same assumption is found, namely that the stable defect concentration N_c and the concentration of defects that will become active $N_{X,0}$, only depend on the fluence.

The second basic assumption of the Ziock parameterisation is that the time constants only depend on the temperature and not on the fluence.

Similar to the Hamburg model the Ziock parametrisation predicts a saturation of V_{fd} for $t \rightarrow \infty$. The saturation depletion voltage is given by $V_Z + V_A = V_U = \nu_U \phi$, where $\nu_U = 4.78e-12 \text{ Vcm}^2$, determined experimentally.

The overall annealing behaviour of V_{fd} after irradiation described by the Ziock parametrisation using above definitions and equations is expressed as:

$$V_{fd}(t) = V_Z + V_S \exp(-t/\tau_S) + V_A \left[1 - \exp(-t/\tau_L) \right] \quad (3.17)$$

Plotted in figure 3.9 are the predictions of the Ziock parameterisation and the Hamburg model for V_{fd} at 25 °C. The fluence was set to $2.1 \times 10^{14} \text{ cm}^{-2}$,

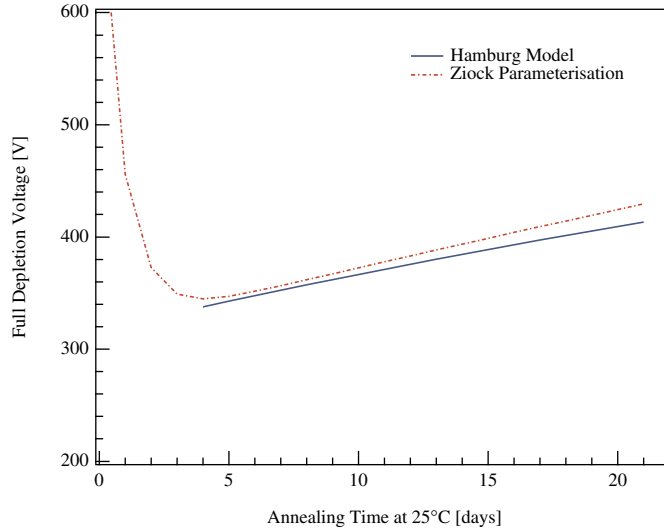


Figure 3.9: Annealing of the full depletion voltage as predicted by the Hamburg model and the Ziock parameterisation after a fluence of $2.1 \times 10^{14} \text{ cm}^{-2}$.

which corresponds to the 1 MeV neutron fluence expected in ATLAS. In order to express the Hamburg model in term of the full depletion voltage a $300 \mu\text{m}$ thick detector with an initial V_{fd} of 50 V was assumed. The activation energy E used to calculate k for the Hamburg model was set to 1.31 eV.

Both models give a very similar description of the anti-annealing. The offset from the x-axis of the Hamburg model does also depend on the initial V_{fd} . In the case of an initial V_{fd} of 50 V the Hamburg model and the Ziock parameterisation predict almost the same voltages.

It has to be emphasised that a comparison of V_{fd} on diodes from different manufacturers indicates a standard deviation of 150 V of the data after $2 \times 10^{14} \text{ 1MeV neutrons/cm}^2$ [37]. These measurements and the results presented in the following section indicate that the measured values can show a significant deviation of the predicted ones, which do not take any spread into account. The predicted values on figure 3.9 have to be seen in the context of the measured values obtained on different diodes and the detectors presented in section 3.5.3 and the observed spread in V_{fd} . The general trend of V_{fd} after irradiation as a function of time is described qualitatively by the presented parameterisation and model. However, a spread in V_{fd} on different detectors all irradiated to the same fluence has been observed which is not included in these parametric descriptions.

3.5 Results from ATLAS Prototype Detectors

A study was carried out on ATLAS prototype detectors to investigate the performance of detectors which have received the maximum ATLAS fluence. The results of this study are presented in the following chapter.

3.5.1 Detector Baseline

The basic structure of the ATLAS SCT is introduced in section 1.3. The barrel and forward disks consist of detector modules that are constructed of 4 silicon detectors and frontend chips mounted on a hybrid. The highest fluences in the SCT after 10 years of operation will reach values of $\approx 2 \times 10^{14}$ 1 MeV equivalent n/cm².

Due to the large area of the SCT the detector design has not only to be cost effective but also highly fault tolerant. It will be difficult to replace defective detectors during operation and therefore the system operation time has been set to at least 10 years.

In 1996 n-in-n detectors were chosen as the baseline detectors for ATLAS to ameliorate problems due to the high fluence expectations. P-in-n detectors were chosen as the backup solution [8]. In the following a few important features and parameters of n-in-n and p-in-n detectors are listed. Displayed in figures 3.10 and 3.11 are the schematic cross sections of n-in-n and p-in-n detectors.

n-in-n Detectors:

- Assuming the worst case, the detectors will have to sustain equivalent fluences of $\approx 2 \times 10^{14}$ 1 MeV n/cm². As explained in section 3.3.2 after type inversion the junction is located on the strip side from where the detector depletes. It has been demonstrated that fully inverted n-in-n detectors can be operated partially depleted. Compare also figure 4.40, where the results from a testbeam with irradiated p-in-n and n-in-n detectors connected to binary electronic are presented.
- The partially depleted operation of the detectors limits the overall power consumption of the system, but results in decreased signal to noise ratio.
- Compared to a p-in-n detector the production cost for a n-in-n detector is more than two times higher due to double sided processing. Most of the production costs are due to the number of photo-masks required. For n-in-n detectors approximately 11 masks are required while the production of p-in-n detectors necessitates the use of 5-6 masks.
- Due to the double sided processing the yield will decrease thus increasing the costs.

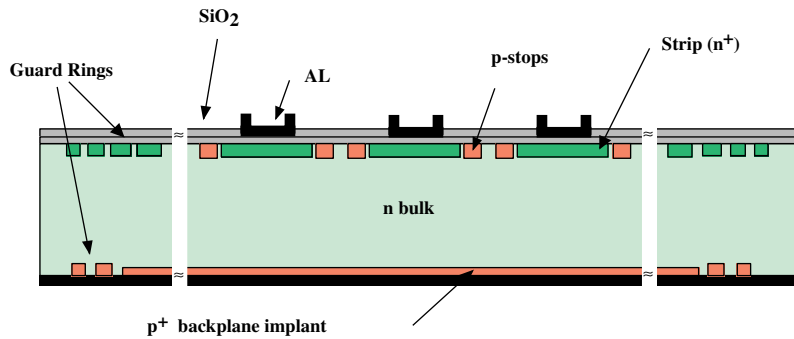


Figure 3.10: Schematic cross section of a n-in-n detector.

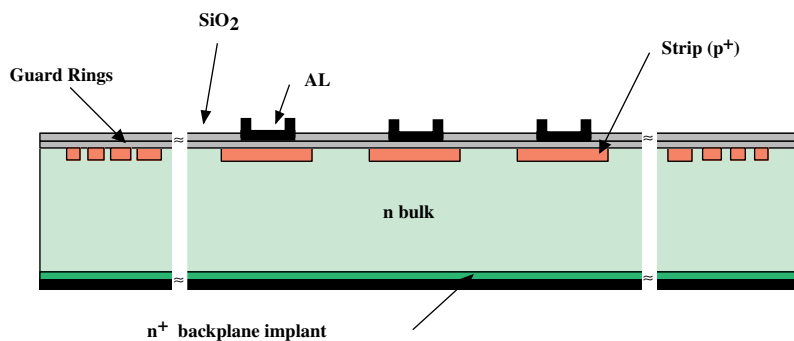


Figure 3.11: Schematic cross section of a p-in-n detector.

The structure of n-in-n detectors is somewhat more difficult as p^+ -implants have to be placed between the strips to avoid shorts between the strips. These p^+ -implants can either be individual p-stops where one p-frame surrounds each strip, or common p-stops where all frames around the strips are connected together, or p-spray implants.

p-in-n Detectors:

- The efficiency decreases for voltages below V_{fd} faster than for n-in-n detectors, see figure 4.40. Therefore operational voltages close to V_{fd} are desired.
- P-in-n detectors can be produced in single sided processes which increases the yield.
- The costs for p-in-n detectors are less than half of n-in-n detectors due to the simpler process.

Taking into account the above mentioned points it was decided to study the performance of highly irradiated p-in-n and n-in-n detectors. For this

Total Area	$64 \times 63.6 \text{ cm}^2$
Active Area	$62 \times 61.6 \text{ cm}^2$
Readout Strips	768+2
Strip Implant Width	18 μm
Strip Implant Length	62 mm
Strip Pitch	80 μm
Thickness	$300 \pm 15 \text{ }\mu\text{m}$

Table 3.3: Basic specifications of the ATLAS barrel prototype detector.

purpose a selection of detectors from different manufacturers was tested, irradiated at CERN and annealed in 1997.

Most of the detectors irradiated were produced as barrel detectors. Their basic properties are summarised in table 3.3.

The wedge type detectors followed the same specifications apart from the different geometry. The design of the forward wheels necessitates this special shape. A more detailed list of the specifications can be found in [8].

3.5.2 Pre-Irradiation Results and Detector Irradiation

Prototype detectors were delivered to different ATLAS institutes, tested and mounted there and then sent to CERN for the irradiation. At CERN a batch of p-in-n and n-in-n detectors from SINTEF [38] was received, tested and mounted.

SINTEF Detectors

SINTEF produced a batch of ATLAS barrel prototype detectors according to the specifications in table 3.3. All detectors were produced on $\langle 100 \rangle$ silicon wafers from TOPSIL. The wafers all originate from the same ingot with a resistivity of $\approx 5 \text{ k}\Omega\text{cm}$.

Some parameters of the detectors differ from the original specifications or were not specified at all and are therefore decided by the designer. On the detectors from SINTEF the implant width of the strips was 16 μm instead of the specified 18 μm . A multiguard structure of 6 guard rings was used on the p-in-n detectors, while the multiguard ring of the n-in-n detectors included 10 guard rings on the strip side. On the backside of the n-in-n detector the same guard ring design as for the p-in-n detectors was used. For the coupling capacitance the n-in-n detectors used a nitride and a SiO_2 layer, while the p-in-n detectors used SiO_2 only. Apart from this the p-in-n and n-in-n batch can be regarded as practically identical.

Fourteen n-in-n and 8 p-in-n detectors were delivered to CERN in August 1997. Leakage current measurements were carried out on all detectors to

n-in-n detectors	
$I_{total} <$	6 μ A at 150 V 100 μ A at 300 V
p-in-n detectors	
$I_{total} <$	6 μ A at 150 V 20 μ A at 300 V 100 μ A at 500 V

Table 3.4: Current specifications for ATLAS detectors.

see whether they meet the ATLAS pre-irradiation specifications, which are listed in table 3.4.

The total leakage current measurements of all SINTEF detectors that were chosen for the irradiation are shown in figure 3.12 and 3.13. Only detector n62 meets the specifications at 150 V, but all n-in-n detectors meet the specifications at 300 V. From the group of p-in-n detectors detector p16 exceeds all specified values, while all other p-in-n detectors meet the specifications. The measurements on the p-in-n detectors were only carried out to 400 V as at the time of the measurement the specifications for p-in-n detectors for ATLAS were not yet published.

Interstrip capacitance measurements were carried out on several p-in-n detectors. The interstrip capacitance to the nearest neighbours was found to be between 7.8 pF and 8.2 pF for the full strip length. These values are relatively high for the given configuration. Measurements have been carried out at various frequencies up to 100 kHz with no significant change.

The aluminium line resistance has been tested on a few detectors and was found to be 70-80 Ω for the full length. This is in accordance with the ATLAS specifications. The resistivity of the Al lines represents a series noise source and thus low values are desired.

The C-V measurements of all p-in-n detectors gave a value of V_{fd} of 50-60 V. The values for the n-in-n detectors were generally a bit lower, between 40 and 55 V, which can be accounted for by the different design on the strip side. On the n-in-n detectors the p-stops will lead to a different field configuration between the strips which also affects the depletion voltage.

The detectors were separated into two groups. Detectors p7, p15, p17, n9, n62 and n70 were irradiated to the maximum fluence of 3×10^{14} p/cm². Detectors p9, p16, n34 and n42 were irradiated to 1×10^{14} p/cm².

In the previous irradiations the detectors were glued onto ceramics to be mounted in the irradiation area. However, removing the detectors from the ceramic is not possible after irradiation as this would involve heating. At high temperatures the annealing of V_{fd} is accelerated so the time development can no longer be studied. A new mounting system was developed to be

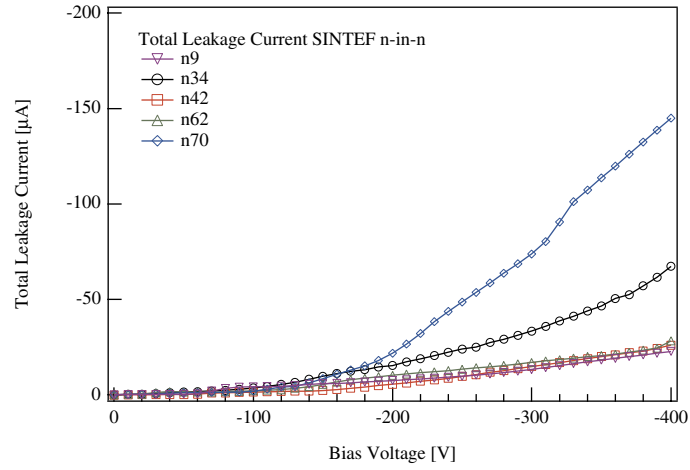


Figure 3.12: Pre-irradiation total leakage currents of the SINTEF n-in-n detectors selected for irradiation.

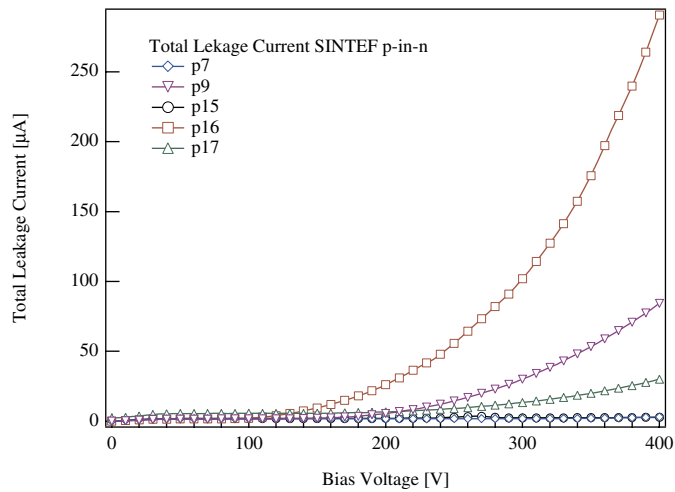


Figure 3.13: Pre-irradiation total leakage currents of the SINTEF p-in-n detectors selected for irradiation.

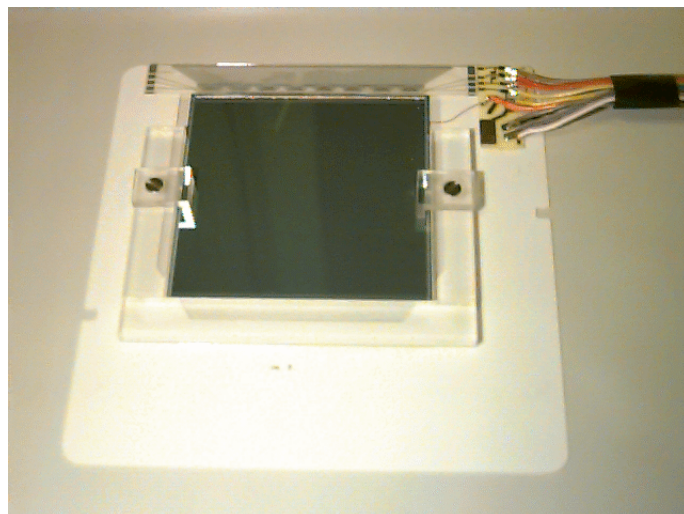


Figure 3.14: New mounting frame developed for the SINTEF detectors.

able to reuse the SINTEF detectors after irradiation without the ceramic, e.g. when bonding the detector to a readout chip. A picture of a mounted detector is shown in figure 3.14.

In order to keep the strips at the same potential and to avoid a voltage difference between the implant and the aluminium of the strips, all strips were bonded to ground.

Detector Irradiation

A total of 39 detectors from 5 different manufacturers (Canberra, Eurysis, Hamamatsu, MPI and SINTEF) were irradiated in the CERN PS with 24 GeV protons. The detectors were mounted on ceramics and placed in an aluminium box where they were kept at -8 ± 1 °C throughout the irradiation. Except for two detectors (Hamamatsu S10 and S21) all detectors had their strips bonded to ground. The detectors were biased at 150 V and the current was monitored during irradiation. The irradiation was carried out at low temperatures in order to simulate the ATLAS operational conditions.

Figure 3.15 shows the schematic setup in the irradiation area. A proton beam is extracted from the CERN PS every 14 s into the T7 test-facility. As the beam size is only approximately 1 cm wide and 2 cm high the detectors have to be scanned to ensure uniform irradiation over the whole area. For this purpose the box is placed on an x-y stage which enables scanning of the detectors.

In approximately 300 hours irradiation a total fluence of 3×10^{14} p/cm² was achieved. This corresponds to a 1 MeV neutron fluence of 2.1×10^{14} n/cm², which is the maximum fluence expected in the SCT taking into

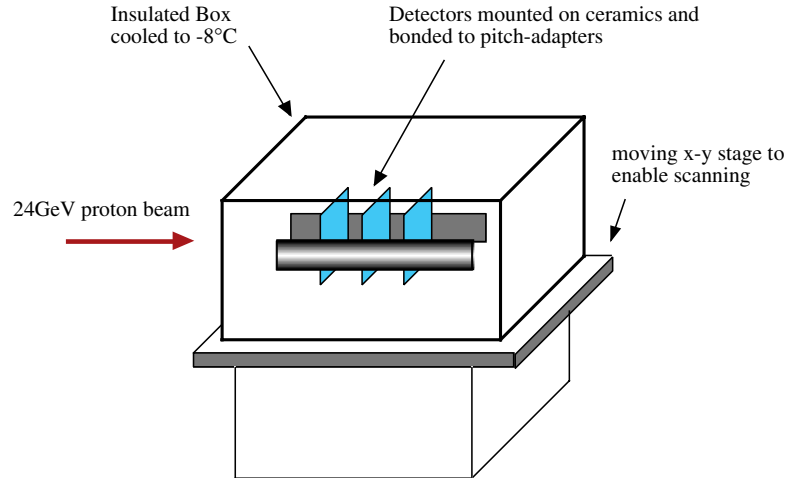


Figure 3.15: Schematic setup of the T7 irradiation.

account a 50% safety margin defined in the TDR, and using a hardness factor $\kappa = 0.7$.

The fluence was determined from activation measurements of aluminium foils [39]. The number of protons registered in an ionisation chamber was used as a cross reference. The error of the fluence calculation using aluminium foils has previously been determined to be in the order of 6% [40]. Immediately after irradiation all detectors were stored in a freezer at $-10\text{ }^\circ\text{C}$.

3.5.3 Annealing Study of Irradiated Prototype Detectors

The operational conditions of the ATLAS SCT detector are presented in the ATLAS TDR [8]. It is foreseen to operate the SCT at $-7\text{ }^\circ\text{C}$ to reduce annealing effects and the radiation induced leakage current. However, maintenance periods have to be taken into account. The TDR foresees a yearly maintenance scenario of

2 days at $20\text{ }^\circ\text{C}$ and 2 weeks at $17\text{ }^\circ\text{C}$

The effect of this warm up over the 10 year operation can be simulated on a shorter time scale by using a radiation damage model or parameterisation. The ATLAS SCT community agreed to use the Ziocck parameterisation as the time constants are directly expressed as a function of temperature. The same amount of anti-annealing as achieved in 10 years with the above described scenario can be reached by annealing the detectors at a higher temperature for a shorter time [41], see table 3.5. Shown in figure 3.16 is prediction of V_{fd} using the Ziocck parameterisation for $25\text{ }^\circ\text{C}$. As is well illustrated in figure 3.35 the Ziocck parameterisation is quantitatively not describing the

10 years with TDR scenario compares to:	45 days at 20°C
	21 days at 25°C
	10 days at 30°C

Table 3.5: Warm-up times assuming the 10 year scenario proposed in the ATLAS inner detector Technical Design Report [8].

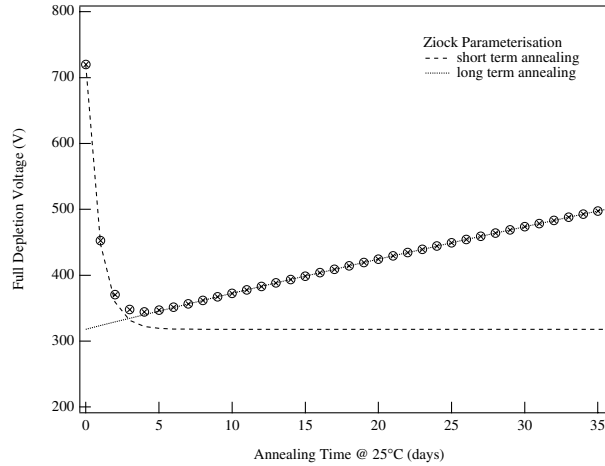


Figure 3.16: Prediction of the Ziock Parameterisation for 25 °C. The short term annealing is indicated by a broken line and the long term annealing by a solid line.

data. The general trend is well described, but the predicted level of V_{fd} is too high.

A selection of 9 detectors, representing all available types of p-in-n and n-in-n detectors, was chosen to undergo the annealing study. The aim of this study was to investigate the time evolution of the main detector parameters, such as leakage current and full depletion voltage as a function of annealing time up to the amount of anti-annealing expected after 10 years of LHC. Up to now annealing studies have mainly been carried out on diodes. The use of a full size prototype detector simulates the real case and allows the influence of the more complicated design and process to be seen. Shown in table 3.6 are the basic parameters of the 9 selected detectors.

Detectors n70 and p17 were produced by SINTEF. H97-4, Wedge 12-1, Hamamatsu S10 and Hamamatsu S21 were produced by Hamamatsu. The MPI 7 detector, produced by MPI, the Canberra 71 detector, produced by Canberra and the Eurysis 80 detector, produced by Eurysis used all the same design provided by the MPI Munich.

	d [μm]	Pass.	Type	Biasing	P-Stops	V_{fd}
n70	300	none	n-in-n	poly	individual	42 V
p17	300	none	p-in-n	poly	-	55 V
H97-4	300	silox	n-in-n	poly	individual	60 V
Wedge 12-1	300	silox	n-in-n	poly	individual	50 V
MPI 7	280	none	p-in-n	implant	-	100 V
Canberra 71	310	none	p-in-n	poly	-	60 V
Eurysis 80	340	none	p-in-n	implant	-	40 V
S10	300	silox	n-in-n	poly	common	70 V
S21	300	silox	n-in-n	poly	common	70 V

Table 3.6: Information on detectors selected for the annealing where d is the detector thickness.

All detectors apart from the Hamamatsu Wedge 12-1 detector were designed as barrel type detectors. Except for detector MPI 7 which was produced on 2 k Ωcm resistive silicon, all detectors were produced on high resistive material (4-6 k Ωcm).

Taking into account the various thicknesses of the detectors, all data presented were corrected to 300 μm . The leakage current was scaled linearly and the full depletion voltage according to the square root of the thickness.

After two weeks storage at -10 $^{\circ}\text{C}$ in a freezer the 9 detectors were moved to a climate cabinet allowing temperature control with an accuracy of 0.1 $^{\circ}\text{C}$. A setup was installed which allowed the measurement of the leakage currents and the full depletion voltage inside the cabinet. A Keithley 237 source/measurement unit was used to apply the bias voltage and to measure the total leakage current with an accuracy in the order of 100 nA. A Keithley 617 electrometer was used to measure the guard ring leakage current on those detectors where the guard ring contact could be accessed. The C-V measurements were carried out using an HP4263B LCRmeter. The measurements were controlled by LabView programs.

The detectors were stored together in the climate cabinet at 25 $^{\circ}\text{C}$ and I-V and C-V measurements were carried out regularly on all detectors. To reduce the high leakage current after irradiation the climate cabinet was cooled to -10 $^{\circ}\text{C}$. At the end of the annealing period some of the detectors were prepared for a testbeam so that part of their warm-up was taking place at temperatures other than 25 $^{\circ}\text{C}$. These times were normalised to 25 $^{\circ}\text{C}$ using the following relation:

$$\frac{\text{days at T1}}{\tau_L(\text{T1})} = \frac{\text{days at } 25^{\circ}\text{C}}{\tau_L(25^{\circ}\text{C})} \quad (3.18)$$

The temperature in the cabinet was monitored by an internal temperature sensor and a Pt100 placed next to the detector. The temperature in the

cabinet is specified to be accurate to 0.1 °C. To test the temperature monitoring the leakage current of detector Wedge 12-1 was measured at various temperatures, see figure 3.17.

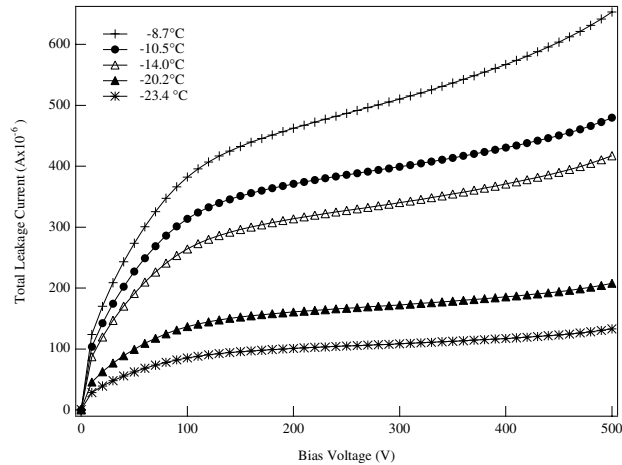


Figure 3.17: I-V curve of detector Wedge 12-1 at various temperatures after 12 days at 25 °C.

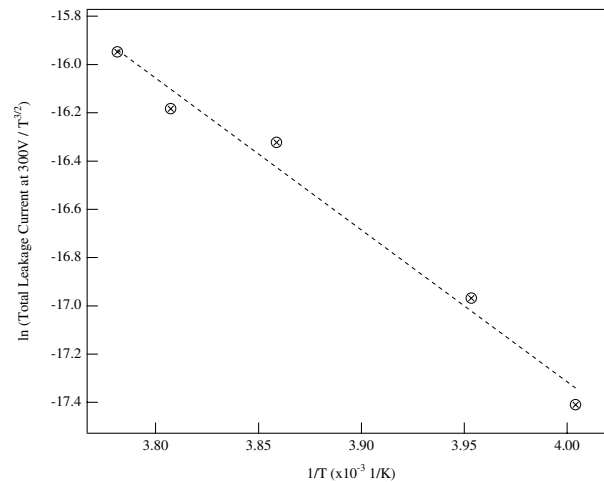


Figure 3.18: Total leakage current of detector Wedge 12-1 at 300 V at various temperatures.

According to equation 2.2 the leakage current depends exponentially on the temperature. Figure 3.18 shows an Arrhenius plot of the leakage current of detector Wedge 12-1 at 300 V.

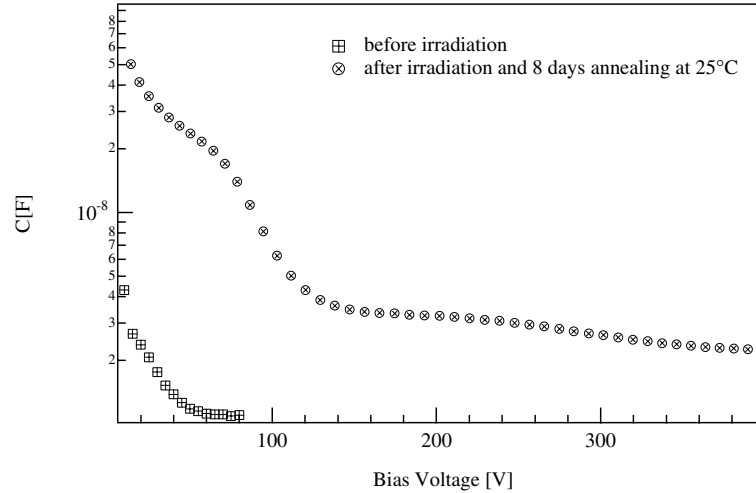


Figure 3.19: C-V characteristic measured on detector p17 before and after irradiation at 100 Hz.

Any self-heating would be indicated by a deviation of the data from the linear relation. The fit results in an activation energy of 1.15 eV. The linear relation indicates that no self heating is present and that the temperature monitoring system is reliable.

C-V Measurements

For non-irradiated detectors no significant frequency dependence of the form of the C-V curve and the full depletion voltage has been observed. This changes drastically after irradiations to higher fluences. Figure 3.19 shows the C-V measurements carried out on detector p17 before and after irradiation and partial annealing of the detector. Both measurements were carried out at 100 Hz. It is important to note that the measurement before irradiation was carried out at room temperature while after irradiation the C-V characteristic had to be measured at -10 °C due to the high leakage current. The temperature dependence of the C-V characteristic will be discussed at a later stage in this chapter.

The C-V characteristic after depletion differs strongly from the pre-irradiation curve indicating the influence of defects in the bulk and in the oxide [42].

The presence of defects in the bulk causes a frequency dependence of the space charge region. High frequencies require a fast response of the defect to the AC signal. Deep levels cannot follow the high frequencies fast enough due to their large distance to the conduction band and the valence band. For

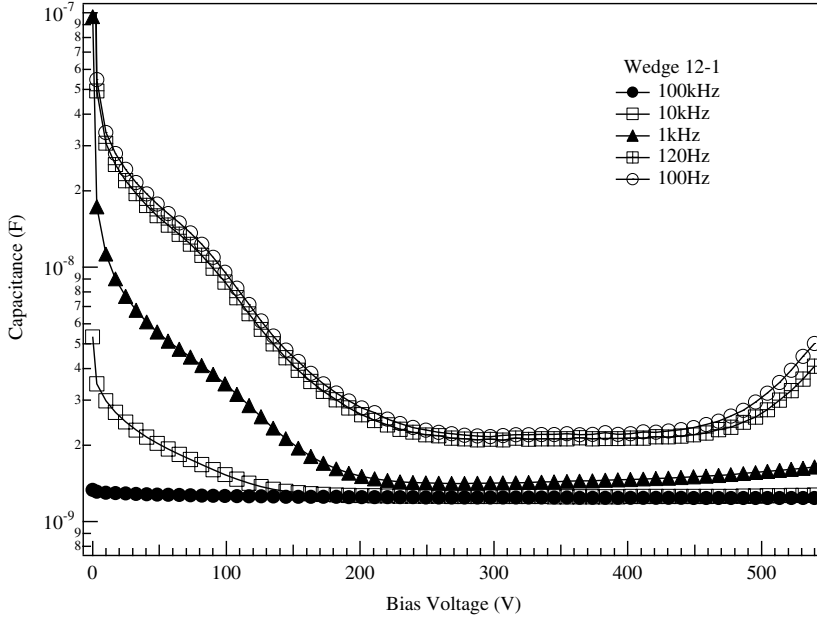


Figure 3.20: C-V characteristic of the Wedge 12-1 detector carried out at different frequencies after 17 days of annealing at 25 °C.

low capacitances these defect centres will therefore cause a deviation of the $V^{-1/2}$ dependence of the capacitance [28]. This is illustrated in figure 3.20, where the C-V characteristic of the Wedge 12-1 detector was measured at different frequencies.

At low voltages the C-V curve is influenced by the oxide charges present. The first part of the C-V curve shows the same frequency dependent behaviour as a MOS structure after irradiation [28].

Measurements on the Wedge 12-1 detector carried out at 100 Hz and at different temperatures as shown in figure 3.21, suggest that the C-V curve is not only frequency dependent, but also temperature dependent. In the observed time regime the temperature dependence is not very pronounced. Measurements over a wider temperature range were not possible due to the leakage current and the setup. However, a change in form and level can clearly be observed. This temperature dependence of the C-V curve is related to the temperature dependence of the individual defects present in the bulk.

The frequency and temperature dependence not only affects the form of the C-V curve but also the extracted full depletion voltage V_{fd} . By using a HP4284A LCRmeter it was possible to carry out measurements at frequencies of 20 Hz, 30 Hz, 80 Hz, 100 Hz, 200 Hz, 500 Hz and 1 kHz.

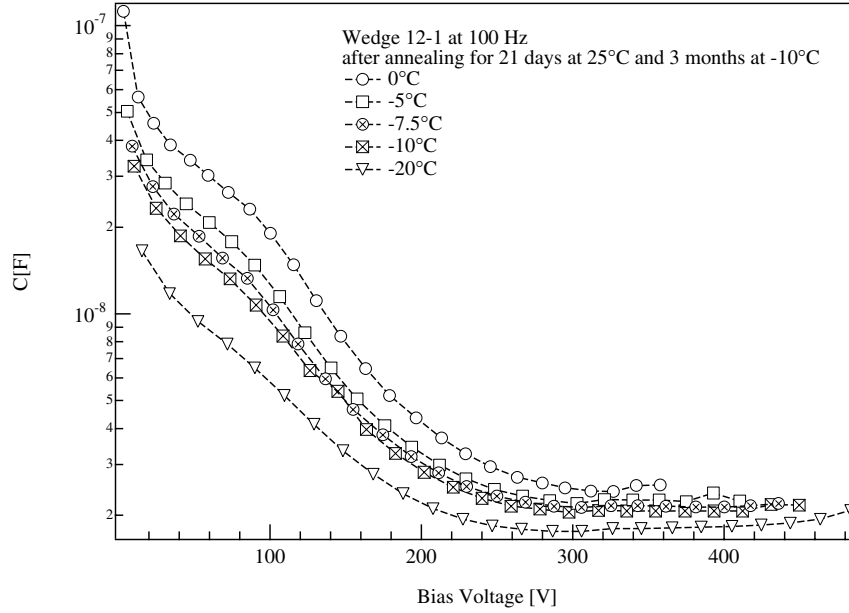


Figure 3.21: C-V characteristic of detector Wedge 12-1 at 100 Hz measured at different temperatures.

V_{fd} of detector Wedge 12-1 was measured as a function of temperature and frequency after annealing of 21 days at 25 °C and storage in a freezer at -10 °C for 3 months. V_{fd} was determined from C-V measurements by fitting lines to a region of decreasing capacitance at low voltages and a region of almost constant capacitance at higher voltages. V_{fd} is defined as the intersection of these lines. A maximum uncertainty of ± 10 V is estimated due to the fitting procedure. Measurements were carried out between 0 °C and -20 °C.

Figure 3.22 displays the dependence of V_{fd} as a function of temperature for different frequencies. The data suggest a small decrease of V_{fd} with decreasing temperature. This behaviour has been observed in previous publications where the measurements could be carried out over a larger temperature range due to small diodes being used [43]. In this case the study was carried out on a full size ATLAS prototype detector. The high leakage current prevents measurements at higher temperatures and thus the temperature behaviour is not very well pronounced. The mean decrease of V_{fd} over the 20 K range is $9.5 \pm 3\%$ for all frequencies. This corresponds to a change in V_{fd} of 28.1 ± 10 V and is in accordance with the observation on diodes in [43].

Figure 3.23 shows V_{fd} plotted as a function of measurement frequency for three different temperatures varying exponentially with frequency.

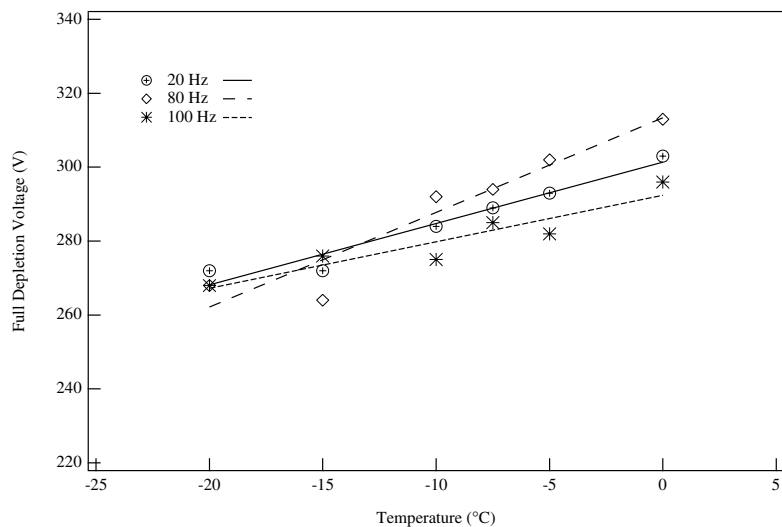


Figure 3.22: V_{fd} of detector Wedge 12-1 as a function of temperature for lower frequencies.

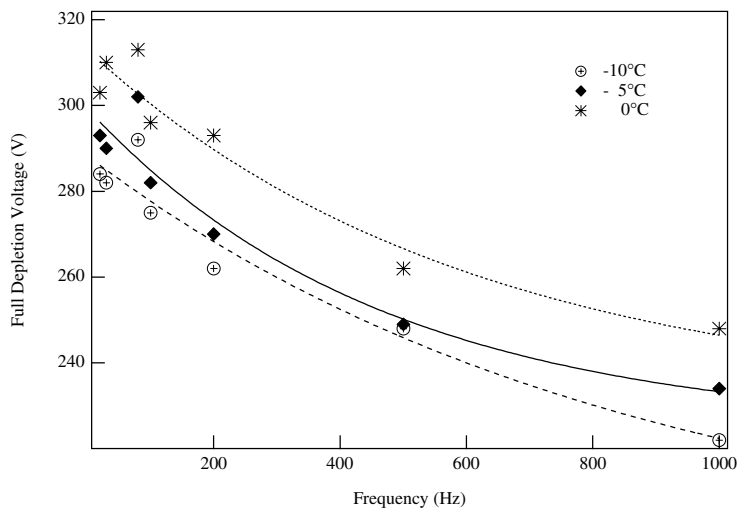


Figure 3.23: V_{fd} of detector Wedge 12-1 as a function of frequency at three different temperatures.

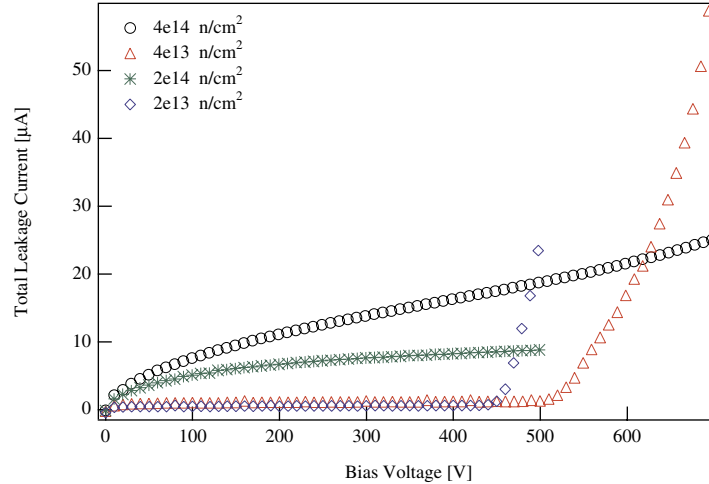


Figure 3.24: I-V curves of diodes irradiated in a reactor to four different fluences measured at $-10\text{ }^{\circ}\text{C}$.

The mean change in V_{fd} between 20 Hz and 1 kHz has been determined to be $59\pm 10\text{ V}$. This corresponds to a relative change of $20.0\pm 3.4\%$. The exponential behaviour of V_{fd} as a function of frequency has been previously observed by Beattie [43]. Contrary to the results on the Wedge 12-1 detector these studies were again carried out on diodes. Also the measurements in [43] were carried out in a higher frequency range between 1 kHz and 100 kHz.

The variation of V_{fd} at very low frequencies between 20 and 100 Hz is within the error of the measurement for all measured temperatures. Thus no significant difference between 20 Hz and 100 Hz has been observed.

To study the frequency dependence of V_{fd} at different fluences four p-in-n diodes produced by SINTEF were irradiated in a TRIGA reactor in Ljubljana with fast neutrons to fluences of $2\times 10^{13}\text{ n/cm}^2$, $4\times 10^{13}\text{ n/cm}^2$, $2\times 10^{14}\text{ n/cm}^2$ and $4\times 10^{14}\text{ n/cm}^2$. The diodes were irradiated at room temperature without bias for about one day and then transported to CERN where the measurements were carried out. During the transport the diodes were annealing at room temperature for approximately 3 days. Figure 3.24 shows the leakage currents of the diodes measured at $-10\text{ }^{\circ}\text{C}$ on their arrival at CERN. Note that for the two highest fluences no breakdown is visible.

Figure 3.25 shows V_{fd} of the four diodes measured at different frequencies as a function of fluence.

The fluence displayed is the fast neutron fluence and has to be multiplied with the hardness factor $\kappa=0.9$ [44] to achieve the 1 MeV equivalent fluence. The neutron fluence corresponding to $2.1\times 10^{14}\text{ 1 MeV/cm}^2$ is $2.3\times 10^{14}\text{ fast neutrons/cm}^2$.

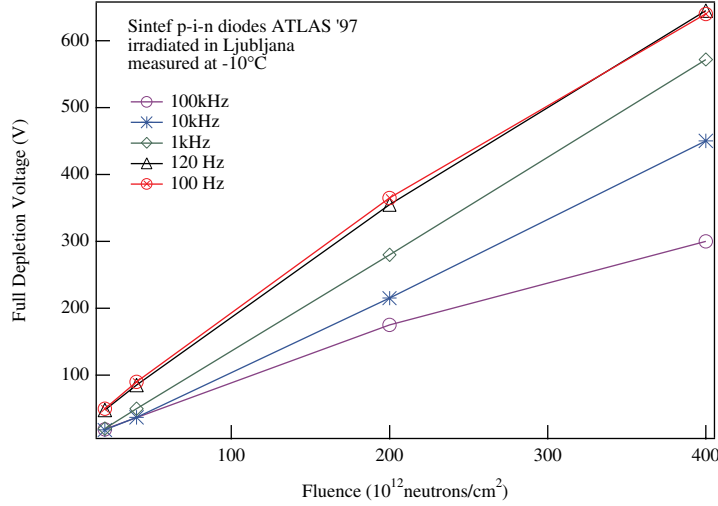


Figure 3.25: V_{fd} measured on diodes irradiated in a TRIGA reactor to four different fluences using different measurement frequencies.

Note that V_{fd} changes more with frequency at higher fluences as more deep defects are introduced which show a stronger response to low-frequent AC signals.

Leakage Current Measurements

During irradiation I-V curves were measured at 1.2×10^{14} p/cm 2 and at the end of the irradiation. In the irradiation area only the total leakage current could be measured. The damage constant α has been determined for five detectors according to equation 3.4 at 300 V. The values for α were obtained for all detectors and normalised to 300 μ m and to 20 °C. The mean value of α of all detectors at 20 °C is $2.83 \pm 0.24 \times 10^{-17}$ A/cm taking into account the errors on the fluences and the leakage current measurements. The data have not been corrected for self-annealing since the detectors were kept at -8 °C throughout the irradiation and annealing effects are thus assumed to be negligible. The obtained mean value of α is in accordance with recently quoted data of 2.5×10^{-17} A/cm [45].

At the end of the irradiation the detectors were left in the cold box for a few days to decrease their activity. The activation is mainly due to ^{24}Na produced in the reaction of protons with silicon and ^7Be which is a spallation product of silicon. The ^{24}Na decays quickly with a half life time of ≈ 12 hours. The ^7Be has a half life time of ≈ 50 days and therefore determines the long term activity.

Before the detectors were removed from the irradiation area I-V curves were taken on most of the detectors, shown in figure 3.26.

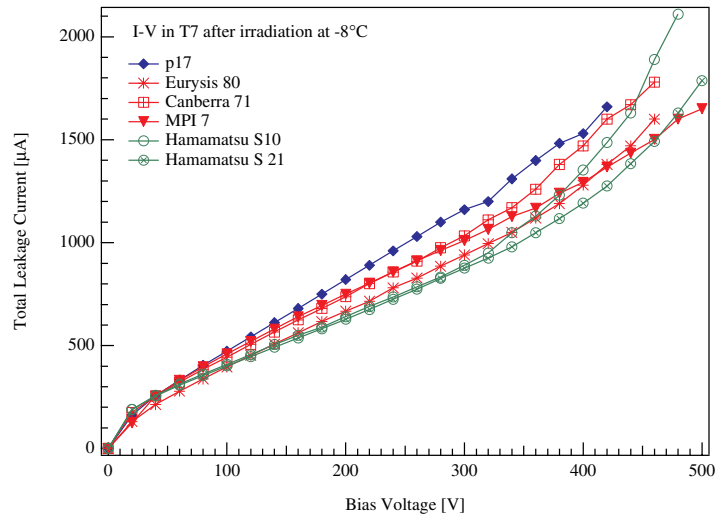


Figure 3.26: I-V curve taken at the end of the irradiation in T7 at -8 °C.

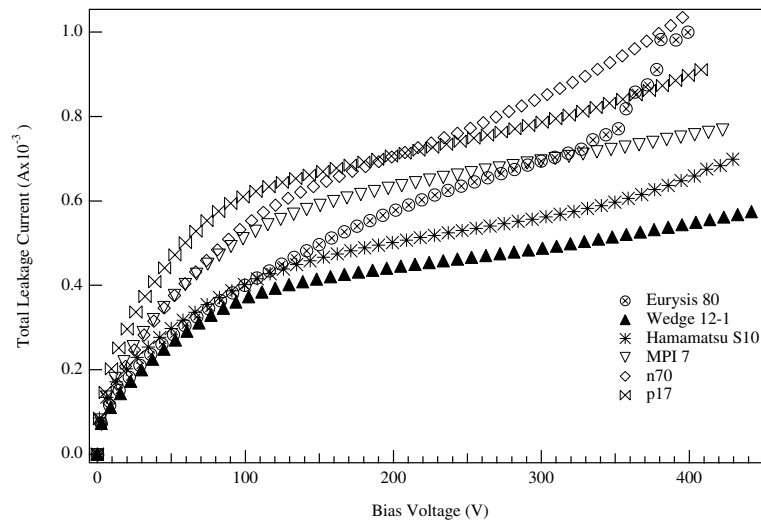


Figure 3.27: Total leakage current measured after 9.3 days of annealing at 25 °C.

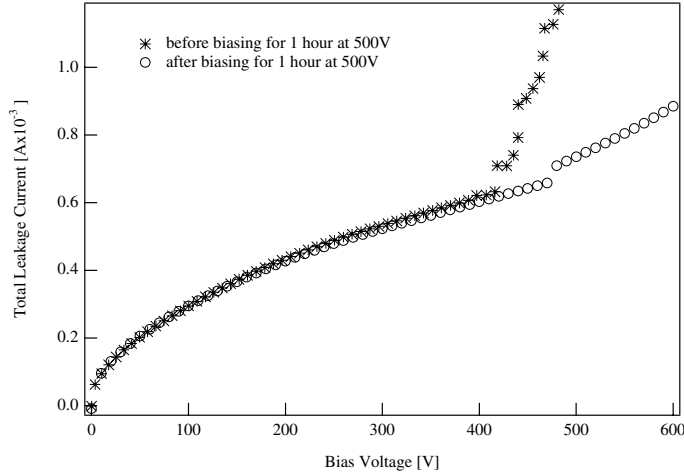


Figure 3.28: Total leakage current of detector Eurysis 80 before and after biasing at 500 V for one hour.

Detector	V_{fd} (V)	Total Current (μA)
Eurysis 80	288	685
Wedge 12-1	235	458
Hamamatsu S10	305	562
MPI 7	295	690
n 70	245	760
p 17	145	662

Table 3.7: V_{fd} from CV-measurements and total leakage current at V_{fd} measured after 9.3 days of annealing at 25°C.

After irradiation the detectors were annealed for 21 days at 25 °C. Figure 3.27 shows the total leakage current of 6 detectors in the annealing after 9.3 days. As can be seen from this plot the leakage current of all detectors is stable up to more than 400 V. The forms of the I-V curves indicate that bulk currents are the dominating currents.

Only detector Eurysis 80 shows indication of soft breakdown around 370 V. This is due to glue on the surface and the edge of the detector and had already been observed before irradiation. The effect can be reduced by biasing the detector for some time at a high voltage. The I-V curve appears to be much stabler afterwards as can be seen in figure 3.28.

The values of the total leakage current at V_{fd} taken from plot 3.27 are Listed in table 3.7.

It has to be noted that the currents are between 458 μA and 760 μA .

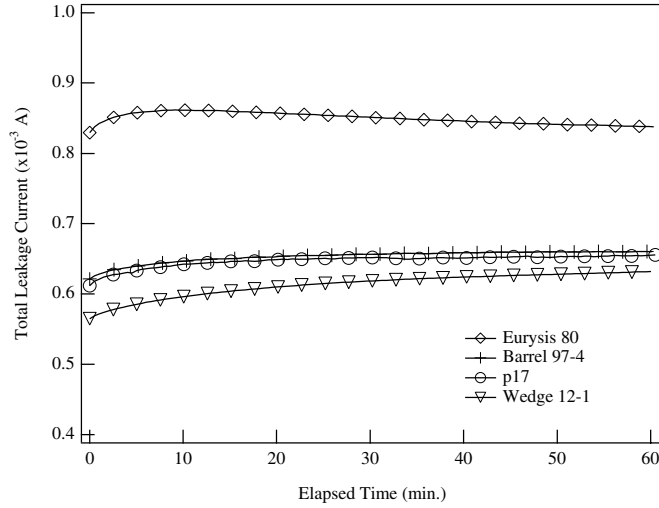


Figure 3.29: Current stability measurements at $-10\text{ }^{\circ}\text{C}$ at 500 V bias.

Before irradiation the currents of all these detectors were comparable, and were about $<8\text{ }\mu\text{A}$ at 150 V at room temperature. Normalising the currents to room temperature gives values of a few mA. This results in a significant increase in noise and eventually self heating and thermal runaway.

Stability measurements were carried out to investigate the current evolution as a function of time. Due to the limited time that was available for all measurements, the stability measurements were only carried out for one hour. However, as can be seen in figure 3.29 all measured detectors behave extremely well at 500 V bias voltage. The measurement was carried out at $-10\text{ }^{\circ}\text{C}$ after annealing of approximately 17 days at $25\text{ }^{\circ}\text{C}$. All detectors have been optimised in design and production for high voltage operation which is illustrated by the stable behaviour.

The leakage current was monitored on all detectors throughout the annealing at $25\text{ }^{\circ}\text{C}$. The total leakage current at 400 V measured at different annealing times is shown in figure 3.30. Not all detectors show a smooth evolution with time which is mostly due to the short time available for the measurements. Immediately after the annealing a testbeam was carried out with six of these detectors, so that those detectors had to be prepared in parallel for the electronic tests. It was also observed that a more stable and generally lower current was measured if the detectors were stored at $-10\text{ }^{\circ}\text{C}$ for a few hours and then biased at a higher bias voltage for again a few hours. This is also apparent from the stability tests carried out. However, due to the time constraints it was not always possible for all detectors to undergo above mentioned preparations which is reflected in the data points in figure 3.30.

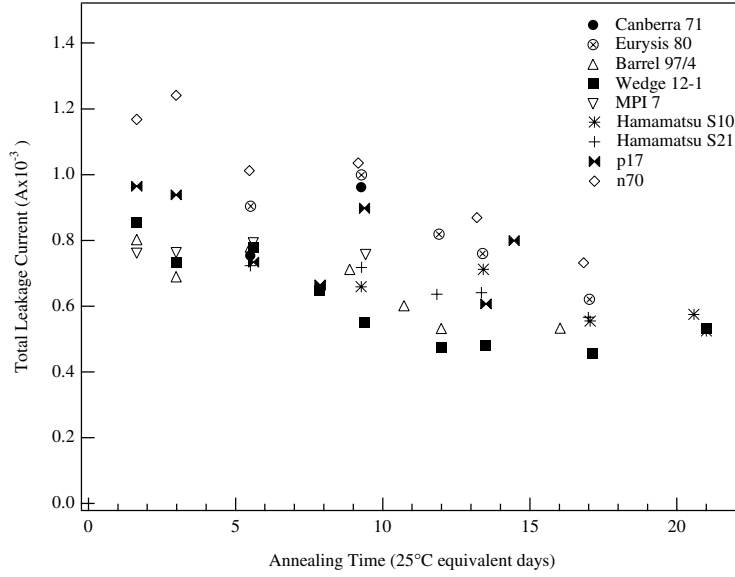


Figure 3.30: Total leakage current at 400 V measured at $-10\text{ }^{\circ}\text{C}$ and normalised to $300\text{ }\mu\text{m}$ as a function of annealing time at $25\text{ }^{\circ}\text{C}$.

During the annealing study an annealing of the current has been observed on all detectors. For the Wedge 12-1 detector a current annealing of $\approx 40\%$ could be observed between day 2 and day 21 of the annealing. This detector was not selected for a testbeam and could therefore be measured over the full annealing time.

As can be seen from figure 3.31 the dominant part of the leakage current is the current from the active area. The measurement was carried out on detector p17 after 7.9 days at $25\text{ }^{\circ}\text{C}$. Both currents are stable up to about 400 V. The biasline current shows a characteristic bulk current form with no indication of breakdown.

The guard ring and the biasline leakage current could be measured separately on detector p17 throughout the annealing. That was not possible on all detectors due to different designs. The guard and biasline leakage currents of the SINTEF p17 detector for different annealing times are shown in figures 3.32 and 3.33. Both currents decrease with annealing time. Comparing the biasline current before and after irradiation the change in form is obvious. The soft breakdown visible before irradiation has completely disappeared. This has also been observed on an irradiated diode, see figure 3.5. The guard ring current does not change its characteristic to the same extent. The increase of the guard ring current after irradiation is much less compared to the increase of the current of the active volume, where the current level changes from a few μA to a few hundred μA .

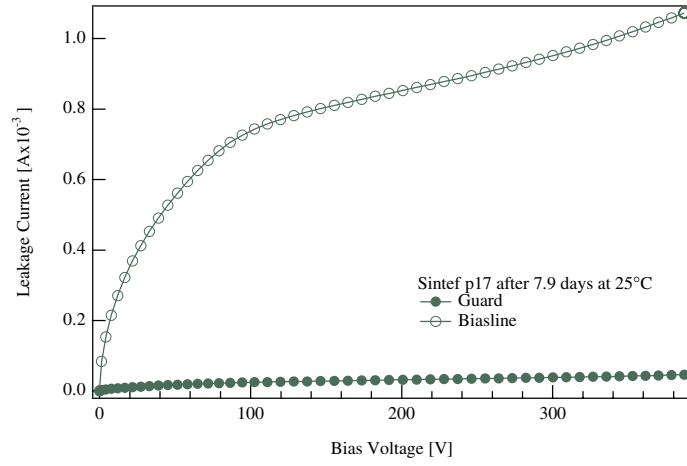


Figure 3.31: Leakage current of detector p17 measured at $-10\text{ }^{\circ}\text{C}$ after 7.9 days annealing at $25\text{ }^{\circ}\text{C}$.

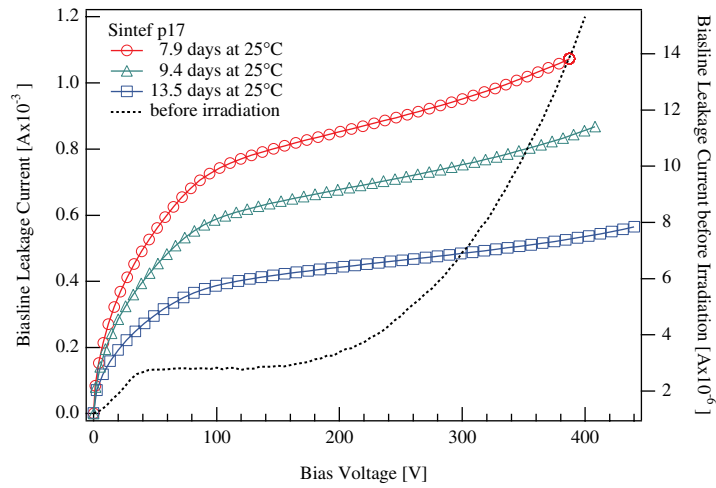


Figure 3.32: Bias leakage current before irradiation and after 7.9 days of annealing at $25\text{ }^{\circ}\text{C}$.

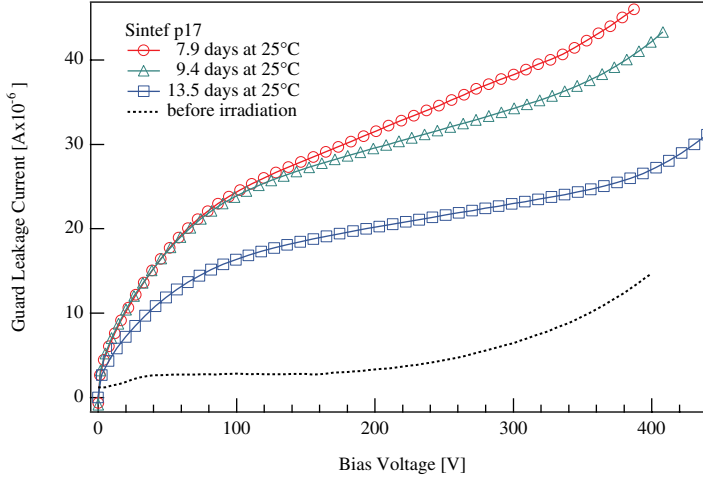


Figure 3.33: Guard leakage current before irradiation and after 7.9 of days of annealing at 25 °C.

Annealing of the Full Depletion Voltage

The full depletion voltage of the detectors included in the study was measured throughout the annealing period at 25 °C at regular intervals. All measurements were carried out under the conditions described above at -10 °C. To ensure the best possible determination of V_{fd} all measurements were carried out at 100 Hz/500 mV which is the lowest frequency available on the HP4263B.

As discussed in section 3.5.3 V_{fd} changes with temperature and measurement frequency. It is therefore emphasised that all detectors were measured at the same frequency and temperature during the annealing. It is therefore possible to compare the obtained values for V_{fd} of all detectors except for detector MPI 7 which was produced with lower resistivity material. Figure 3.34 shows V_{fd} as a function of annealing time at 25 °C.

Missing data points are due to parallel electronic tests on some of the detectors. Six of these detectors were measured in a testbeam immediately after the annealing, so that the preparations of this testbeam had to be carried out in parallel. At 9.3 days of annealing, data from all detectors are available.

Comparing the data from those detectors that were produced at high resistive bulk material, detector Hamamatsu S10 shows the highest V_{fd} of 310 V. Detector p17 has the lowest value of V_{fd} of 150 V. The maximum spread in V_{fd} is thus 160 V. As all detectors were handled together and measured under the same conditions it is assumed that this value spread is due to

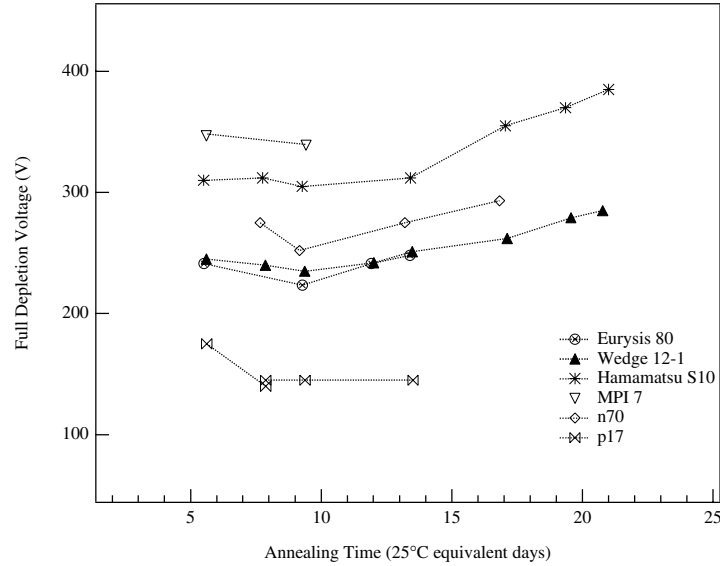


Figure 3.34: Full depletion voltage measured at -10 °C and normalised to $300 \mu\text{m}$ as a function of annealing time at 25 °C.

design and process differences. This is especially pronounced for detector Wedge 12-1 and Hamamatsu S10, which are both n-in-n detectors produced by Hamamatsu, but with differences in designs and under different conditions. A comparison of several measurements of V_{fd} at different fluences on diodes from different manufacturers has shown that at $2 \times 10^{14} \text{ 1 MeV n/cm}^2$ a spread of 150 V is the 1σ range of the data [37]. The spread of the data in figure 3.34 is in accordance with this observation.

V_{fd} could be measured for the Wedge 12-1 and the Hamamatsu S10 detector over the entire annealing period up to 21 days. Using the Ziock parameterisation (see section 3.4.2), fits were applied to the data and are shown in figure 3.35. Due to the relatively short time scale the approximation described in equation 3.16 was used for the fit. This does also reduce the number of free parameters for the fit. Starting values for the fit were taken from [27] and are summarised in table 3.8. Due to the lack of data points at short times a meaningful fit to τ_S was not possible and τ_S was therefore fixed to 2 days. This value is about twice as high as the predicted value from Ziock, but was used to account for the minimum in V_{fd} being reached after 8 days and not 4 days as predicted.

The fit was applied using the Levenberg-Marquardt algorithm [46] which is an algorithm for non-linear least square fits. The limited number of data points and the relatively short annealing time lead to a low number of degrees of freedom. Some of the parameters are highly correlated such as V_A and

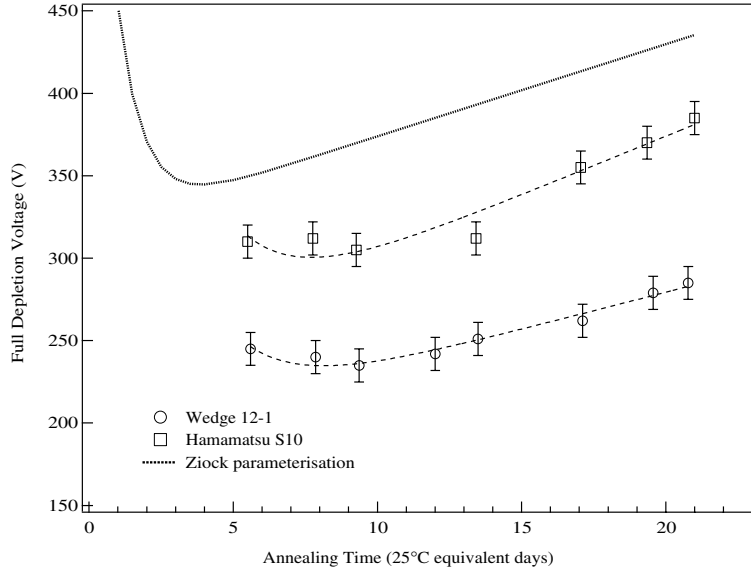


Figure 3.35: Annealing of the full depletion voltage after irradiation. The data have been fitted using the Ziock parameterisation.

V_Z . This results in large errors on the fitted parameters, shown in table 3.8.

From figure 3.35 it is evident that the Ziock parameterisation does not describe the data points. The predicted values of V_{fd} from [27] are generally higher than the measured data points. The minimum of V_{fd} should be around 350 V, while the measured values at the minimum are between 240 V and 310 V. This can only partially be explained by the fact that the measurements were carried out at -10 °C. Over the 30 K difference to room temperature an increase in V_{fd} of approximately 15% (see section 3.5.3) would be expected. Taking this increase into account the minimum in V_{fd} of detector Hamamatsu S10 would be very similar to the predicted minimum around 350 V. However, for the detector Wedge 12-1 the Ziock prediction

	Ziock Value	Wedge 12-1	Hamamatsu S10
V_Z	318V	189 ± 16 V	231 ± 18 V
V_S	402V	529 ± 269 V	676 ± 274 V
V_A/τ_L	5.59V/d	4.52 ± 1.02 V/d	7.14 ± 1.07 V/d
τ_S	2d		
χ^2/ndf	-	0.6/5	4.1/4

Table 3.8: Values from Ziock [27] and fit parameters for annealing at 25°C. The short term constant τ_S has been fixed to 2 days.

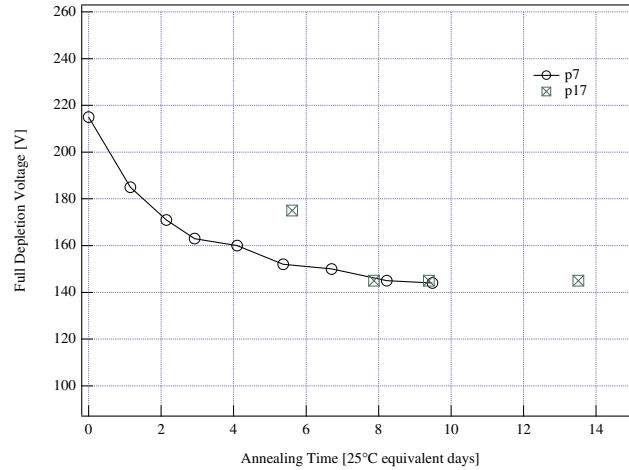


Figure 3.36: Annealing of V_{fd} of detectors p17 and p7.

would still be higher by about 60-70 V. The minimum in the data appears around day 8 of the annealing while the Ziock parameterisation predicts it around day 4.

The parameter values obtained from the fit are only partially in agreement with those found by [27]. V_Z does not agree with the value found by [27] which reflects the generally lower level of V_{fd} . V_S is in statistical agreement, but has very large errors due to the missing data points. The parameter describing the long term annealing $V_A/\tau L$ is for both detectors statistically compatible with that found by [27].

Looking at the Ziock prediction for 25 °C shown in figure 3.35 and the range of curves in figure 3.34 it is clear that the Ziock parameterisation is too simple a model to describe the behaviour of complicated detector structures and to provide a universal function for annealing of all detector types. Different initial doping concentrations, surface effects, geometric effects and in particular process technology differences between different manufacturers are not considered. However, all detectors follow the general trend of a decrease in V_{fd} at short times followed by a slow increase in V_{fd} with increasing times.

An interesting result of the annealing was that the detector p17 showed a relatively low full depletion voltage (150-180), while the n-in-n detector also produced by SINTEF shows a 100 V higher depletion voltage. Three p-in-n detectors produced by SINTEF were irradiated together to 3×10^{14} p/cm² in T7. A second detector, p7, was in the following annealed for a couple of days at 25 °C under the same measurement conditions as detector p17. The result of the annealing of detector p7 is shown in figure 3.36.

3.5.4 Conclusions

The maximum fluence expected in the ATLAS silicon strip detectors is 2.1×10^{14} 1 MeV neutrons/cm², taking into account a safety margin of 50%. This will cause severe bulk and surface damage in the silicon. Up to now no final model which describes this damage has been developed. Attempts to describe the anti-annealing of the full depletion voltage have been undertaken by a group from Hamburg University [25]. Another parameterisation describing beneficial- and anti-annealing was developed by Ziock [27]. Intensive studies are being undertaken at the moment [30] to find a model which fully describes the effects of high fluence irradiations in silicon.

To simulate the effects of the highest fluence expected in ATLAS irradiations were carried out on full size ATLAS prototype detectors. The irradiation was carried out at low temperature (-8°C) as foreseen in the TDR [8].

A selection of p-in-n and n-in-n detectors from various manufacturers were chosen to undergo an annealing study which simulated the warm-up periods necessary to maintain the ATLAS detector within 10 years. This study has to be regarded as a worst case study. At the beginning of the study n-in-n detectors were defined as the baseline detectors and p-in-n were chosen as a backup solution.

The Ziock parameterisation was used to define an accelerated annealing program which produces the same amount of anti-annealing as after 10 years of ATLAS operation. During 21 days the detectors were then stored at 25°C. C-V and I-V measurements were carried out at regular intervals. Generally, no systematic difference in leakage current and full depletion voltage was found between n-in-n and p-in-n detectors [47, 48, 49]. Furthermore the full functionality of p-in-n and n-in-n detectors after irradiation connected to binary readout electronics could be shown in a testbeam, see figure 4.40. Finally, in December 1997 the ATLAS baseline was changed to p-in-n detectors as the functionality of p-in-n detectors could be demonstrated and they can be produced at lower cost.

The full depletion voltage as a function of time follows in general the Ziock prediction. A spread of ≈ 160 V in V_{fd} was found between the detectors in the study. This is in accordance with previous observations on diodes [37]. However, the Ziock parameterisation is too simple a model which does not take into account pre-irradiation parameters, surface effects or design differences. It does not provide a universal description of the annealing of different detector types.

From the measurements a frequency and temperature dependence of the C-V measurements and the obtained V_{fd} was found and carefully investigated [47, 48, 49]. This behaviour reflects the introduced damage in the silicon. The obtained results are in agreement with previous studies on diodes. Measurements carried out on diodes irradiated to different fluences

show a stronger change of V_{fd} with frequency at higher fluences. This is related to more deep defects being introduced in the material.

Separate measurements of the guard and the biasline leakage current have shown that the main current contribution comes from the bulk region. Breakdown or instabilities that were observed before irradiation are not visible anymore after irradiation.

Chapter 4

Frontend Readout Systems for ATLAS

Contents

4.1	Charge Collection and Signal Readout	72
4.1.1	Charge Sensitive Preamplifier	79
4.1.2	Ballistic Deficit	84
4.1.3	Spatial Resolution and Noise	86
4.2	Readout Systems	89
4.3	Analog and Binary Readout Systems	90
4.3.1	Analog Readout	90
4.3.2	Binary Readout	92
4.4	The SCT32A Analog Frontend Chip	93
4.4.1	SCT-A Layout and Functionality	93
4.4.2	Noise Performance	97
4.4.3	Source- and Pulse-Setup for the SCT32A in the Laboratory	98
4.5	Results from an ATLAS prototype detector us- ing the SCT32A	102
4.5.1	Source Tests	104
4.5.2	Testbeam Results	110
4.6	Source tests with an irradiated ATLAS proto- type detector using the SCT32A	118
4.7	Conclusions	126

In the following chapter some basic principles of the readout of silicon detectors, such as charge collection and charge sensitive preamplifiers are discussed. Special emphasis is laid on the ballistic deficit for fast shaping

times. The ballistic deficit for 25 ns shaping, as will be used in ATLAS, can lead to a loss of registered signal. In order to minimise this effect higher bias voltages for the detectors are required. A further chapter deals with the noise sources that have to be considered in a readout module. Furthermore the basic concept suggested for the ATLAS readout of the silicon tracker is introduced. As there is no definite decision taken yet whether binary (baseline) or analog (backup) frontend electronics will be used in ATLAS, both systems are shortly discussed and their advantages and disadvantages presented. The SCT-A chip and its functionality are presented as an example for an ATLAS frontend readout chip. Results from a testbeam and source measurements with an ATLAS prototype detector connected to this chip are presented. Source measurements were also carried out using a highly irradiated detector. These measurements give an insight into the problems of operating silicon strip detectors in ATLAS after 10 years of LHC.

4.1 Charge Collection and Signal Readout

Silicon detectors in high energy physics experiments are used for tracking information on particles. When a charged particle passes through a silicon detector, electron-hole pairs are produced by ionisation. The mean energy loss dE per unit length dx is described by the Bethe-Bloch formula [14].

$$\frac{dE}{dx} = 2\pi N_a r_e^2 m_e c^2 \rho \frac{Z}{A} \frac{z^2}{\beta^2} \left[\ln \left(\frac{2m_e \gamma^2 v^2 W_{max}}{I^2} \right) - 2\beta^2 - \delta - 2\frac{C}{Z} \right] \quad (4.1)$$

with r_e as the classical electron radius, m_e is the electron mass, N_a the Avogadro constant, c is the velocity of light in vacuum, ρ is the density of the absorbing material, Z is the atomic number of the absorbing material, A is the atomic weight of the absorbing material, z is the charge of the incident particle, I is the mean excitation energy, $\beta=v/c$ of the incident particle and $\gamma=1/\sqrt{1-\beta^2}$. The two last terms are the density correction term δ and the shell correction term. W_{max} is the maximum energy transfer.

Figure 4.1 shows the the energy loss rate in copper with and without corrections. Particles with energies around the minimum of the energy loss rate ($\beta\gamma \sim 2-3$) are referred to as minimum ionising particles (MIP).

The Bethe-Bloch formula describes the mean energy loss. However, for finite absorber thicknesses statistical fluctuations in the actual energy loss have to be taken into account. For thick absorbers the distribution will be Gaussian. Whereas for thin absorbers the distribution becomes asymmetric.

Silicon detectors with standard thicknesses of around 300 μm have to be regarded as thin absorbers. The Landau theory describes the energy loss in a thin absorber taking into account the probability for large energy transfers

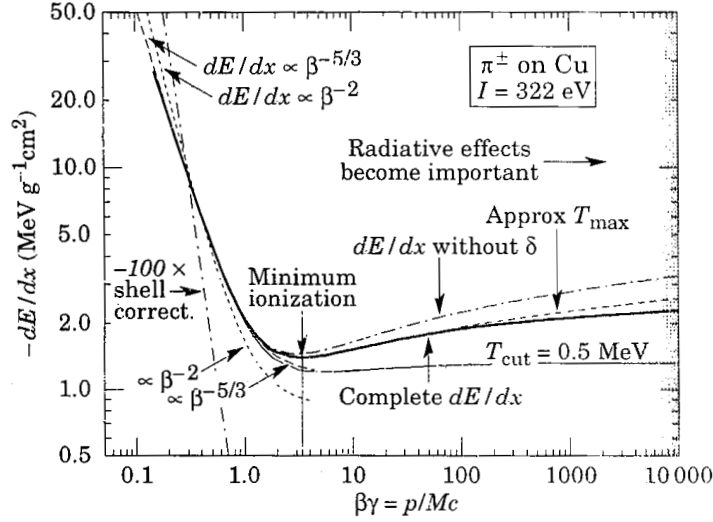


Figure 4.1: Energy loss rate in copper [11].

in a single collision. These events add a long tail on the high energy side of the energy loss probability distribution. The mean energy loss no longer correspond to the peak of probability but is shifted to higher energies. The peak is now referred to as most probable energy loss.

The electron-hole pairs created in a silicon detector, when a charged particle traverses it, represents the detectable signal and can be registered on the electrodes. Figure 4.2 shows the signal to noise ratio measured on a 300 μm thick silicon strip detector using a ^{106}Ru source with an electron energy up to 2.7 MeV.

For a MIP traversing a 300 μm thick silicon detector the most probable charge deposition is 81 keV [50]. The ionisation energy needed to create an electron-hole pair in silicon is 3.6 eV. Therefore the most probable charge deposited by a MIP in a 300 μm detector is 22500 electron-hole pairs or 3.6 fC.

The Landau theory does not take into account that the atomic electrons are rather bound than free [51] which leads to a broader distribution than predicted by Landau. A Gaussian distribution convoluted with a pure Landau distribution is used to fit the signal distributions presented here.

The charges produced in the detector volume move to the electrodes due to the applied field and diffusion. The moving charge induces a signal current in the electrode, which is a function of the motion of the charge carriers [50].

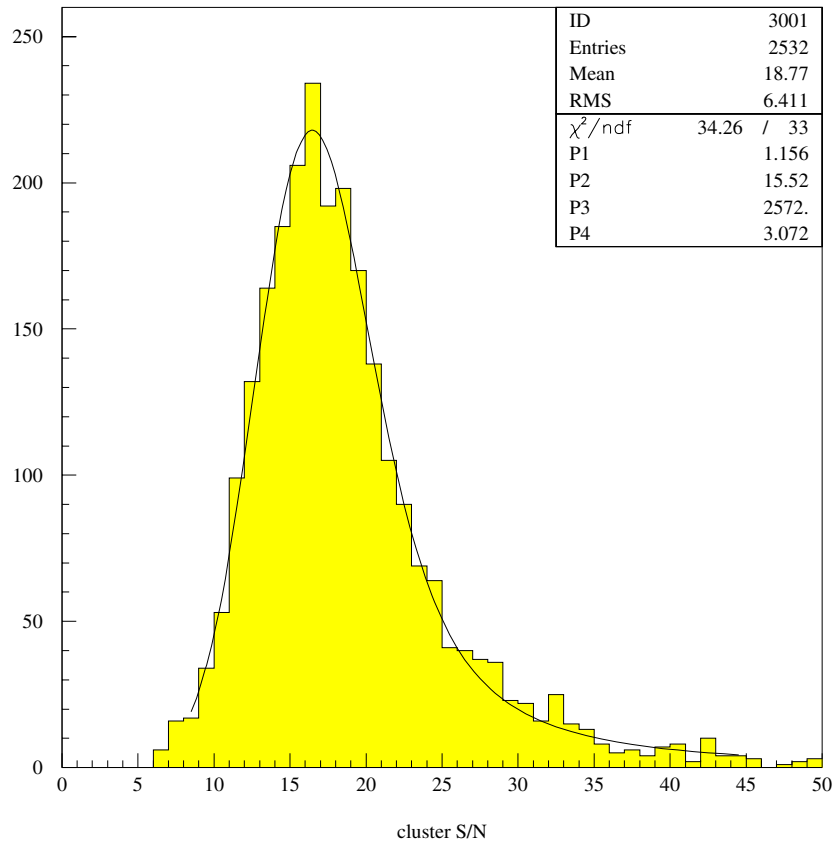


Figure 4.2: Histogram of the cluster signal to noise ratio of a 300 μm thick ATLAS prototype silicon strip detector using the SCT32A chip. The applied bias voltage to the detector is 300 V.

Both, holes and electrons contribute to the current. In the special case of a p^+-n -junction with a bias applied higher than the full depletion voltage and assuming constant carrier mobility the total current can be written as [52]:

$$\begin{aligned}
I(t) = & Q_{gen} \frac{\mu_e}{2} \left[E_{max} \left(1 + \frac{V_{od}}{E_{max}d} \right)^2 \exp\left(-\frac{\mu_e E_{max}t}{d}\right) - \right. \\
& \left. - \frac{V_{od}^2}{E_{max}d^2} \exp\left(\frac{\mu_e E_{max}t}{d}\right) \right] \sigma(t_{max}^e) \\
& + Q_{gen} \frac{\mu_h}{2} \left[E_{max} \left(1 + \frac{V_{od}}{E_{max}d} \right)^2 \exp\left(-\frac{\mu_h E_{max}t}{d}\right) - \right. \\
& \left. - \frac{V_{od}^2}{E_{max}d^2} \exp\left(\frac{\mu_h E_{max}t}{d}\right) \right] \sigma(t_{max}^h)
\end{aligned} \tag{4.2}$$

Q_{gen} is the total generated charge per unit length, $\mu_{e,h}$ are the electron and hole mobility, V_{od} is the amount of over depletion, d is the detector thickness, E_{max} is the maximum field at depletion, $t_{max}^{e,h}$ are the maximum collection times for electrons and holes. It is important to note that the diffusion of the carriers is neglected in this approximation and only the drift component due to the electric field is taken into account. The two terms only contribute to the total current as long as free carriers are present, which is accounted for by σ which is

$$\sigma(t_{max}^{e,h}) = \begin{cases} 1 & 0 \leq t \leq t_{max}^{e,h}, \\ 0 & \text{elsewhere.} \end{cases} \tag{4.3}$$

For bias voltages higher than the depletion voltage the maximum charge collection times can be expressed as

$$t_{max}^{e,h} = \frac{d}{v_{e,h}} \ln \left(1 + \frac{E_{max}d}{V_{od}} \right) \tag{4.4}$$

where $v_{e,h}$ is the drift velocity of electrons and holes, respectively. The collected charge q as a function of time can be expressed in a similar way, where d is the thickness of the detector or diode.

$$\begin{aligned}
q(t) = & \frac{Qd}{2} \left[\left(1 + \frac{V_{od}}{E_{max}d} \right)^2 \left(1 - \exp\left(-\frac{\mu_e E_{max} t}{d} \right) \right) + \right. \\
& \left. + \left(\frac{V_{od}}{E_{max}d} \right)^2 \exp\left(+\frac{\mu_e E_{max} t}{d} \right) \right] + \\
& + \frac{Qd}{2} \left[\left(1 + \frac{V_{od}}{E_{max}d} \right)^2 \left(1 - \exp\left(-\frac{\mu_h E_{max} t}{d} \right) \right) + \right. \\
& \left. + \left(\frac{V_{od}}{E_{max}d} \right)^2 \exp\left(+\frac{\mu_h E_{max} t}{d} \right) \right]
\end{aligned} \tag{4.5}$$

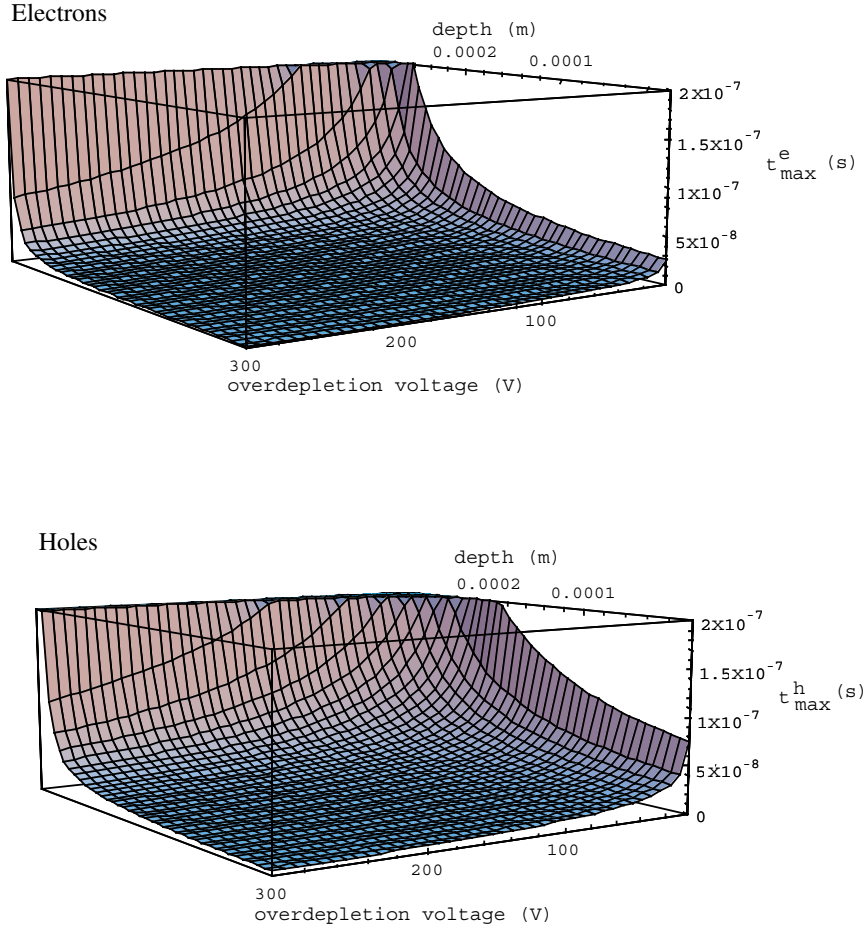


Figure 4.3: Maximum collection time of electrons and holes in 300 μm silicon as a function of over depletion voltage and depth.

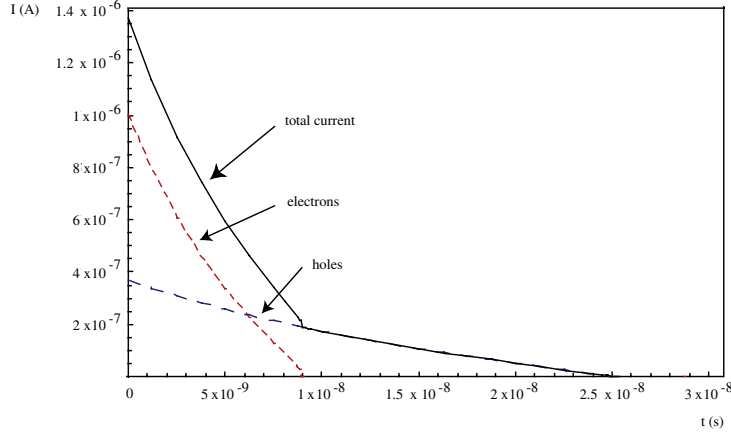


Figure 4.4: Induced current in a 300 μm thick and 30 V over depleted $\text{p}^+\text{-n}$ detector.

Assuming a 300 μm thick $\text{p}^+\text{-n}$ junction which depletes at 60V ($N_D = 8.8 \times 10^{11} \text{cm}^{-3}$) the collection time can be plotted as a function of over depletion ($V_{od} = V_{bias} - V_{fd}$) and of the position x in the detector. The mobility of electrons is $1350 \text{cm}^2/\text{Vs}$ and the hole mobility $480 \text{cm}^2/\text{Vs}$. Displayed in figure 4.3 are the collection times of electrons and holes as a function of V_{od} and x .

The collection time decreases with increasing V_{od} voltage. At $x=0$ the collection time is a minimum for each over depletion voltage as here the electric field reaches its maximum (see also equation A.10). The collection time goes to infinity for zero V_{od} . This is an artifact of the model as for no V_{od} the electric field vanishes at one side and thus the carrier velocity equals zero as no diffusion is taken into account.

The total induced current for the above described $\text{p}^+\text{-n}$ detector for $V_{od}=30 \text{V}$ is plotted in figure 4.4.

The two terms of the current described in equation 4.2 are completely symmetric only differing by the mobility of electrons and holes. Assuming a constant carrier mobility, which is a good approximation for a standard $\text{p}^+\text{-n}$ detector, the current increases with over depletion and the collection time becomes shorter as can be seen in figure 4.5. Here the sum of hole and electron current is plotted for $V_{od}=30 \text{V}$ and for $V_{od}=80 \text{V}$.

Figure 4.6 illustrates the collected charge as a function of time for a $\text{p}^+\text{-n}$ junction with above mentioned properties and $V_{od}=30 \text{V}$. The electron charge remains constant after t_e and the hole charge after t_h , respectively.

This approximation gives a first idea of the collection time and the signal shape as a function of time in a planar diode. In order to shorten the collection time a substantial V_{od} has to be applied to the detector.

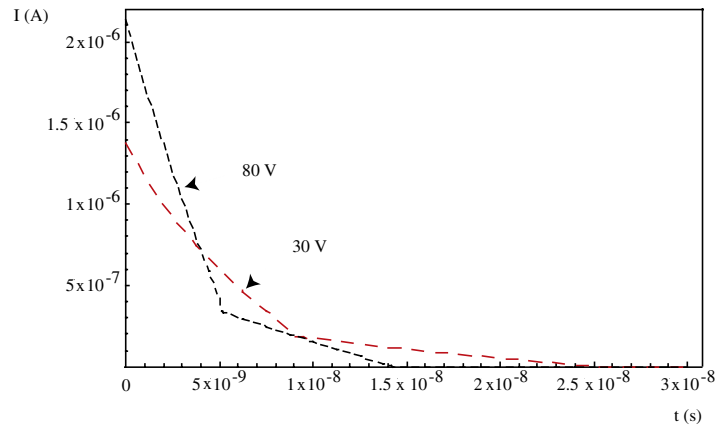


Figure 4.5: Total induced current at $V_{od}=30$ V and $V_{od}=80$ V.

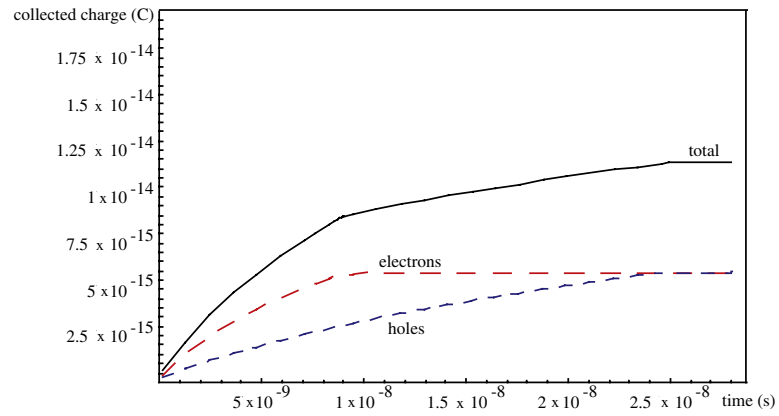


Figure 4.6: Collected Charge as a function of time for $V_{od}=30$ V.

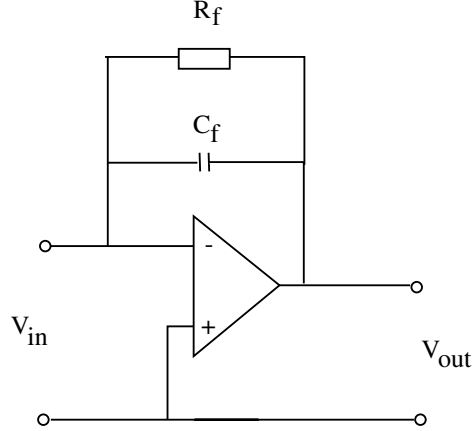


Figure 4.7: Block diagram of a charge sensitive preamplifier with resistive feedback.

4.1.1 Charge Sensitive Preamplifier

The signal produced by a traversing particle in the detector is amplified by a preamplifier mounted close to the detector to minimise noise due to electrostatic pickup or cable capacitance.

In a **charge sensitive amplifier** the charge from the detector is integrated on a feedback capacitor C_f . The output voltage V_{out} is proportional to the charge at the input of the amplifier. For an ideal amplifier with infinite gain it can be written as:

$$V_{out} = -\frac{1}{C_f} \int_0^t I_{in}(t) dt = -\frac{Q(t)}{C_f} \quad (4.6)$$

V_{out} remains at a constant value for times greater than t so that the output voltage of a signal following the first one will start at the level of the first one and thus have a higher absolute amplitude. In order to avoid this effect a feedback resistor R_f is put in parallel to C_f to discharge C_f after each integration. V_{out} then decreases exponentially with a time constant $\tau_p = R_f C_f$. Figure 4.7 shows the block diagram of a charge sensitive preamplifier with a feedback capacitor and resistor.

Pile-up can occur due to a high pulse frequency where the capacitor is not yet completely discharged when another signal arrives at the input. As the deposited charge is proportional to the voltage step of the output the differentiation of V_{out} gives a short bipolar pulse with the height proportional to the voltage step at the output of the preamplifier. This differentiator transmits high frequency noise which decreases the signal to noise ratio

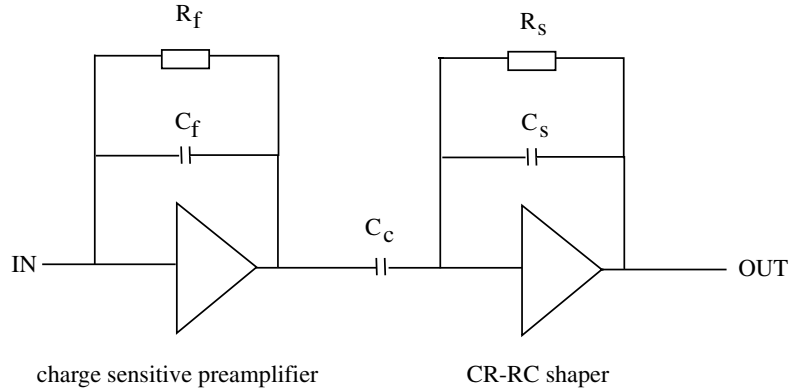


Figure 4.8: Schematic of a charge sensitive preamplifier and a CR-RC shaper

S/N. Therefore an integrator is placed after the differentiator. This stage after the preamplifier is referred to as shaper. It reshapes the signal from the preamplifier and acts as a bandpass filter. The time constant τ_s of the shaper has to be significantly higher than the charge collection time to avoid charge losses due to ballistic deficit, see 4.1, and low enough to be sensitive to the experimental parameters, such as the bunch-crossing frequency in collider experiments. Figure 4.8 shows a block diagram of a charge sensitive amplifier and a CR-RC shaper.

CR-RC shaping is only one possibility of shaping. There exist various other shapers, such as double differentiation or semi-Gaussian shaping. Which method is chosen depends on the experimental requirements, such as S/N ratio or pile-up acceptance. The shaping time plays a crucial role in the noise performance of the system which will be discussed in the following paragraphs.

The noise performance of a system is characterised by the equivalent noise charge (ENC) which is defined as a signal which would generate an output signal of the same amplitude as the rms noise in the system. The noise performance is determined by the noise parameters of the preamplifier input device and the shaping function of the circuit. As a simplification the noise of an amplifier system can be expressed as an ideal noiseless amplifier and a series voltage noise source and a parallel current noise source [53, 54, 55, 56, 57].

The main **series noise** contributions are:

- Noise in the *input channel* of the preamplifier. In an input FET it is due to current fluctuations, while in a bipolar transistor the channel series noise is caused by Johnson noise in the base spreading resistance and collector shot noise. The series channel ENC for an input FET and a bipolar transistor assuming CR-RC shaping can be written as

$$\text{ENC}_{cs}^{FET} = \frac{e}{q} \sqrt{\frac{4kT2\Gamma}{3g_m\tau_s}} (C_i + C_d) \quad (4.7)$$

$$\text{ENC}_{cs}^{bipolar} = \frac{e}{q} \sqrt{\frac{4kT \left(R_{bb} + \frac{1}{2g_m} \right)}{\tau_s}} (C_i + C_d)$$

q is the unit charge, $e=2.718$, k is the Boltzmann constant, T the absolute temperature, Γ is the excess noise factor, g_m is the transconductance, C_i is the input capacitance of the amplifier which can be neglected in the case of the bipolar transistor, C_d is the detector capacitance, τ_s is the peaking time of the shaper and R_{bb} is the base spreading resistance.

For the bipolar transistor the transconductance $g_m=qI_c/kT$ where I_c is the collector current. For a FET $g_m \cong 3I_{ds}/V_p$, where I_{ds} is the drain-source current and V_p is the pinch-off voltage.

The series channel noise represents the minimum white noise in the system. It can be displayed as a constant term plus a term depending linearly on the detector capacitance.

- *Flicker noise* (1/f - noise) is an excess noise with an 1/f-spectrum. The Flicker noise is independent of the shaping time and directly proportional to the detector capacitance. Possible sources for Flicker noise are resistance fluctuations in a resistor proportional to the dc current flowing through it.

Flicker noise has also been observed on highly irradiated FOXFET biased detectors, where the oxide contains many positive charges and influences the functionality of the FOXFET structure.

- Noise from *series resistors* on the detector or from resistors between detector and amplifier. This can for instance be the resistance of the aluminium layer on top of the readout strip of a silicon detector. For an aluminium layer of width w , thickness d , length L and a resistivity ρ the equivalent noise charge can be expressed as [58]:

$$\text{ENC}_{rs} = \frac{e}{q} \sqrt{\frac{4kTR_s}{\tau_s}} (C_i + C_d) \quad (4.8)$$

where $R_s=\rho L/wd$.

The main **parallel noise** sources are:

- Noise due to the *detector leakage current* across the pn-junction. The leakage current produces shot noise, which is a statistical fluctuation in the current. The shot noise increases with the square root of the shaping time τ_s .

$$\text{ENC}_{lp} = \frac{e}{q} \sqrt{\frac{qI_l\tau_s}{4}} \quad (4.9)$$

$q=1.602 \times 10^{-19} \text{C}$ and I_l is the detector leakage current.

- Noise due to the *feedback resistor* R_f . In most cases in a charge sensitive preamplifier the feedback resistor can be made sufficiently high so that noise contributions from R_f can be neglected.

$$\text{ENC}_{fp} = \frac{e}{q} \sqrt{\frac{kT\tau_s}{2R_f}} \quad (4.10)$$

- Noise due to the *bias resistor of the detector* R_d .

$$\text{ENC}_{dp} = \frac{e}{q} \sqrt{\frac{kT\tau_s}{2R_d}} \quad (4.11)$$

- For a bipolar transistor the *base current* contributes to the parallel noise in the same way as the detector current. $\beta=I_c/I_b$ is the current gain factor where I_c and I_b are the collector current and the base current, respectively.

$$\text{ENC}_{icp}^{bipolar} = \frac{e}{q} \sqrt{\frac{qI_c\tau_s}{\beta}} \quad (4.12)$$

The total noise of the system is defined as the square-root of all parallel and series noise sources added in quadrature.

$$\text{ENC}_{total} = \sqrt{\sum_i \text{ENC}_i^2} \quad (4.13)$$

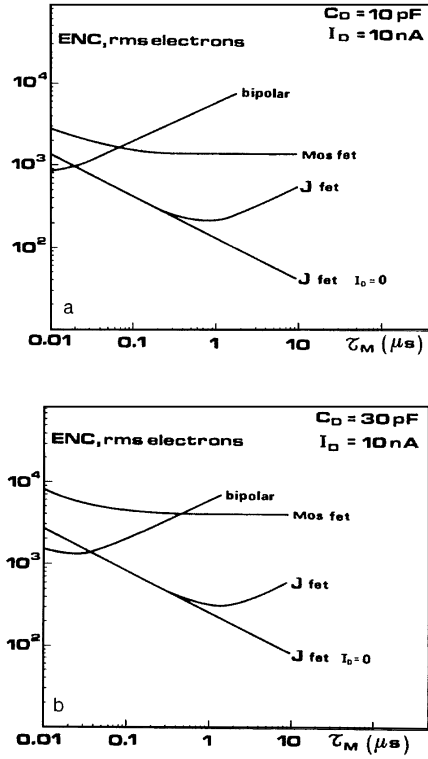


Figure 4.9: ENC for a bipolar transistor a JFET and a MOSFET as a function of shaping time for two different detector capacitances (10 pF and 30 pF). Recent developments [59] have shown that CMOS frontend chips with a much lower noise can be produced. For the VIKING chip with 2 μs shaping time the ENC for a load capacitance of 10 pF and 10 nA leakage current would be 400-500 e^- .

Whether a bipolar or field effect transistor is chosen for the preamplifier depends largely on the experimental conditions. Shown in figure 4.9 is the equivalent noise charge from three different devices as a function of shaping time (from [54]). In one case a detector capacitance of 30 pF is assumed and in the other case C_d is set to 10 pF. The detector leakage current is set to 10 nA. The figure illustrates that at very short shaping times the bipolar transistor gives a lower ENC compared to a MOSFET or JFETs. This time regime is exactly the range foreseen for LHC. In order to avoid pile-ups determined by occupancy shaping times of 25 ns are necessary.

Generally, the noise has to be sufficiently low to distinguish the signal of a particle passing through the detector from the noise. A measure for this is the signal to noise ratio (S/N) where the S/N peak from the particle has

to be well separated from the pedestal peak.

Radiation damage of readout electronics is not considered in this thesis. However, it is a severe problem in the planned ATLAS detector as it leads to a general performance degradation. More information on radiation damage in frontend electronics can be found in [60].

4.1.2 Ballistic Deficit

Ballistic deficit is the loss of output signal amplitude due to charge collection times in the detector being larger than the shaper rise time of the readout electronics. In the ideal case the signal output should be independent of the charge collection time in the detector, or the input current should be a delta-like pulse. As shown in section 4.1 the charge collection time in a depleted silicon detector depends on the amount of over depletion of the detector. For $V_{od}=30$ V figure 4.4 shows a maximum collection time of approximately 25 ns. This is in the order of the shaping times needed in LHC experiments and the current pulse can no longer be regarded as a delta-like pulse.

For a given pulse shaping network where all the charges are collected instantaneously, the output pulse is given as $V_0(t)$ with peaking time t_0 . For a finite collection time the input pulse $U(t)$ will reach its maximum at a time T and thus the output pulse $V_T(t)$ will peak at t_m . The maximum amplitude is reduced to $V_T(t_m)$ by the ballistic deficit BD [61]. The ballistic deficit can be defined as

$$BD = \Delta V = V_0(t_0) - V_T(t_m) \quad (4.14)$$

The relative ballistic deficit (RBD) can then be expressed as:

$$RBD = \frac{\Delta V}{V_0(t_0)} \quad (4.15)$$

As shown in figure 4.10 the ballistic deficit is coupled with a shift in the peaking time of the output pulse.

The output signal is a convolution integral representing the superposition of the impulse responses over time and can be written as

$$V_T(t) = \int_0^t I(z)V_0(t-z)dz \quad (4.16)$$

The output signal for a semi-Gaussian shaper ($CR-RC^n$) for instantaneous charge collection can be determined using the Laplace transform of the differential equation characterising the pulse shaping network [61]:

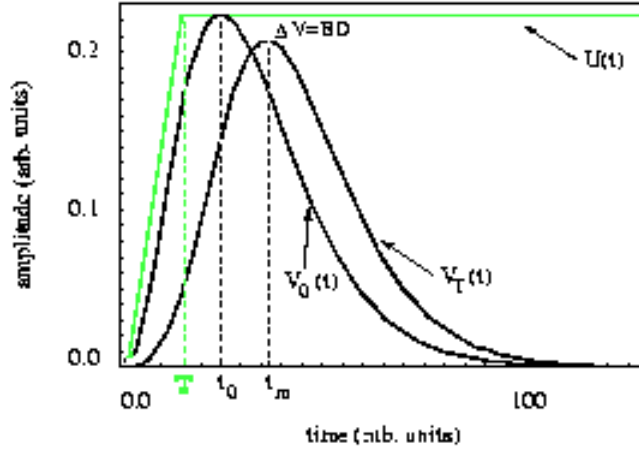


Figure 4.10: Illustration of the ballistic deficit for an input pulse with rise time T and a semi-Gaussian shaper of order $n=3$. See text for definition of symbols.

$$V_0(t) = \frac{1}{n!} \left(\frac{t}{\tau} \right)^n \exp\left(-\frac{t}{\tau} \right) \quad (4.17)$$

where $t_0 = n\tau$.

A constant source function $U(t)$ of duration T is assumed for finite charge collection.

$$U(t) = \frac{1}{T} [t - (t - T)H(t - T)] \quad (4.18)$$

where $H(t-T)$ is a step function, which is equal to zero for $t < T$ and equal to one for $t \geq T$.

The resulting output signal can then according to equation 4.16 be written as:

$$V_T(t) = \frac{t}{\tau} \left(1 - \exp(-t/\tau) \left(1 + \sum_{m=1}^n \frac{t^m}{m! \tau^m} \right) - \left(1 - \exp((T-t)/\tau) - \exp((T-t)/\tau) \sum_{m=1}^n \frac{(t-T)^m}{m! \tau^m} \right) H(t-T) \right) \quad (4.19)$$

The output pulse peaks now at the time t_m , which is larger than t_0 .

$$t_m = \frac{T}{1 - \exp(-T/(n\tau))} \quad (4.20)$$

This exact solution is based on the Laplace transform of the differential equation characterising the pulse shaping network. It has to be noted that the input signals from a real detector may not lead to a preamplifier output in the form of $U(t)$. $U(t)$ as described here assumes a rectangular current pulse, which is especially not the case for low over depletion. However, a first approximation of the ballistic deficit and the general change of the shaper output can be derived with it. In section 4.5 a pulse scan of a strip detector connected to the SCT32A chip at different bias voltages is presented.

4.1.3 Spatial Resolution and Noise

The position resolution of a silicon strip detector depends on different factors. They can roughly be divided in physical processes in the detector and external parameters. The physical processes contain the statistical fluctuations of the energy loss and the diffusion of carriers during the drift in the electric field. External parameters are the strip pitch and the electronic noise [15].

Most of the electron-hole pairs produced by a traversing minimum ionising particle are produced within a narrow channel of about $1 \mu\text{m}$ width [62]. As discussed in section 4.1 the fluctuation of the energy loss leads to the release of high energetic electrons, the δ -electrons. Although their probability is small they can have a quite large range and may lead to a shift of the centre of gravity of the produced charge carriers.

The produced charge carriers drift in the electric field to the electrodes of the detector. During the drift electrons and holes diffuse by multiple collisions. The charge distribution can be described as a superposition of many Gaussian distributions. The *diffusion* leads to the fact that the produced charge can be shared between several strips. In reality the charge distribution of a MIP in a $300 \mu\text{m}$ thick detector has a FWHM (full width at half maximum) in the order of 5-10 μm . With readout pitches larger than the diffusion width, most tracks are only registered on one strip.

For a detector with a strip pitch larger than the diffusion width, the position information of a track is given by one strip responding to the hit. The resolution is then given by a rectangular or binary distribution.

$$\sigma = \frac{P}{\sqrt{12}} \quad (4.21)$$

where p is the strip pitch of the detector.

If the charge is shared between adjacent strips the position of a hit can be determined with higher accuracy by finding the centroid of the charge. Charge division can not only occur by diffusion (where sufficiently small pitches are required) but also by tracks passing the detector under small angles and by capacitive or resistive charge coupling.

For charge coupling [63] the strip pitch is reduced by introducing intermediate strips which are not read out by the electronics. Resistive charge division requires a high resistor being implemented between adjacent strips which represents a parallel noise source. Capacitive charge division does not require an additional process step and uses the the intrinsic interstrip capacitance between the strip implants. Charge induced in the intermediate strips is registered by capacitive coupling on the readout strips. The interstrip capacitance has to be much bigger than the strip-to-backplane capacitance to avoid charge losses to the backplane. To avoid distortions of the electric field all strips have to be at the same potential. This is achieved by integrated bias resistors in the case of ac-coupled strips.

To calculate the centroid of the charge, several algorithms can be used. All of them rely on the correlation between signal on the readout strip and track position. In the following the centre of gravity method and the eta algorithm are discussed.

When the charge is deposited on two strips the *centre of gravity* yields:

$$x = x_L + \frac{S_R}{S_L + S_R}p = x_L + \eta p \quad (4.22)$$

with x_L as the position of the left strip in the cluster, $S_{L,R}$ are the signals on the left and the right strip in the cluster respectively, and p is the strip pitch. It is assumed that $S_{L,R}$ are the two largest pulse heights in the cluster.

The resolution is then given by the standard deviation of the difference of the predicted position (by a telescope system) and measured position (centre of gravity method).

The COG (centre of gravity) method does not take into account the influence of the strip capacitance to the backplane and between non-neighbouring strips and only applies to clusters produced by the passage of a single particle [64]. It also assumes that the signal on the readout strip depends linearly on the track-position between the strips. It has been shown that close to the implant the reconstructed position is independent of the hit position, while in between the strips it strongly depends on the exact hit position. This means that the COG method does not necessarily lead to the optimum resolution.

A method which takes into account the full aspect of charge sharing is the *eta-algorithm* [65]. The average impact point x_0 for a given η is then given by:

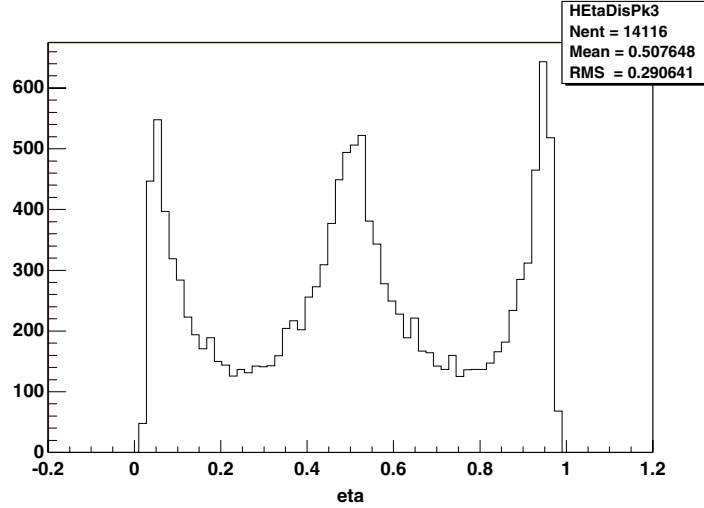


Figure 4.11: η -distribution for a $50 \mu\text{m}$ pitch detector with one intermediate strip.

$$x_0 = x_L + \frac{\Delta}{N_0} \int_0^\eta \frac{dN}{d\eta} d\eta = x_L + F(\eta)\Delta \quad (4.23)$$

The total number of events N_0 is used to determine the correlation between η and x . Comparing it to the COG method the expression η has been replaced by a function $F(\eta)$. The only assumption necessary for the reliability of this algorithm is a uniform distribution of particle tracks in one strip pitch interval.

An example for an η -distribution is plotted in figure 4.11. The detector used here has a pitch of $50 \mu\text{m}$ with one intermediate strip. By integrating $dN/d\eta$ one can obtain $F(\eta)$ and thus the position of the hit. Resolutions of $1\text{-}2 \mu\text{m}$ were obtained with this type of detector using readout electronics with $2 \mu\text{s}$ shaping time [59]. For big strip pitches, e.g. $80 \mu\text{m}$ as used for the ATLAS detectors, the obtained resolution is more close to the digital resolution for straight tracks.

The position resolution now not only depends on the strip pitch as in the binary case, but also on the S/N ratio. The electronic noise determines the minimum signal which can be measured on a strip and therefore small signal contributions could get lost if the noise is too high. The position resolution can be approximated by:

$$\sigma = K \frac{N}{S} p \quad (4.24)$$

The empirical constant K depends on the geometry of the detector [62].

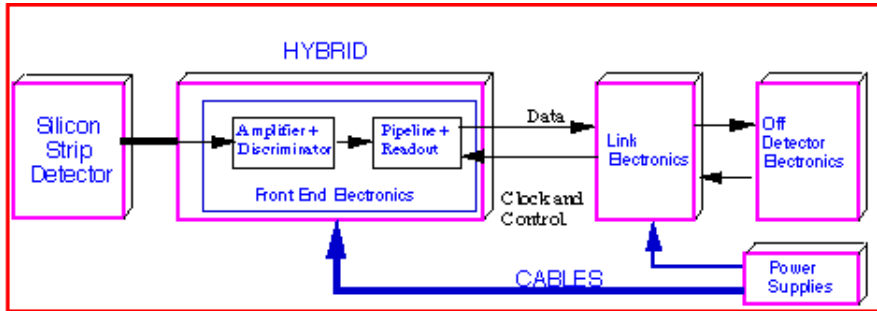


Figure 4.12: Schematic view of the ATLAS SCT readout system [66].

4.2 Readout Systems

The baseline ATLAS module will consist of 4 silicon strip detectors, 2 pairs mounted back to back and hybrids with readout electronics mounted on both sides of the module. A total of more than 6 million channels have to be read out in the silicon strip part of the ATLAS SCT.

The readout system for the ATLAS SCT consists of frontend electronics mounted close to the detectors, data links transmitting the data from the module and supplying clock and control signals, power supplies for the detectors and chips, and an off detector readout and control system. A schematic view of the ATLAS readout system as proposed in the TDR using binary frontend chips is shown in figure 4.12.

The frontend chips have to fulfil several requirements to guarantee the optimum performance throughout the experiments lifetime:

- **Low noise** with high detector capacitances (~ 20 pF/channel).
- **Fast pulse shaping** (25 ns peaking time) to be sensitive to the high event rate of the LHC.
- **Radiation hardness** to ensure good performance in the high fluence environment.
- **Low power consumption** per channel as more than 6 million channels are used for the silicon strip detector readout.

Given in table 4.1 are the specifications for the SCT readout electronics defined in the ATLAS TDR [8]. The specifications assume two ATLAS prototype detectors of 64×63.6 cm² total area connected to 6 chips on one hybrid. The total load capacitance of each channel is approximately 20 pF.

Parameter	Specification
Noise	<1500 ENC
Efficiency	99%
Bunch Crossing Tag Resolution	1 bunch crossing
Pipeline Length	128 locations
Temperature Range	-15 °C to 30 °C
Power Dissipation	<3.8 mW/channel
Radiation Total Dose	2×10^{14} n/cm ² (10 Mrad)

Table 4.1: Specifications of the ATLAS SCT readout electronics

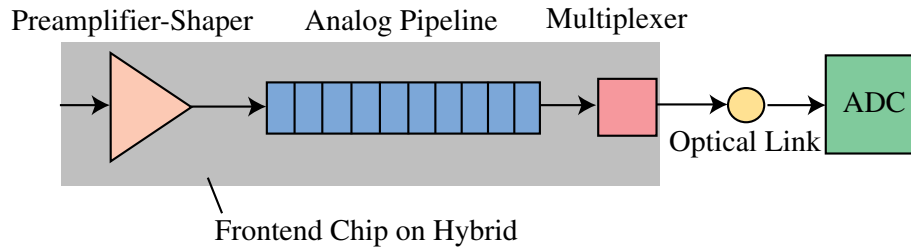


Figure 4.13: Schematic analog readout architecture for one channel.

4.3 Analog and Binary Readout Systems

Several readout systems have been proposed for the ATLAS silicon tracker. One general question is whether the pulse height information, and thus an analog system, is needed or not. In the following a short overview of the advantages and disadvantages of analog and binary readout systems is given [67].

4.3.1 Analog Readout

An analog frontend chip designed for ATLAS consists of a preamplifier-shaper circuit followed by an analog pipeline and a multiplexer to read out the individual channels. The data are transferred via an optical link to the off detector system. In an analog system the pulse height information of every channel is preserved and can be analysed. A signal from the detector is first amplified and then shaped to provide the proper peaking time. The analog signal is then sampled into a storage pipeline. When a positive trigger signal arrives the stored value is read out for each channel via a multiplexer, see figure 4.13. This requires a fast analog multiplexer running at 40 MHz and an analog optical link of sufficient bandwidth.

The data are then sparsified in the counting room by processor farms. A

hit is usually defined when the signal on a strip exceeds a certain threshold defined in units of the system noise. In most cases this threshold is set to 4σ . The strip with the highest signal is referred to as the seed strip. The neighbouring strips are then investigated to find out if they contain part of the signal. The neighbouring threshold is commonly set to 2σ . If their signal exceeds this threshold they are included in the hit cluster. The signals of all channels in a cluster are then added and divided by the single channel noise. This quantity is referred to as the cluster signal to noise ratio (S/N). Another cut which is higher than the individual cuts is applied to the cluster S/N.

An analog system is relatively robust to common mode noise, which can be electromagnetic pick-up from power supplies or the connected detector. The common mode noise can be easily subtracted in the software.

Direct access to the pulse height information enables gain or pedestal variations to be corrected in software. Threshold non uniformities can be avoided using a software discriminator.

The resolution of a detector system can be improved by using analog electronics and a centroid finding algorithm (see 4.1.3) to get a better resolution than the binary resolution of strip-pitch/ $\sqrt{12}$. By introducing intermediate strips which are not read out the pitch decreases without increasing the number of electronics channels. As an example detectors with 50 μm readout pitch and one intermediate strip can reach resolutions of 1 μm [68]. However, for ATLAS spatial resolutions of approximately 20 μm [67] are required which can easily be reached with a binary system of 80 μm readout pitch. On the other hand the analog electronic allows bigger readout pitches for the same resolution and thus can reduce the number of total channels. A limitation of the resolution reachable with charge sharing and analog electronics is given by the signal to noise ratio.

The single channel performance in an analog system is continuously monitored during operation. Problems such as high leakage current regions, dead areas, bonding failures, etc. can be detected immediately. The pulse height information from every strip allows the fast diagnosis of such errors during running and add therefore to the safety, reliability and efficiency of the system.

The cluster analysis offers the possibility of excluding large clusters which can be caused by high energetic delta rays or shallow tracks and are generally unwanted events for the track reconstruction. The maximum cluster size can be defined in the software and all other events be rejected.

An analog readout system offers more information on the detector performance and improves the safety of the system. In the foreseen ten years of LHC operation the detectors will have to cope with severe radiation damage leading to performance degradation on top of the already strict constraints of low noise, high speed and low power consumption. In chapter 4.5 measurements on irradiated and non-irradiated ATLAS prototype detectors con-

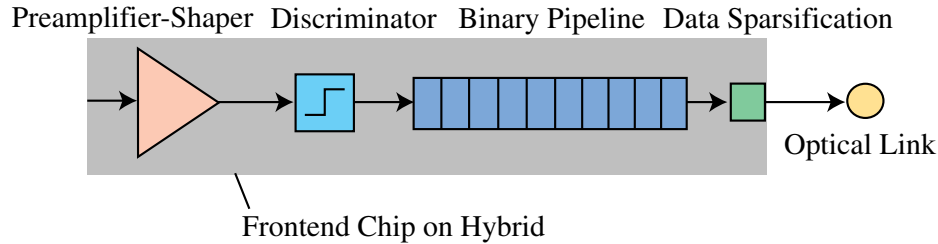


Figure 4.14: Schematic binary readout architecture for one channel.

nected to an analog prototype chip for ATLAS are discussed. The decrease of the S/N for irradiated detectors is one of the main concerns for ATLAS. A highly safe and reliable readout system is therefore very important for the overall detector performance.

4.3.2 Binary Readout

The binary frontend chips use a somewhat similar approach, but do not preserve the information on pulse heights. A preamplifier and shaper, principally of the same architecture as in the analog case, are followed by a discriminator which only provides hit/no-hit information from the strip. Contrary to the analog chip the data is then stored in a digital pipeline until the trigger Level 1 decision is taken. In case of an event the data are written to a readout buffer and transmitted via an optical link to the off-detector system. The readout is in this case referred to as sparse readout as only the data corresponding to hit strips are readout thus reducing the data volume. Data from non-hit strips are ignored.

The monitoring of the system becomes more difficult as no continuous information on every single strip is available. However, it has been shown that the pulse height information and the noise can be obtained from threshold scans of the comparator of the discriminator stage. This is very time consuming and would not be carried out during runs. The longterm stability of the chip is therefore very important.

The binary readout requires a very high quality preamplifier and shaper with negligible gain and pedestal spread. Mismatches cannot be corrected in the analysis software. Threshold non-uniformities will effectively add to the noise.

A good signal to noise ratio is required as otherwise a high rate of noise hits will force an increase in threshold and therefore cut on the efficiency. This is a non-negligible problem in the high radiation environment which leads to degradation of the signal to noise ratio.

Common mode noise cannot be subtracted and will decrease the system performance without any chance to cure the problem in software.

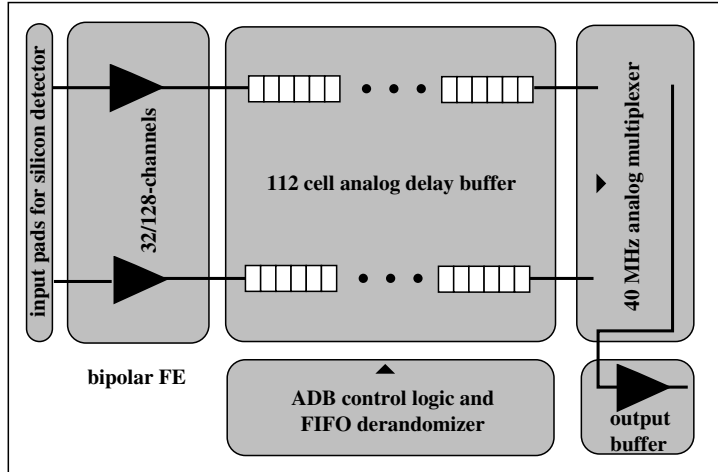


Figure 4.15: Blockdiagram of the SCT-A chip.

4.4 The SCT32A Analog Frontend Chip

A prototype analog frontend chip in a 32 and 128 channel version has been developed for the ATLAS silicon tracker readout [55]. The SCT-A was produced in radhard BiCMOS DMILL technology to sustain the radiation environment in LHC.

The BiCMOS technology [69] combines bipolar and CMOS transistors in one single integrated circuit which allows VLSI (Very Large Scale Integration) circuits with high speed and low power dissipation to be achieved. A further advantage of the BiCMOS technology is that no change in the series noise due to radiation has been reported so far. The increase of noise is basically due to the radiation induced leakage current increase of the detector.

4.4.1 SCT-A Layout and Functionality

The overall chip size of the 32 channel version is $4.6 \times 6.8 \text{ mm}^2$ and for the 128 channel version $7.9 \times 8 \text{ mm}^2$. The SCT-A chip consists of a bipolar preamplifier-shaper circuit, followed by a 112 cell deep analog delay buffer (ADB), the so called pipeline for each input channel. At the output side a readout amplifier and a 40 MHz analog multiplexer (MUX) is placed. A ADB control logic and a FIFO derandomizer are integrated on the chip. Figure 4.15 shows the blockdiagram of the SCT-A chip.

The frontend stage consists of a transresistance amplifier with a bipolar input transistor, a single gain stage and a integrator with 25ns peaking time

followed by an output buffer. The preamplifier consists of a single ended npn feedback pair circuit. The feedback resistor has a value of $80\text{ k}\Omega$ and the feedback capacitor a value of 50 fF .

The analog signal from the frontend is sampled at 40 MHz into the ADB. The ADB is an analog memory CMOS circuit which stores analog signals during the trigger 1 latency. The storage capacitor that samples the voltage has a value of 310 fF . In order to recover the full pulse shape from the frontend stage it is only necessary to retrieve the sample of the peak value. The pipeline is controlled by two registers (write,trigger) and one buffer clocked at 40 MHz . A write pointer controls the writing of data into unused memory columns while the trigger pointer sets flags for trigger level 1 acceptance signals. The buffer is used to hold these flags to memory columns to protect them from being overwritten. As soon as the trigger level 1 acceptance signal arrives the binary address of the memory column with the corresponding analog values is stored in the derandomizing FIFO. The delay between the write pointer and the trigger pointer can be tuned between 2 and $2.5\text{ }\mu\text{s}$. As the readout time is usually longer than the loop pointer time, the pointers skip over columns that are protected with flags. This simultaneous read and write operations enable detector readout without dead time.

The analog values from flagged memory columns in the ADB are read out via the multiplexer part of the chip. It contains 32 (128 for the SCT128A) channels with sample-hold circuits followed by an output buffer. The multiplexer of the 128 channel version works at 40 MHz , while the SCT32A is only equipped with a 10 MHz multiplexer.

Figure 4.16 shows a picture taken from an SCT32A chip mounted on a PCB. The input of the chip is on the right-hand side of the picture with a total of 36 pads. The SCT32A has 32 input channels with a complete readout chain and four input pads which are connected only to the preamplifier shaper part of the chip. The pad pitch on the detector side is $50\mu\text{m}$. Two channels have no preamplifier attached and cannot be contacted via an input pad though they are visible in the multiplexer output.

The PCB is supplied with external voltages of: $+7\text{ V}$ and -7 V as voltage supplies for the output drivers on the PCB; -2 V and $+5\text{ V}$ for ECL signals; $+4\text{ V}$ to power the chip.

For the SCT32A and the first version of the SCT128A the bias settings of the chip have to be adjusted via potentiometers on the PCB. The nominal settings for the SCT32A chip are given in table 4.2. However, the collector current setting depends largely on the connected load capacitance [70]. The value for the collector current I_{pre} given in table 4.2 is best used for load capacitances of 10 pF and above. For load capacitances of about 2 pF per channel, preamplifier currents of around $70\text{ }\mu\text{A}$ were used.

I_{pre} is the current in the input transistor of the preamplifier (collector current), I_{shaper} is the shaper current, I_{buffer} is the bias current of the buffer,

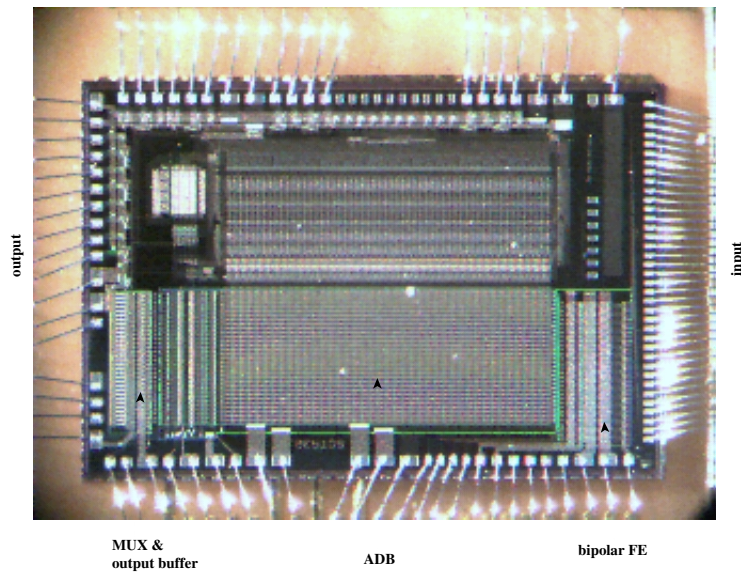


Figure 4.16: Picture of an SCT32A chip mounted on a PCB.

	Nominal Settings
I_{pre}	$220 \mu\text{A}$
I_{shaper}	$40 \mu\text{A}$
I_{buffer}	$10 \mu\text{A}$
V_{ri}	2 V
V_{ro}	2 V
I_{biad}	$30 \mu\text{A}$
I_{biar}	$25 \mu\text{A}$
I_{sfb}	$30 \mu\text{A}$
I_{ecl}	$100 \mu\text{A}$

Table 4.2: Nominal bias settings for the SCT32A.

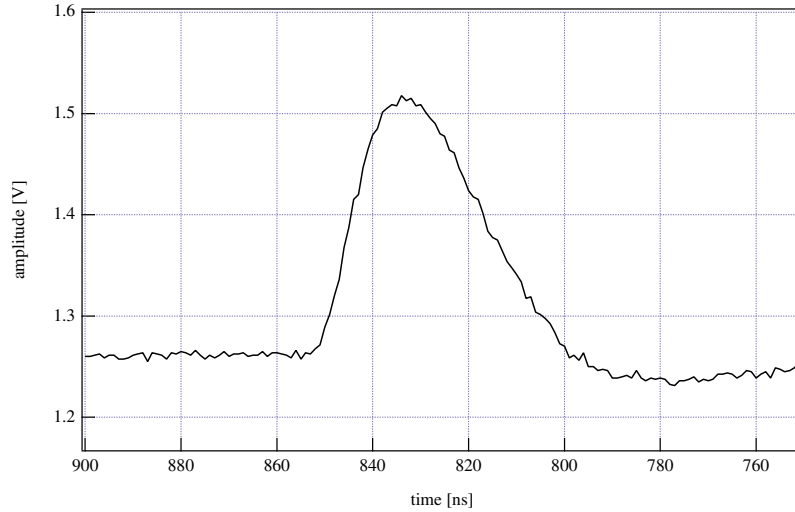


Figure 4.17: Broken channel output of the SCT32A for a 3.6 fC input pulse.

V_{ri} is the reference potential of the memory capacitor, V_{ro} is the baseline of the readout amplifier, I_{biad} and I_{biar} are the bias currents of the readout amplifier, I_{sfb} is the bias current of the MUX output buffer and I_{ecl} is the bias current of the ECL to CMOS converters.

The SCT32A includes a test-capacitor input of 100 fF. The response to an injected signal via this test-capacitor can be detected directly after the preamplifier shaper part of the chip on the so called broken channel output.

To test the full chain of the chip, including pipeline and multiplexer, the test-pulse can be injected in every fourth channel of the chip. Four connectors on the PCB allow the response of the whole chip to be scanned, as the first connector injects the pulse to channel 1, 5, 9, etc., the second one injects the pulse on channels 2, 6, 10, etc.

Figure 4.17 shows the broken channel output of a SCT32A chip for an input voltage step of 3.6 fC provided by a pulse generator. The output pulse has a peaking time of 25 ns. The pulse shape was obtained by varying the time of the injected pulse with respect to the readout time so that a different time slice of the shaper output is measured for each time-step.

The output is not exactly a true semi-Gaussian. The falling edge of the pulse decreases faster than expected for a semi-Gaussian shaper. This is caused by two feedback resistors in series used in the integrator stage.

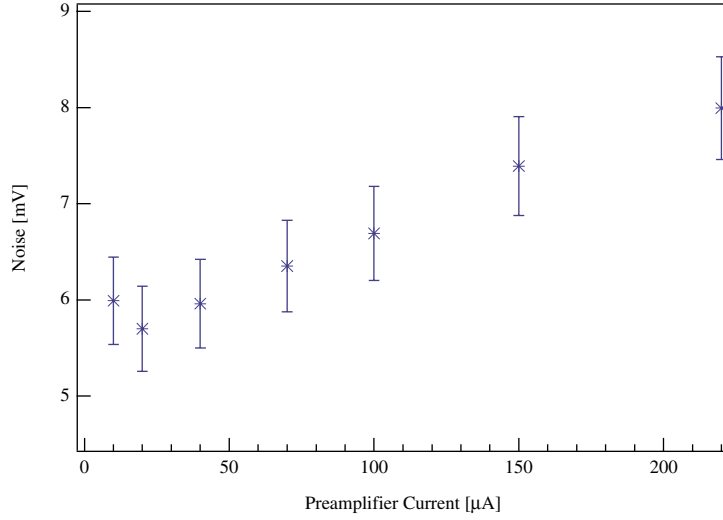


Figure 4.18: Mean noise of all 30 channels of the SCT32A chip 28. The errors displayed are the standard deviations of the mean values.

4.4.2 Noise Performance

The noise performance of the SCT32A chip is given by the channel noise of the bipolar input transistor and the parallel base current noise. According to equations 4.7 and 4.12 the equivalent noise charge can be written as

$$\text{ENC}_{bipolar} = \sqrt{\frac{4kT \left(R_{bb} + \frac{1}{2g_m} \right)}{\tau_s} (C_i + C_d)^2 + \frac{2qI_c \tau_s}{2\beta}} \quad (4.25)$$

The parallel noise of the feedback resistor can be neglected for high load capacitances. For 220 μA collector current the base spread resistance R_{bb} has a value of 60 to 80 Ω .

The measured mean noise of all channels without load capacitances including the ADB and the multiplexer as a function of collector current, is displayed in figure 4.18. A 3.6 fC input pulse (equivalent to one MIP) was applied to the test capacitor. It can be seen that the noise increases with increasing collector current. The noise is displayed in mV and not converted to ENC due to uncertainties in the test capacitor as discussed in the following chapter.

Noise measurements performed on the frontend have been carried out leading to a noise figure of $\text{ENC}=620 \text{ e}^- + 33 \text{ e}^-/\text{pF}$. For measurements including the full chain of the chip a somewhat higher noise is expected

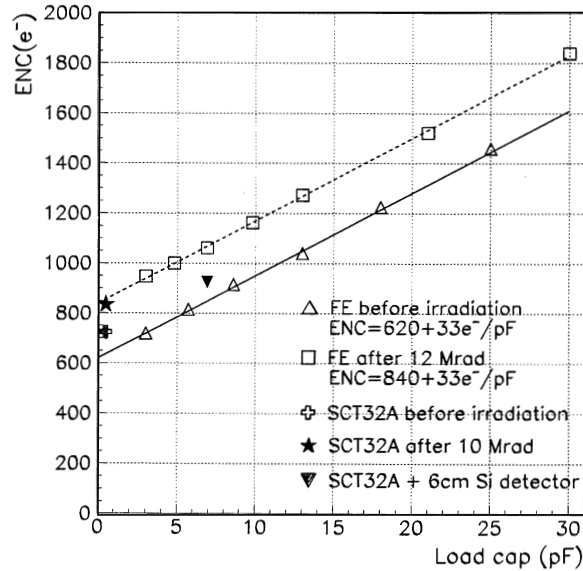


Figure 4.19: Noise measurements of the SCT32A preamplifier-shaper circuit and on the full chip [55].

due to contributions from cell to cell variations in the pipeline or pick-up of digital noise. Measurements on the full chip gave an equivalent noise charge of $720 e^-$ as displayed in figure 4.19.

4.4.3 Source- and Pulse-Setup for the SCT32A in the Laboratory

Measurements to check the functionality of the chip were carried out by injecting pulses from a pulse generator into the test capacitor input. The measurements were controlled by a PC using *Labview*. A schematic of the apparatus is displayed in figure 4.20. The output of the chip is connected to a digital oscilloscope. The data are sampled in the ADC of the scope and read out via a GPIB-bus from the PC. To provide the 40 MHz clock and the control signals for the chip (reset, write, etc.) a sequencer designed by M. Morrissey [71] was used. This VME unit is essentially a programmable multi-channel pulse generator. As shown in figure 4.17 the peak of the shaper output is rather sharp. In order to readout the full signal, i.e. at the peak of the pulse, the trigger must be precisely timed with respect to the 40 MHz clock. In the case of running at LHC the exact trigger is provided

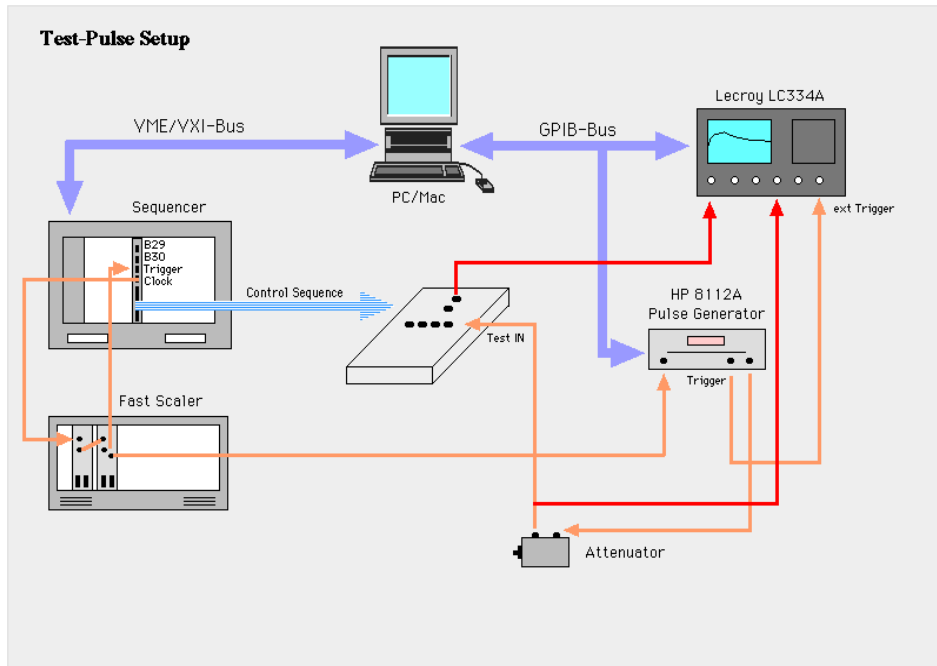


Figure 4.20: Setup to measure the response of the SCT32A to a calibration pulse.

by the bunch crossing clock. The trigger signal is built from the 40 MHz clock by scaling down the clock using a fast NIM scaler. The resulting NIM signal is then brought to the trigger input of the sequencer and to the trigger input of the pulse generator. The pulse generator provides a voltage step which is fed into the test input of the chip and a trigger signal for the scope. The time of the injected pulse can be varied at the pulse generator with respect to the readout time. By varying the delay the pulse shape of the shaper output can be scanned even from the multiplexer output as every delay time corresponds to a different slice of the pulse being read out. The observed signal height of a channel at the multiplexer therefore follows the pulse shape of the shaper.

With the pulse-setup it is possible to check the pulse form of the preamplifier part, the functionality of all channels, the linearity of the chip and the signal to noise performance. The response of the chip can be regarded as linear at least up to an input pulse of 4 MIP (14.4 fC) as can be seen in figure 4.21. The output pulse of the broken channel was measured for different input pulses up to 4 MIP for two different chips. For both input pulse polarities both chips show almost identical behaviour.

The noise of a bare chip is determined by injecting a known signal into the test-capacitor input. The test capacitor has a nominal value of 100

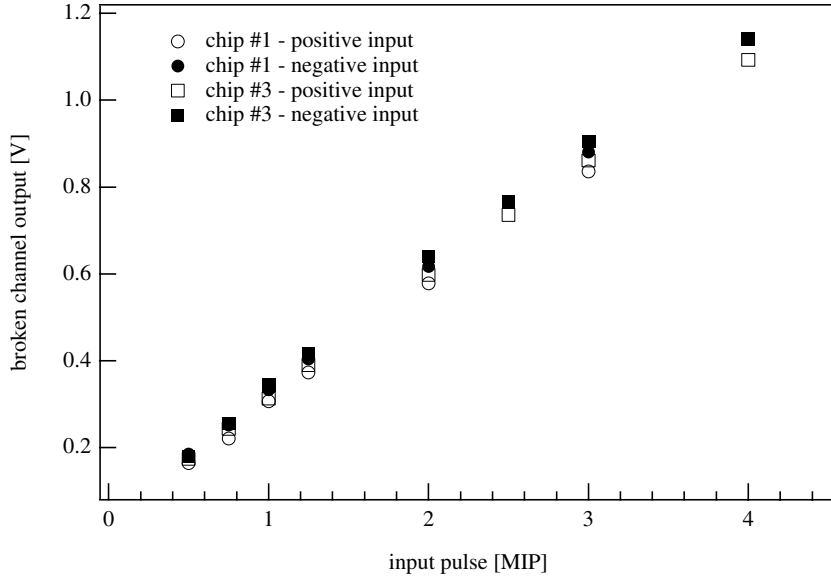


Figure 4.21: Broken channel output of two SCT32A chips as a function of positive and negative input pulses.

fF. Due to this small value parasitic capacitances can considerably change the effective capacitance on which the input signal is collected. Effective changes of up to 20-30% are possible. As a consequence of a higher effective capacitor value, a higher output signal will be detected and thus leading to a lower ENC.

A source setup was used to measure the signal from minimum ionising particles passing through a detector. As for the pulse-setup the sequencer is used to provide the clock and the control signals, the data are acquired with the oscilloscope ADC and a PC controlled the measurements. The trigger is synchronised using a coincidence between the so called B29 output of the sequencer and the signals from a photo multiplier. The B29 is the same signal as the 40 MHz clock, but it is only active during the readout cycle of the chip. After passing through a discriminator the B29 signal is brought into the coincidence. A photo multiplier is placed underneath the detector which registers the β from a Ru^{106} -source. The photo multiplier signal is passed through a discriminator and then fed into the trigger input of the pulse generator. The pulse generator fulfils two functions. It creates an 8 ns wide output pulse, which is about the peak width of the shaper output, to ensure that only the peak value of the signal is identified. The second function is that the pulse generator allows the photo multiplier signal to be shifted with respect to the readout time and thus determine the optimum timing. Figure 4.22 shows the schematic setup for source tests.

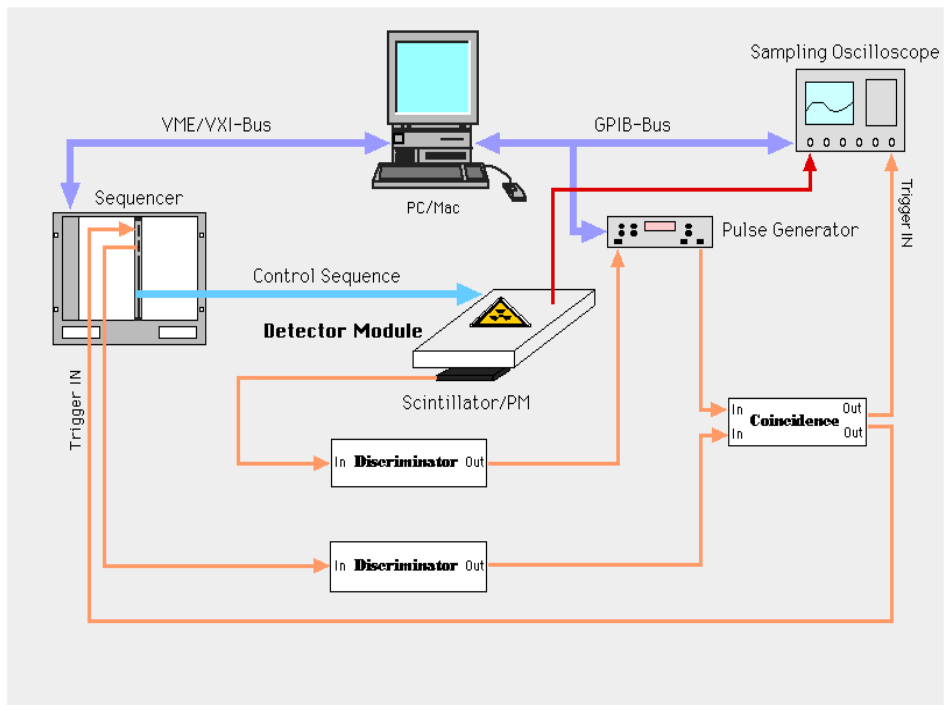


Figure 4.22: Source-setup for the SCT32A.

Thickness	300 μm
Size	$64 \times 63.6 \text{ mm}^2$
Strip Length	61.04 mm
No. Readout Strips	768
Strip Pitch	80 μm
Multiguard Structure	10 guard rings
Passivation	polyimide (top side only)
V_{fd}	55 V

Table 4.3: Basic properties of the detector p20 from SINTEF.

A program written in C by C. Lacasta is used to analyse the data taken. Usually a 4σ cut is applied to the seed hit and a 2σ cut to the neighbouring hits. A general 6σ limit is used for all clusters and only events with one cluster are accepted. The common mode is corrected in the data and the number of strips in a cluster can be limited. For the presented results the number of strips is limited to three. This is a reasonable choice for detectors with 50 μm and 80 μm pitch with no intermediate strips. As discussed in chapter 4.1.3 mostly single strip events are expected. Clusters with more strips can be allocated to delta-rays emitted perpendicular to the strips. Noisy or defect strips can be excluded from the analysis in the input file. Finally the program produces an HBOOK-file that can be analysed.

4.5 Results from an ATLAS prototype detector using the SCT32A

An ATLAS prototype detector was connected to a SCT32A chip and tested in the source setup in the lab and in a testbeam at CERN. This allowed investigation of a detector and a chip which fulfil the specifications foreseen in the final ATLAS detector. The detector is one of the prototype detectors produced by SINTEF which are described in chapter 3. In table 4.3 the main properties of this detector, referred to as *p20*, are listed.

The chip input pads can only be wire-bonded once. Therefore a 2 mm long glass adapter with parallel aluminium lines is glued between detector and chip to allow a possible reuse of the chip.

To limit the current, a 100 k Ω resistor is put in series with the HI-path of the bias voltage supply. With high detector leakage currents a voltage drop across this resistor will decrease the actual bias voltage. This has to be taken into account and corrected for. A 22 nF capacitor and a 1 k Ω resistor are put to ground after the series resistor to decouple the power supply from the backplane of the detector.

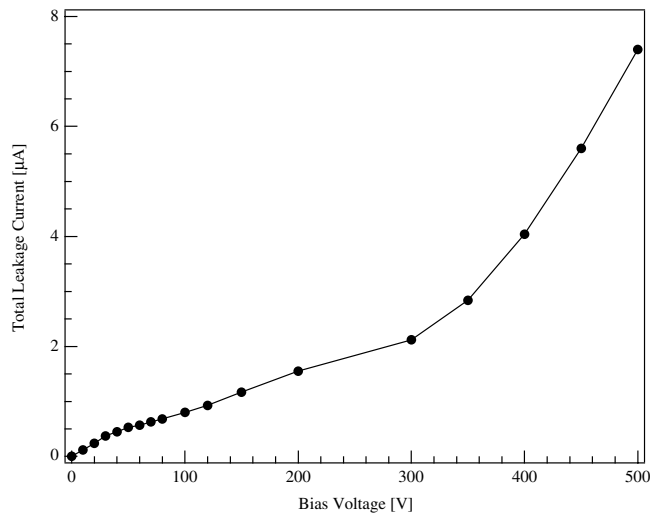


Figure 4.23: Total leakage current of detector p20 mounted to SCT32A.

The total leakage current of the detector mounted on the PCB is shown in figure 4.23. The current has been measured up to 500 V and indicates soft breakdown around 350 V. The voltage drop across the 100 k Ω resistor due to the leakage current is at maximum 0.74 V.

36 strips are bonded via the pitch adapter to the chip of which 30 channels are connected to the full readout chain. All other strips are connected to ground via a kapton line. The contacts for the innermost guard and the biasline are also connected to ground.

The bias settings of the chip used are those listed in table 4.2. The chip was tested by injecting a 3.6 fC signal and showed full functionality for all channels. The noise in this calibration measurement was 759 electrons rms, which is in accordance with the measurements displayed in figure 4.19. However, due to the influence of stray capacitances this value is expected to have an error of about 20-30 %. The mean noise measured across all the channels was 8.0 ± 0.5 mV. The preamplifier current was set to 220 μ A to account for the capacitive load of the detector.

The load capacitance per strip is 1.7 pF to the backplane and 8 pF interstrip capacitance to the next neighbours as determined in static measurements. The maximum error on the measurements is in the order of 1 pF. The interstrip capacitance to the other neighbours has been determined in previous measurements to be in the order of 20% [16] so that the total load capacitance per strip is ≈ 11.3 pF.

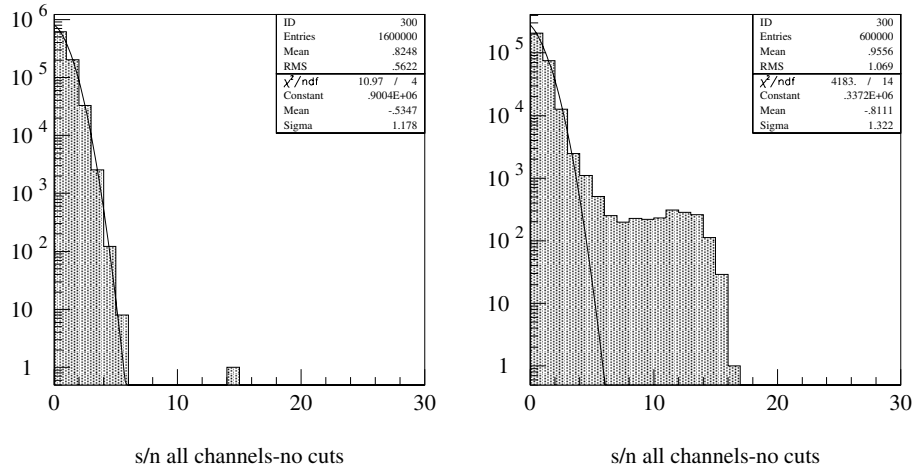


Figure 4.24: Noise runs of two SCT32A.

4.5.1 Source Tests

To check the noise performance of the setup, measurements are taken with a fully equipped board. The source is placed underneath the photomultiplier and a thick steel plate is mounted underneath the detector to shield it from the β -particles. In this way the trigger setup is unchanged, but no particles are registered in the detector. As no particles are registered in the detector and no cuts are applied only the pedestal peak will appear in the S/N histogram. As the noise in a system is the sum of many stochastic processes (shot noise, Johnson noise, etc.) a Gaussian distribution is expected due to the central limit theorem in statistics. Therefore any externally picked up noise will show up in a deviation of the Gaussian form of the pedestal.

The histogram on the left hand side in figure 4.24 shows the result of the noise run of the p20 detector. The detector was biased at 300V and 50 000 events were taken in this measurement. A Gaussian fit was applied to the histogram showing good agreement with the data. The single entry at S/N=14 is negligible compared to 1.6 million total entries. As the detector is not shielded on the side opposite the source it is possible that a cosmic ray has been detected during the almost two hours of run. For comparison the histogram on the right hand side displays the result of a noise run of a different chip with no detector connected. The chip was produced in a different process which caused pick-up noise coupling in from the backplane in about half of the channels. The effect of this non-intrinsic noise in the system is visible as a strong deviation of the pedestals from a Gaussian distribution. This illustrates that the noise runs can be used as a tool to

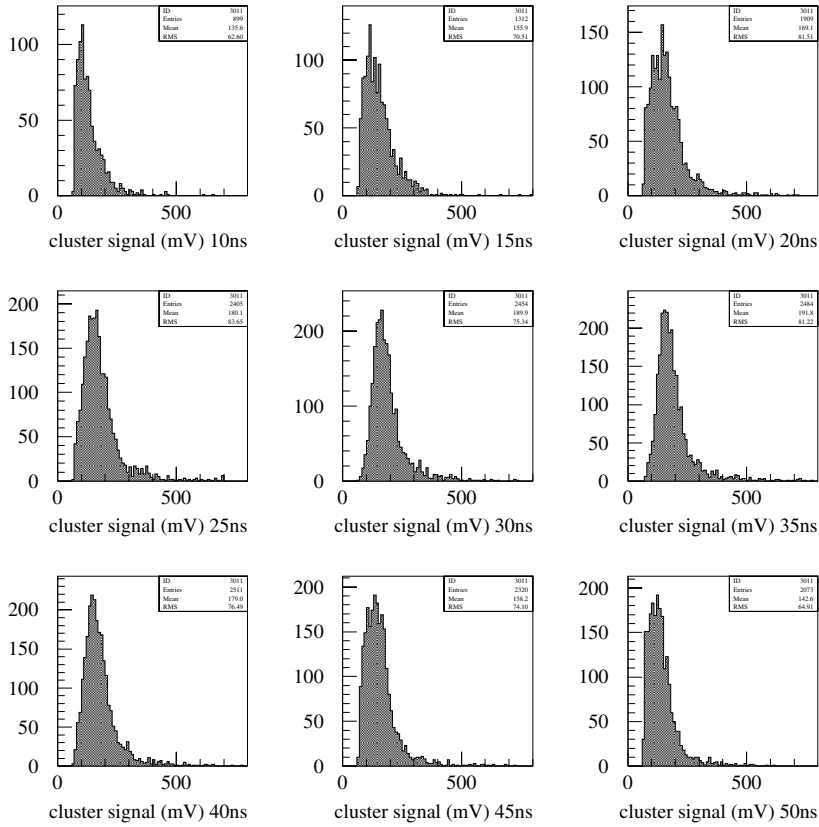


Figure 4.25: Cluster signal of detector p20 at 60 V bias for different trigger delays.

check the immunity of the system to external noise sources.

In order to sample at the peak of the output pulse the delay of the photomultiplier signal with respect to the readout time has to be optimised. Trigger delay scans were carried out at each bias voltage. The delay scans were performed in 5 ns steps. At each delay step 20 000 events were taken in the β -setup and analysed. The cuts applied were those described in 4.4.3.

Figure 4.25 shows the cluster signal histograms at different delay times for 60 V bias. This illustrates that the Landau is distorted even for delays only 15 ns from the optimum delay (which is in this case 35 ns). The Landau distribution seems to ‘move out’ from the pedestals with increasing delay time until it reaches its optimum form and maximum peak value at 35 ns. With further increase of the delay time the peak seems to ‘move back’ into

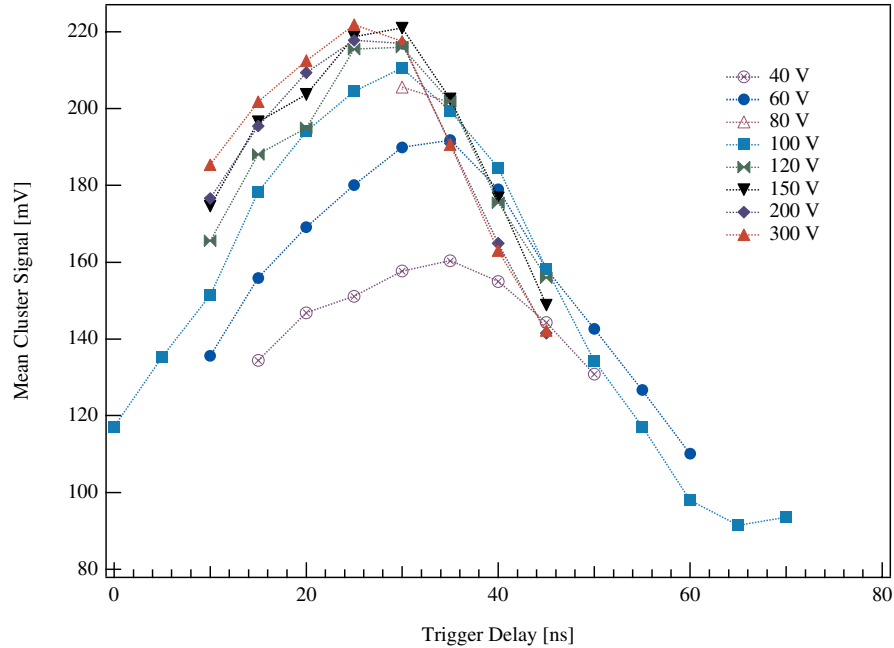


Figure 4.26: Delay scans of detector p20 at different bias voltages.

the pedestals again.

Figure 4.26 shows the mean entries of the cluster signal histograms as a function of delay time for different bias voltages. As the Landau becomes distorted with delay times away from the optimum delay the peak value of the cluster signal distribution cannot be determined. For this reason the mean rather than the peak the mean of all entries are shown as a function of delay time.

The displayed curves are a convolution of the shaper response with the signal from the detector. More measurements at 100 V were taken to illustrate the full pulse shape with the steep slope on the right hand side.

At 40 V bias voltage the detector is not fully depleted. The depletion region has not yet reached the backplane causing e-h pairs which are created in the non-depleted layer to diffuse into the depletion zone. Some of them can recombine before leaving the undepleted zone. The shape of the curve at 40 V is very shallow and broad and no indication of the steep slope of the shaper output is visible. This can possibly be attributed to a very long charge collection time and diffusion in the non-depleted layer.

With increasing bias voltage the pulse shape becomes better defined. The raise of the pulse (right hand side) becomes steeper up to a bias of 200 V. The peaking time at this value can be seen from the plot to be approximately 20-25 ns. Between 60 V and 200 V the pulse shape not only

becomes steeper, but the peak also shifts to lower delay times. This is due to the ballistic deficit as discussed in chapter 4.1.2. With increasing V_{od} the maximum collection time is decreased. As long as the charge collection time is comparable to the peaking time of the shaper the output pulse is smaller than for a delta-like input signal and the peaking time is increased.

Baldinger and Franzen [72] have shown that the relative ballistic deficit can be expressed as

$$\text{RBD} = \frac{\ddot{V}_0(t_0)}{24} V_0(t_0) \quad (4.26)$$

where \ddot{V}_0 is the second derivative with respect to time of the output pulse described in equation 4.17 at $t=t_0$. Thus using equation 4.17, RBD can be written for a semi-Gaussian shaper as

$$\text{RBD} \approx \frac{n}{24} \left(\frac{T}{t_0} \right)^2 \quad (4.27)$$

T is the rise time of the input pulse and n is the order of the semi-Gaussian shaper. The discussion in chapter 4.1.2 presents exact solutions. However, equation 4.27 can be generalised to obtain a quantitative estimate of the RBD without knowing the specific circuit design. This is of special interest as secondary influences on the pulse shape, e.g. from output stage amplification, are not included in the exact solution. The parameter n in equation 4.27 is no longer an integer and accounts for these effects. The parameter n is related to the curvature of the pulse at the peak (represented by \ddot{V}_0) under the assumption of a parabolic shape. A detailed discussion can be found in [72].

As T represents the rise time of the input pulse it can be compared to the maximum charge collection time. On the junction side of the detector the maximum collection time is given by the maximum hole collection time t_{max}^h . By replacing T in equation 4.27 with t_{max}^h from equation 4.4 it is possible to relate the RBD with the collection time and to express the RBD as a function of over depletion.

The mean value of all entries at 300V, which corresponds to 245 V over depletion was used as value for $V_0(t_0)$. The relative ballistic deficit was calculated from equation 4.15. The line referred to as RBD was calculated using equation 4.27 and substituting T with t_{max}^h . The parameters that have to be specified for t_{max}^h are the thickness of 300 μm , the maximum electric field and the drift velocity. The maximum field was calculated for a depletion voltage of 55 V and the drift velocity for holes was obtained at the junction, where $E(x)$ reaches its maximum. The value obtained for E_{max} was 366.7 kV/m and for v_h , 17600 m/s. The prediction of RBD follows the

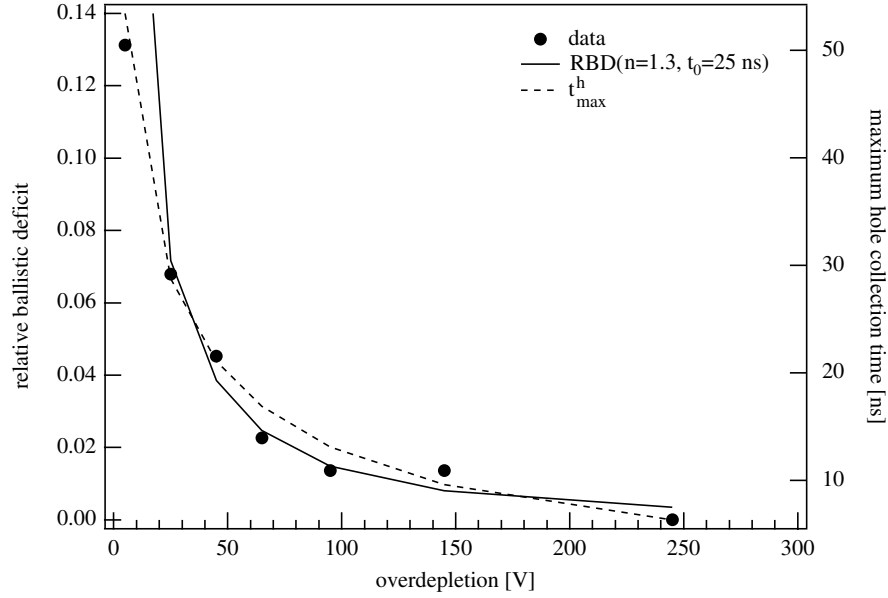


Figure 4.27: Measured RBD, approximation of RBD with T replaced by t_{max}^h and t_{max}^h as a function of V_{od} of p20.

measured data points very smoothly with exception of the first measured data point at $V_{od}=5$ V. In [61] a constant source function of duration T is assumed, which corresponds to a rectangular current pulse. This is not the case for a real detector system (compare figure 4.5). Better agreement between the calculated RBD and the measured point can be expected if the real current form is taken into consideration. Also shown in figure 4.27 is the maximum hole collection time for the previous mentioned parameters as a function of V_{od} . For zero over depletion the collection time goes to infinity which is an artifact of the model described in chapter 4.1. A further assumption which enters into RBD via t_{max}^h is that diffusion is neglected. However, the correlation between RBD and the collection time is clearly shown. For $V_{od}=65$ V the RBD drops below 3%. For a S/N ratio of 17:1 this corresponds to a change of 0.3 in S/N, which is in the order of the measurement error.

The data taken at the different bias voltages have been analysed for optimum trigger delays.

Figure 4.28 displays the S/N ratio and the mean signal per channel at 300 V bias. The signal to noise ratio has been fitted with a convolution of a Landau and a Gaussian distribution.

All measurements taken at the different bias voltages and with optimised trigger delay have been analysed in this way. The peak values of the S/N

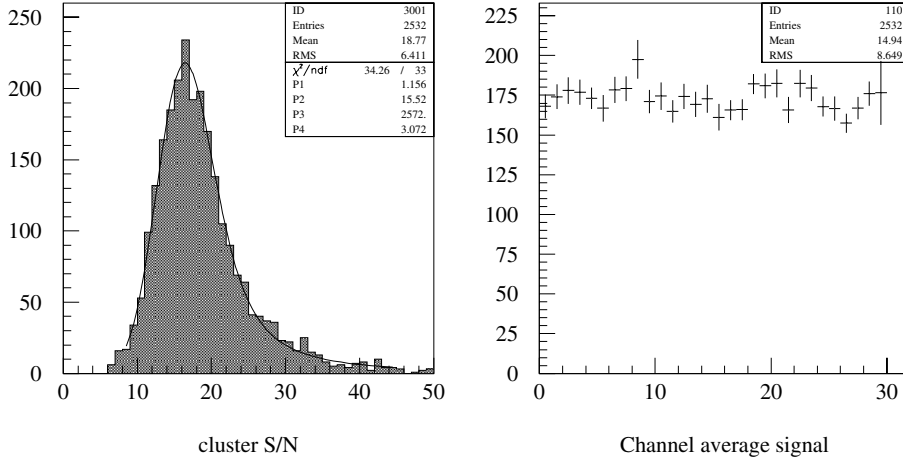


Figure 4.28: S/N and mean channel signal of p20 at 300 V bias.

distributions as a function of bias voltage are displayed in figure 4.29. The errors are in a first approximation assumed for a Gaussian distribution with the peak value being the mean value. The S/N ratio increases with the bias voltage even after full depletion. This can be explained by the ballistic deficit as discussed above. At a bias voltage of around 100 V the S/N ratio reaches quasi-saturation and remains almost constant. The relative ballistic deficit is now less than 3% and leads only to a small increase of S/N up to 300 V bias. This is also visible in figure 4.27, where the RBD drops quickly with increasing V_{od} until it is less than 3% for $V_{od}=65$ V.

At 300 V the S/N ratio reaches a value of $\approx 17:1$. A fit was applied to the data using a function that includes the RBD. The fit function was defined as:

$$a \cdot (1 - \text{RBD})$$

where a is the free parameter. RBD was defined in the same way as in figure 4.27, also using the same fixed parameters for the thickness, the hole velocity and E_{max} . The fit can therefore be expressed as a function of V_{od} . The value for a obtained from the fit is $a=16.9 \pm 0.3$, which corresponds to the S/N ratio. The χ^2 of the fit is 2.8/1.

The ballistic deficit and the resulting increase in S/N ratio beyond depletion is an effect which only occurs at shaping times of the order of the charge collection time. At slower shaping times, e.g. $2 \mu s$ as used in the VIKING chips [59], the RBD can be neglected. In this case the S/N ratio increases with the depletion width and reaches saturation at the full depletion voltage. The electronics that will be used in the LHC experiments has to operate at 25 ns shaping time and thus the ballistic deficit will decrease the performance at low V_{od} .

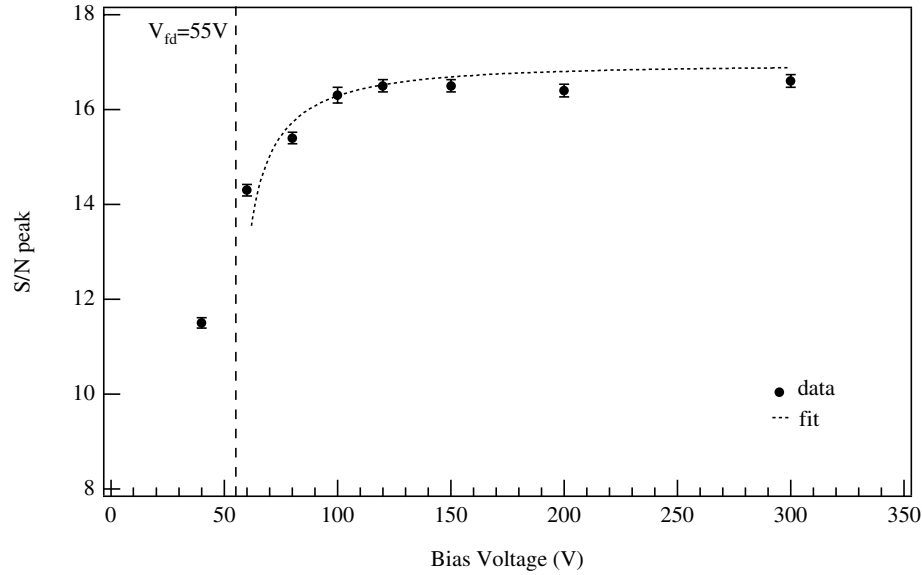


Figure 4.29: S/N as a function of bias voltage of detector p20.

Assuming that a Ru^{106} -source produces approximately 22500 electrons, a S/N ratio of 17:1 corresponds to ≈ 1324 ENC noise. This approximation is not very accurate due to several reasons: the beta source emits a continuous spectrum and thus not only MIP particles; the source cannot be collimated in the same way as a beam; multiple scattering of the β s in the silicon occurs; small angle tracks can cause more strips to fire and decrease the registered signal as some of the signal will be lost in the noise, depending on the applied cuts.

This is illustrated in figure 4.30 where the number of strips per cluster is plotted for 300 V bias voltage. The number of 2-strip clusters is dominating, due to the above mentioned reasons. In a testbeam with a defined particle energy and a beam with small divergence mainly 1-strip clusters and less 2-strip clusters are expected for a $80 \mu\text{m}$ pitch detector with no intermediate strips. A more accurate estimation of the noise of this module is given in the next section, where the testbeam results of this module are presented.

4.5.2 Testbeam Results

The same module as described in chapter 4.5.1, consisting of an ATLAS prototype detector (p20) connected to a SCT32A chip, was measured in a testbeam in May 1998. The settings of the chip were unchanged from the source tests and are listed in table 4.3. The measurements were carried out in the X5 testbeam at CERN. A 100 GeV/c pion beam traversed

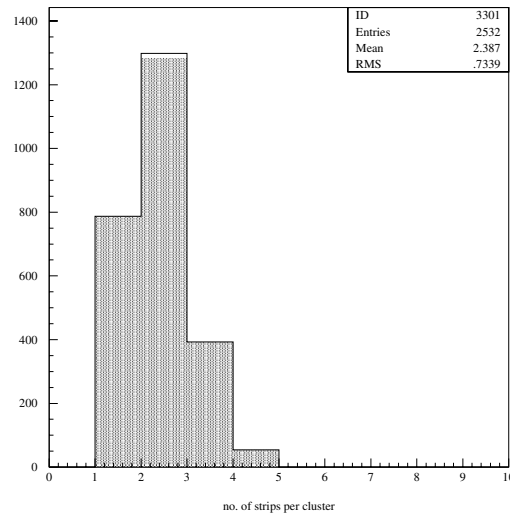


Figure 4.30: Number of strips per cluster of detector p20 at 300 V bias.

the p20 detector perpendicular to the detector plane. To precisely determine the impact point at the detector under test a telescope system from CERN/LEPSI with 4 modules was used [7, 68]. Each module consists of 2 silicon p-in-n detectors mounted perpendicular to each other so that two orthogonal coordinates (x,y) can be measured. Each detector has a total area of $2 \times 2 \text{ cm}^2$ with $50 \mu\text{m}$ readout pitch and one intermediate strip. The detectors are FOXFET biased and the 512 readout strips are connected to 3 VA2 chips [73]. Two modules were placed upstream and two modules downstream of detector p20. A schematic sketch of the arrangement in the testbeam can be seen in figure 4.31. Each module is connected to a VME Scirocco ADC which digitises the signals from the silicon detector. A VME Eurocom CPU controls the DAQ running under OS9 operating system. A small scintillator is mounted in front of the first module plane and after the last module plane to provide a trigger signal. If an event is registered the data from the telescope planes and the detector under test are read into the Scirocco modules. They sample and store the raw data without processing. Finally, the raw data are written to Exabyte tapes to be available for offline analysis. An program developed in ROOT [74] was used to analyse the data after the testbeam.

In the offline analysis the telescope planes have to be aligned in the defined coordinate system (x,y,z) . Tracks are reconstructed by a linear least square fit of the hit positions in the four telescope modules. In this way it is possible to select events where only one track is registered to avoid

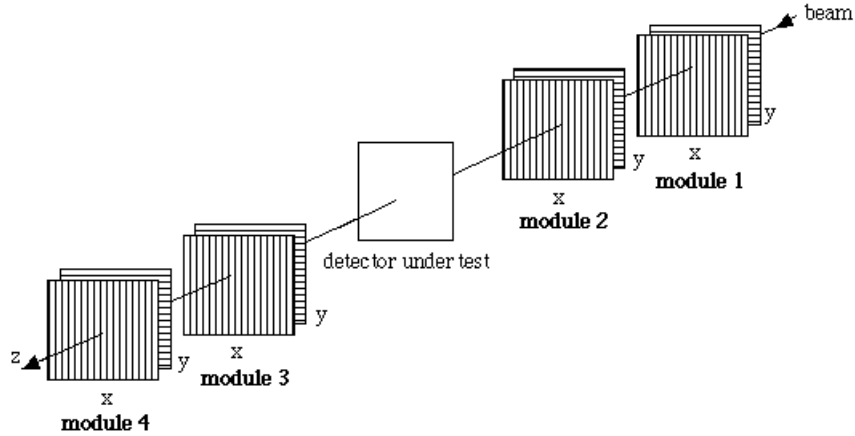


Figure 4.31: Schematic of the telescope system used in the testbeam.

ambiguities. Using a reconstructed track the hit-position in the detector under test can be predicted. Figure 4.32 shows the result for the alignment of one telescope plane. In the right figure the correlation between T_{ud} and T_v is shown. T_{ud} is the difference between the hit position perpendicular to the strips in detector p20 and the track position perpendicular to the strips. T_v is the track position along the strips. If T_{ud} is centred around 0 and a straight line as a function of T_v , the telescope plane is well aligned and the optimum resolution for each plane can be achieved. The resolution determined with the η -algorithm of this plane is shown in figure 4.32. Due to capacitive charge coupling and the low noise at the VA2 chips ($2 \mu\text{s}$ peaking time, $\text{ENC}_{channel} = 135e^- + 12.3e^-/\text{pF}$ [7]) resolutions much better than $25 \mu\text{m}/\sqrt{12}$ can be achieved. The alignment and resolution achieved for plane 3 shown in figure 4.32 is $\sigma = 2.21 \pm 0.07 \mu\text{m}$, which is about ten times better than the binary resolution for $50 \mu\text{m}$ pitch. The resolutions of the other planes vary between 2.12 and $2.4 \mu\text{m}$. Using the telescope planes a passing track can be extrapolated to the detector under test with an accuracy in the order of $1 \mu\text{m}$.

The SINTEF p20 detector was biased at 300 V and data were taken in the testbeam for about two hours. To analyse the data a 6σ cut was applied to the seed hit and a 4σ cut to the neighbouring hit. The seed-cut is 2σ higher than the seed-cut in the source setup as no common cluster cut could be applied in the analysis here and 6σ corresponds to the cluster cut in the source tests. The setup included a TDC so that the time window with the maximum registered charge could be determined. A window of 3 ns width was selected between 149 and 151 ns. The first five channels had to be excluded in the analysis as they were commonly registering hits in almost all events. Also excluded were channels 31 and 32 as they do not have a full

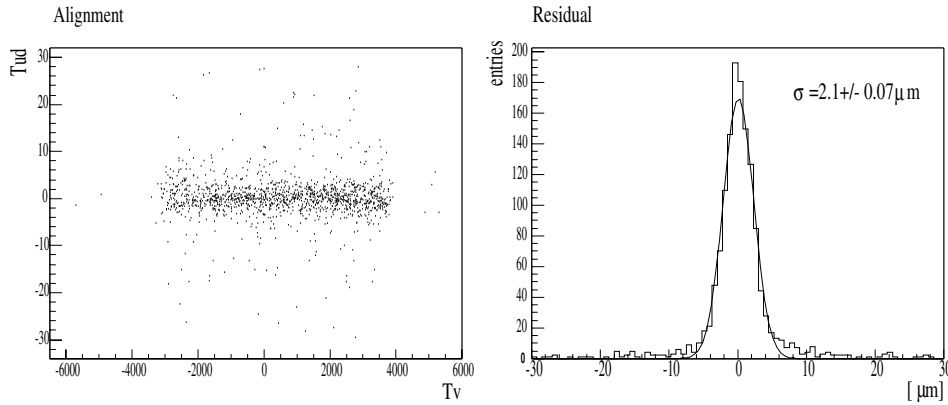


Figure 4.32: Alignment and residual of one telescope plane.

readout chain.

A cut was applied that only allowed a maximum of 3 strips in a cluster. Taking into account the readout pitch of $80 \mu\text{m}$ and no intermediate strip, mainly 1-strip hits are expected in a well collimated beam. Shown in figure 4.33 is the number of strips found in a cluster summed over all registered events. 1-strip hits are dominating, followed by about 15% of two-strip hits.

The cluster signal distribution is shown in figure 4.34. The most probable value of the Landau distribution is 290 ADC counts. A cut was applied at 700 ADC counts to exclude the effects of high energies. The mean noise was computed for all channels and found to be 13.6 ± 3.1 ADC counts. This leads to a S/N ratio of ≈ 21 . 100 GeV pions are not minimum ionising particles anymore and an increase of produced charge pairs in the order of 10% has to be taken into account, so that ≈ 24700 e-h pairs are produced. Assuming that the peak of the Landau corresponds to 24700 e-h pairs, the equivalent noise charge is then 1176 electrons.

Measurements of the noise slope, shown in chapter 4.4.2, have resulted in a noise increase due to load capacitance of 33 electrons per pF. A load capacitance of 11.3 pF leads to $373 e^-$ ENC. The noise slope of the the frontend was determined to be $620e^- + 33^-/\text{pF}$ on a circuit which consisted only of preamplifier and shaper. The total input channel noise is therefore $993 e^-$. The constant value of the input channel noise of $620 e^-$ is most likely an underestimate as it does not contain the noise due to the ADB and the output stage. The noise of a full chip has been measured to be $720 e^-$ in figure 4.19, and the calibration of the chip used in the testbeam has

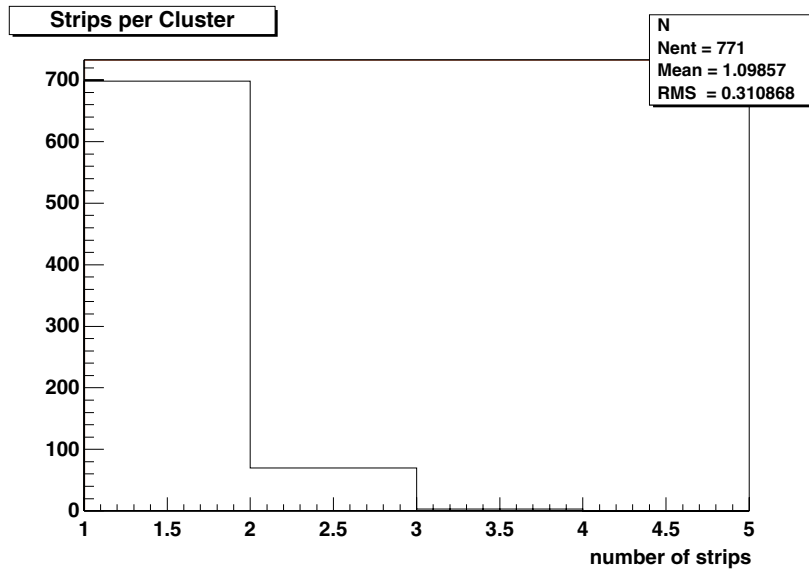


Figure 4.33: Number of strips found in a cluster.

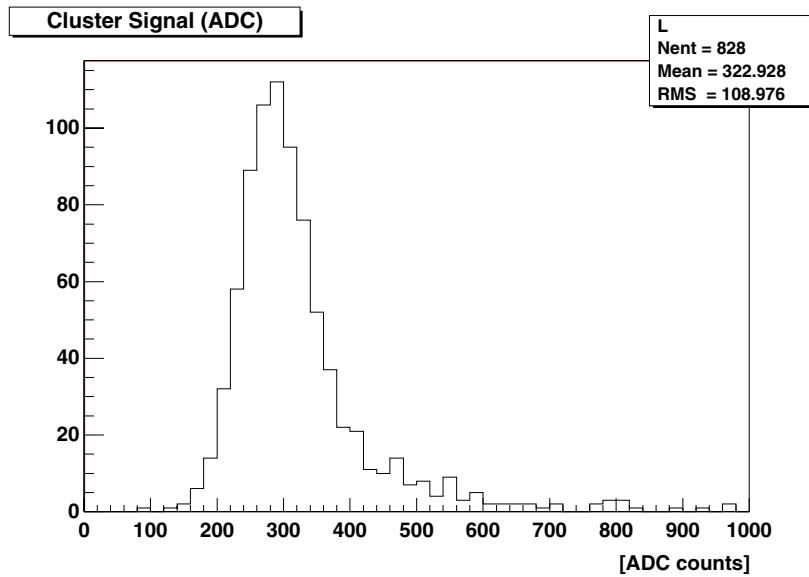


Figure 4.34: Cluster signal distribution of the SINTEF p20 detector.

shown $759 e^-$ ENC. The noise of the full chip is therefore better described by $759 \pm 5\% e^- \pm 33 e^-/\text{pF}$. The 5% uncertainty on the constant term is used to account for variations between different chips. The input channel noise of the module in the testbeam is approximately $1132 e^-$ ENC. The leakage current of the detector stabilised at approximately $7 \mu\text{A}$ after being biased for a few hours and before data were taken. The noise due to the leakage current can be determined using equation 4.9 and is for 9.1 nA , the current of a single strip, $52 e^-$. Further series noise contributions, e.g. from the Al-line, can be neglected, as well as parallel noise contributions from the bias resistor or the feedback resistor. The total noise is therefore according to equation 4.13 $1133 e^-$. The calculated value of the total noise of $1133 e^-$ is in good agreement with the measured value in the testbeam of $1176 e^-$. However, uncertainties that have to be taken into account are that the constant term of the input channel noise varies from chip to chip with at least 5% (as seen from measurement), the calibration itself has an error due to the relatively small test capacitor and due to stray capacitances and that the measurement error of the load capacitance is at maximum 1 pF .

Shown in figure 4.35 is the digital resolution of detector p20 in the testbeam. The plot was obtained by histogramming the difference between the seed strip position and the track position. The distribution is approximately rectangular with edges at around $\pm 40 \mu\text{m}$ as expected for a binary type detector of $80 \mu\text{m}$ pitch. The distribution shown in figure 4.37 was obtained using the eta-algorithm described in chapter 4.1.3 to predict the hit position. The eta distribution for this detector is shown in figure 4.36.

Figure 4.37 was then obtained by histogramming the difference between the calculated hit position and the track position as interpolated from the telescope. A Gaussian fit to the histogram gives a resolution of $23.7 \pm 1.1 \mu\text{m}$. This is in agreement with the binary resolution of $80 \mu\text{m}/\sqrt{12}$. As no intermediate strip is present the resolution cannot be very much improved by charge sharing as for example shown in figure 4.32, where a with $50 \mu\text{m}$ readout pitch and 1 intermediate strip a resolution of $\approx 2 \mu\text{m}$ can be achieved. The eta-distribution in figure 4.36 is already indicating that only very little charge is shared between strips and mostly only one strip is responding to a hit. This is also in agreement with the number of strips found in a cluster, see figure 4.33, where $\approx 85\%$ of the clusters are 1-strip clusters.

In the eta distribution shown in figure 4.36 those signals which are only registered on the ‘left’ strip of two strips are corresponding to an eta of 1, while the signals that are only found on the right strip correspond to an eta of 0. If signals are registered on both strips they correspond to eta values in between the two peaks. Plotted in figure 4.38 is the difference between seed strip position and predicted position for eta values between 0.25 and 0.85 for 2-strip clusters. The plot shows that for a hit between $\approx 30\text{-}50 \mu\text{m}$ from the seed strip a significant part of the signal is registered on the second strip.

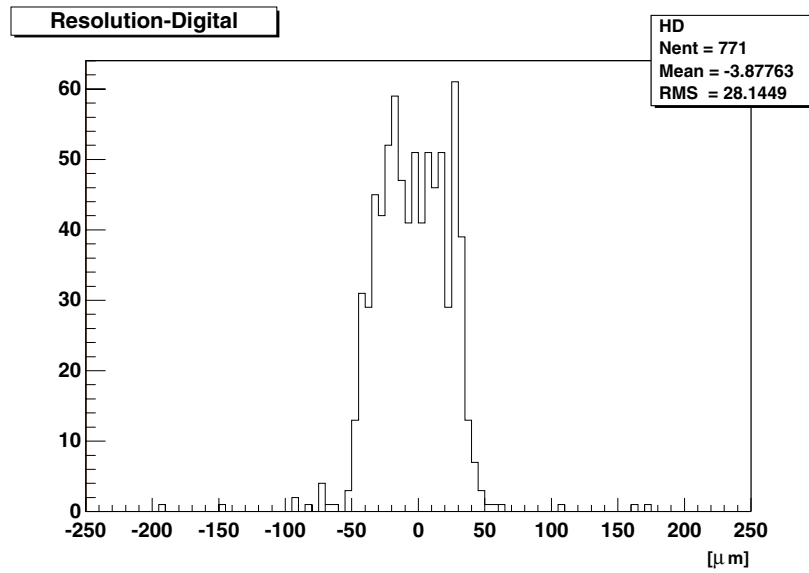


Figure 4.35: Digital resolution of the SINTEF p20 detector.

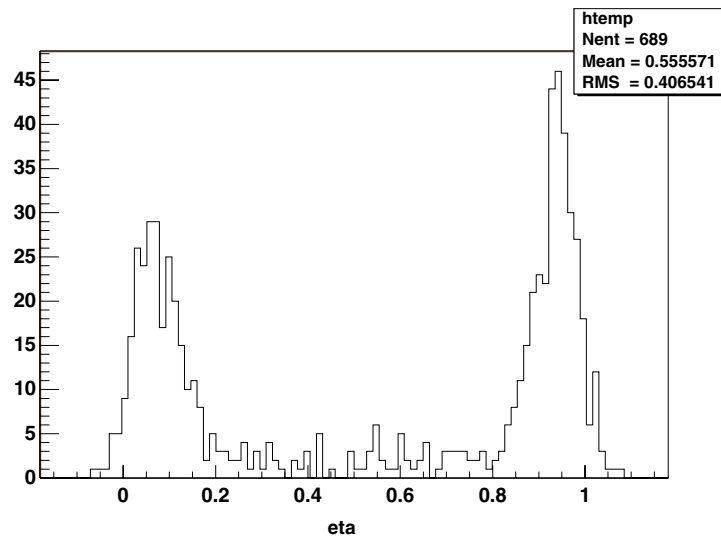


Figure 4.36: Eta distribution of the SINTEF p20 detector.

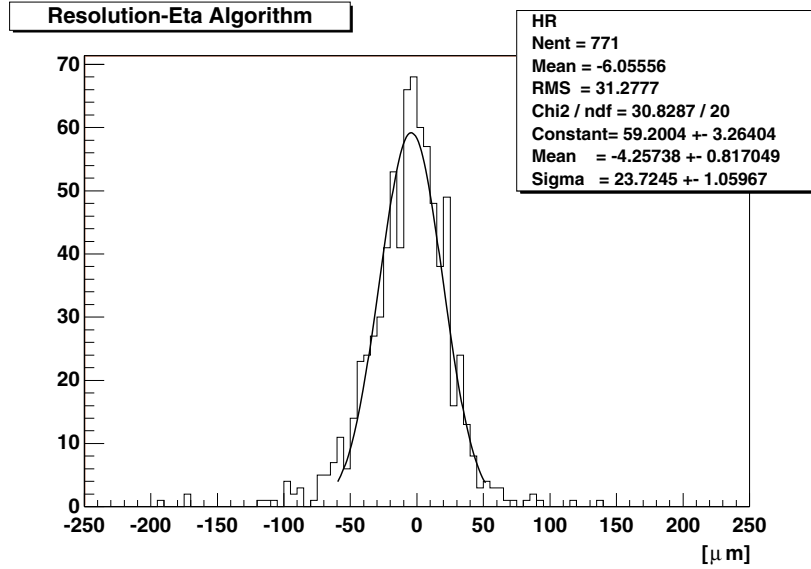


Figure 4.37: Resolution of the SINTEF p20 detector using the eta-algorithm.

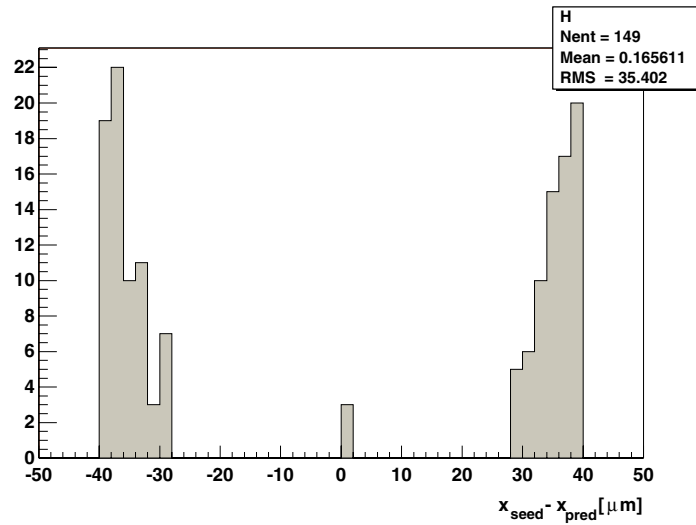


Figure 4.38: Difference between seed strip position and predicted position using the eta algorithm.

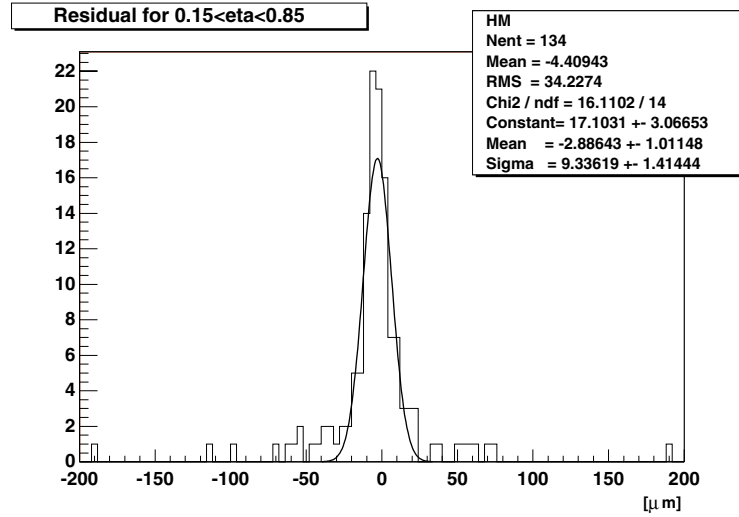


Figure 4.39: Residual of the SINTEF p20 detector for $0.25 < \eta < 0.85$.

This hit distribution is not uniform between $30 \mu\text{m}$ and $50 \mu\text{m}$ but falls off steeply on both sides. This is due to events in the tail of the Landau distribution with substantially higher charge than the Landau peak. All together only $\approx 18\%$ of all events fall into this category and thereby have a better than digital resolution, see figure 4.39.

4.6 Source tests with an irradiated ATLAS prototype detector using the SCT32A

As discussed in chapter 3 the p-in-n detectors produced by SINTEF showed the lowest full depletion voltage of all irradiated detectors. Detector p17 was connected to a hybrid of binary LBIC chips after 18.5 days of annealing and tested in a testbeam at CERN together with 5 other annealed detectors. These detectors took part in the annealing study of which the results are presented in chapter 3. The efficiency as a function of applied bias voltage of all annealed detectors tested in the testbeam are shown in figure 4.40 [75]. As expected all n-in-n detectors show high efficiency down to low bias voltages. This is a result of the detector starting to deplete from the strip side. The p-in-n detectors show a decrease in efficiency around the depletion voltage as the junction has moved to the backside of the detector and in the underdepleted state a non-depleted layer is present underneath the strips. For all detectors a good charge collection efficiency could be achieved at 350 V bias voltage which was then decided to become the op-

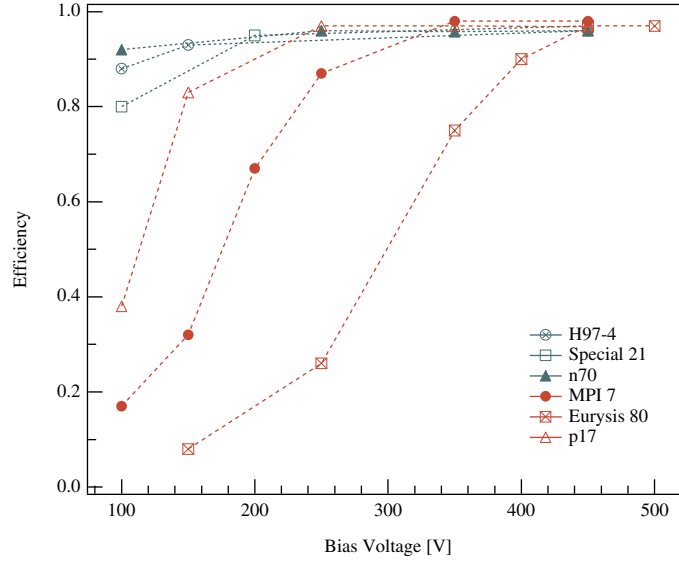


Figure 4.40: Charge collection efficiency at 1 fC threshold of irradiated p-in-n and n-in-n detectors [75]. The detectors have been annealed for 21 days at 21 °C after the irradiation. A description of the detectors can be found in table 3.6

erational voltage for the ATLAS SCT. As can be seen from this plot the detector p17 is fully efficient at 250 V while an efficiency drop is observed on the other two detectors.

Taking the results of this testbeam and the relatively high efficiency of the SINTEF p-in-n detector at low bias voltages, an irradiated ATLAS p-in-n prototype detector produced by SINTEF (referred to as detector *p7*) was connected to an SCT32A chip in the same way as described in section 4.5.1. The chip settings are the same as for the chip connected to detector p20 and are listed in table 4.2. The detectors p7 and p20 have the same layout and were produced in the same production. They even originate from the same ingot. Detector p7 was irradiated together with the other detectors described in chapter 3 in the CERN PS to a fluence of 3×10^{14} p/cm², then stored for approximately 2 months in a freezer at -10 °C. Afterwards the detector was annealed at 25 °C for 9.5 days. The time evolution of V_{fd} during these 9.5 days is shown in figure 3.36. Detector p7 shows a similar V_{fd} as detector p17, which was measured during the annealing study presented in chapter 3, of approximately 150 V at the minimum of the annealing of V_{fd} .

Detector p7 was mounted on the SCT32A board and annealed to 18.34 days at 25 °C, so that it has reached the same amount of anti-annealing as detector p17 before being moved to the testbeam. The β -setup had to be moved into a freezer cooled to -6.4 °C. Due to the high leakage current

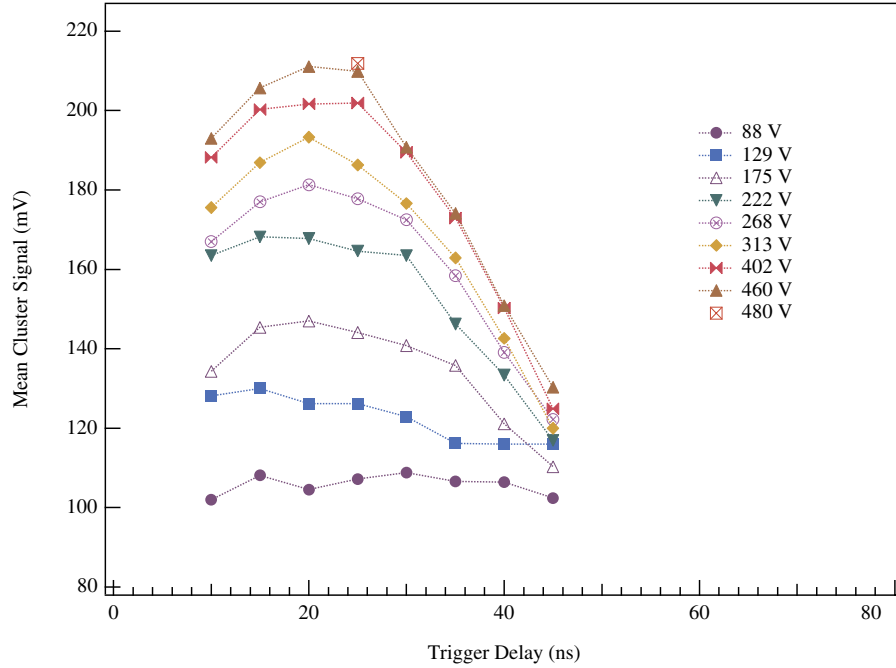


Figure 4.41: Delay scans of detector p7 at different bias voltages.

measurements at room temperature could not be carried out. A noise run was taken to test the system noise and showed a pure Gaussian distribution, compare figure 4.24.

Trigger delay scans were carried out to obtain the optimum delay time as described in the previous section. Shown in figure 4.41 are the mean entries of the cluster signal histograms as a function of delay time for different bias voltages. C-V measurements could not be carried out on the mounted detector. Therefore the V_{fd} has to be estimated from the I-V curve and by comparison to detector p17.

The leakage current of the detector mounted on the board is shown in figure 4.42. A function proportional to \sqrt{V} is fitted to the current values at low voltages. According to equation 2.1 the leakage current increases proportional to the depletion width and thus proportional to the square root of the applied bias until V_{fd} . The data points start to deviate from the fit around 220 V which can be identified with V_{fd} . The exact value of V_{fd} is difficult to obtain with this method as the detector does not represent an ideal junction and the current does not stabilise at a constant value above depletion. However, it can be used as a first approximation of V_{fd} .

From the testbeam results shown in figure 4.40, V_{fd} of detector p17 can be estimated to be between 200 V and 250 V. The detector p17 has been annealed for 2.6 days longer at 25 °C than detector p7. Thus a slightly

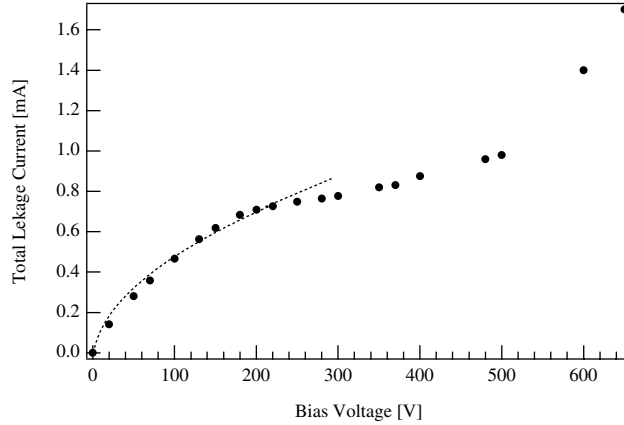


Figure 4.42: Total leakage current of detector p7 mounted to SCT32A.

higher depletion voltage is expected. Using the Ziock parameterisation (see chapter 3) this corresponds to a 4% increase in V_{fd} . This difference is completely negligible compared to the precision of the determination of V_{fd} from the I-V measurement.

V_{fd} is therefore estimated to be between 220 V and 250 V. Large uncertainties have to be taken into account due to the way this value was determined.

Comparing figure 4.41 with the same measurements carried out on the non-irradiated detector p20, see figure 4.26, the behaviour seem to be completely different between irradiated and non-irradiated detector. However, from the information on V_{fd} it is clear that while on the non-irradiated detector all scans, apart from the one a 40 V, were carried out on a fully depleted detector, the irradiated detector was only fully depleted at the measurements above 268 V bias.

From 88 V to 222 V the delay scans of detector p7 appear as curves with no pronounced peak. The detector is not depleted yet. The depletion region is growing from the backside and the region underneath the strips is undepleted. Assuming V_{fd} of 220 V at 88 V the depletion width is only 50 μm wide. It is interesting to note that already at 175 V bias the peak of the Landau distribution of the signal can be fitted although the distribution is not completely separated from the pedestals yet. This voltage corresponds to a depletion width of only 190 μm .

Shown in figure 4.43 are the delay scans of detector p20 at 60 V and of detector p7 at 268 V. At 60 V detector p20 is 5 V over depleted; the best corresponding bias voltage of detector p7 to this value is the measurement at 268 V. The optimum delay has shifted by 5 ns. This is due to different fixed delays using different boards. Both curves appear very similar, but the

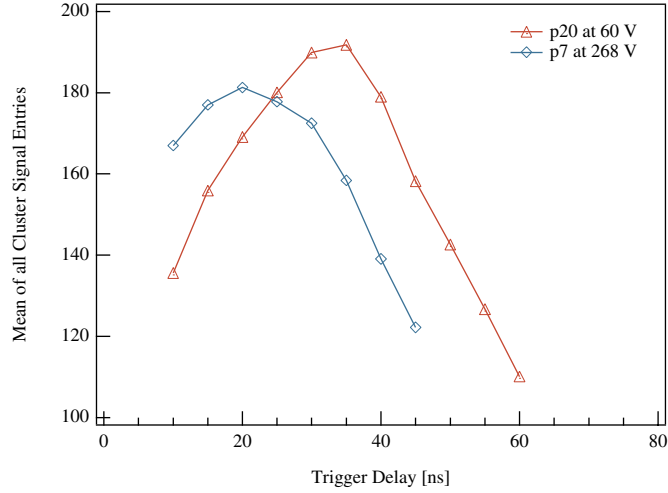


Figure 4.43: Delay scans at 60 V bias for detector p20 and at 268 V bias for detector p7.

detector p7 seems to show a slightly slower increase on the right-hand side. At the maximum the mean entries of all cluster signal of detector p7 is ≈ 12 mV lower than of detector p20.

In comparison, figure 4.44 shows the delay scans at 300 V and 460 V bias. Both detectors are now approximately 240 V over depleted. A difference in height of approximately 10 mV is still visible, but the form of both curves is practically identical with a steep slope of approximately 25 ns peaking time. From this it can be concluded that once the irradiated detector is sufficiently over depleted, no difference in the delay scan is observed in comparison with the non-irradiated detector.

To investigate if the 10 mV difference is a real loss in charge, the peak values of the cluster charge distributions are plotted as a function of bias voltage for detector p20 and p7 in figure 4.45. The errors are assumed for a Gaussian distribution and are of the size of the data points. The broken lines are indicating the full depletion voltages. A difference between detector p20 and the irradiated detector p7 is that in the first case a V_{od} of 40-50 V is sufficient to reach a plateau of the registered signal. For the detector p7 the signal increases slower with V_{od} and does not seem to stabilise at a constant value. At $V_{od}=50$ V the signal is about 25 mV smaller than for the non-irradiated detector which corresponds to a decrease in signal of approximately 14%. However, at 460 V the signal of the irradiated detector reaches an identical value to that signal plateau of the non-irradiated detector. This indicates that part of the charge deficit observed in the irradiated detector is due to charge trapping.

Defects in the lattice introduced by radiation can act as trapping centres

4.6. IRRADIATED ATLAS PROTOTYPE DETECTOR AND SCT32A123

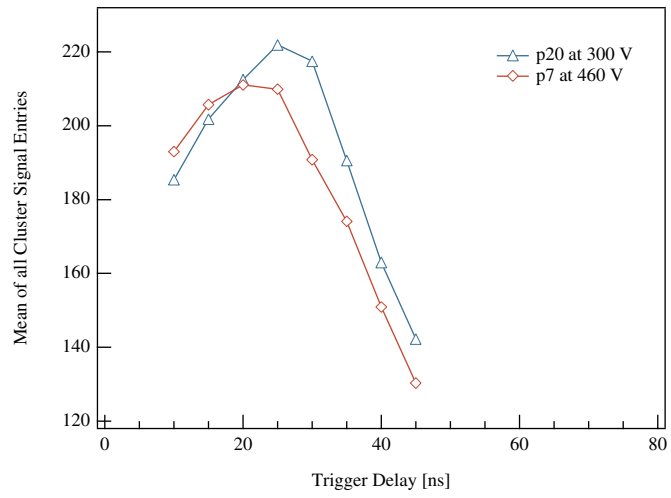


Figure 4.44: Delay scans at 300 V bias for detector p20 and at 460 V bias for detector p7.

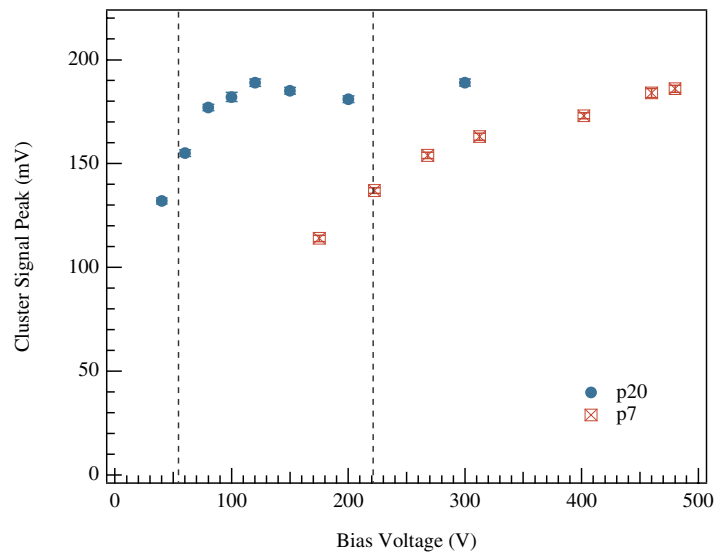


Figure 4.45: Peak value of the cluster signal distribution as a function of bias voltage.

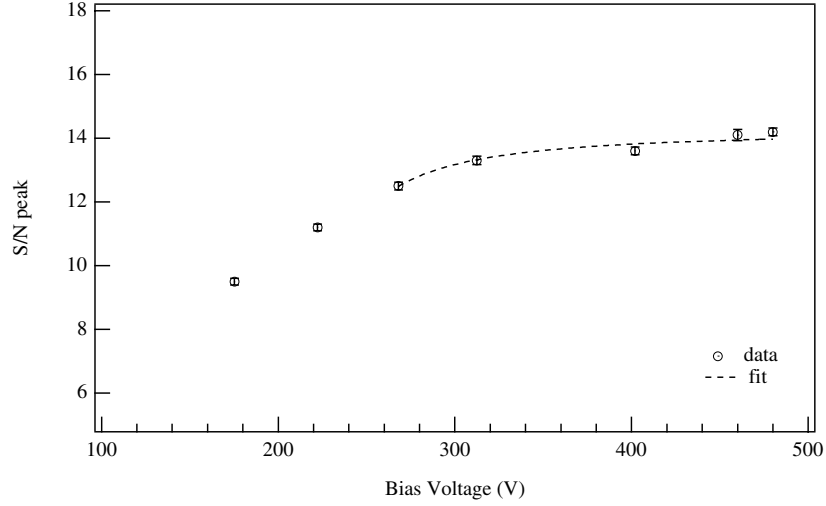


Figure 4.46: S/N as a function of bias voltage of detector p7.

for the produced charges [76]. Charges trapped by these centers are released with a time delay which leads to the effect that not all charges produced by a traversing particle are registered in the amplifier. It has been shown that the mobility of both charge carriers decreases with increasing fluence due to these trapping-detrapping effects causing longer current pulses.

This effects leads to the slower increase of the registered signal with V_{od} . However, sufficient V_{od} leads to the same signal height as registered on a non-irradiated detector.

Shown in figure 4.46 are the S/N peak values at different bias voltages. The S/N ratio increases slowly until it levels off at 14:1 at around 350 V. Similar to the non-irradiated detector the S/N ratio increases after full depletion. This increase appears to be slower than on detector p20 and can be attributed to the slower signal increase as shown in figure 4.45 and a slight increase in noise which is due to increased shot noise from the detector leakage current, as can be seen in figure 4.47.

The same fit has been applied to the data points above depletion as shown in figure 4.29. The fit is described as

$$a \cdot (1 - \text{RBD})$$

where RBD is depending on the maximum collection time. The drift velocity v_h is directly proportional to the mobility of holes which is degraded by radiation. The anti-annealing leads to an increase of N_{eff} , which leads to a change of the electric field. Thus the two parameters v_h and E_{max} were left floating while ‘a’ was fixed to 14.2 which corresponds to the S/N ratio at 480 V. The fit parameters obtained are $v_h = 14447 \pm 3510$ m/s

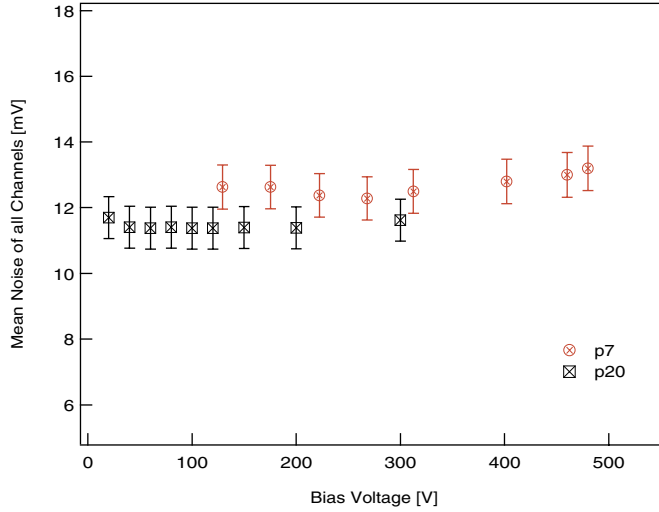


Figure 4.47: Mean noise of all channels at different bias voltages.

and $E_{max}=806.4\pm 393.0$ kV/cm. The χ^2 of the fit is 7.9/3. As the collection time is expressed as a function of over depletion V_{fd} was set to 220 V for the fit. The large errors of the fitted parameters reflect the correlation between drift velocity and the maximum electric field. Calculating the hole mobility from the fitted values yields $\mu_h \approx 179$ cm²/Vs. Leroy et al. have observed a decrease of the hole mobility of $\approx 1.6\%$ per 10^{13} 1 MeV neutrons/cm² [76]. For a neutron fluence of 2.1×10^{14} n/cm² (corresponding to the 3×10^{14} protons/cm²) one therefore expects a decrease of about 34%. Assuming an initial hole mobility of 480 cm²/Vs, the calculated value of 179 cm²/Vs corresponds to a decrease of 63%. Taking into account the large errors of v_h and E_{max} only a qualitative analysis is possible. The data from the irradiated detector can be fitted in the same way as the data from detector p7, indicating that the evolution of the S/N ratio of the over depleted detector increases as $a \cdot (1 - RBD)$, where RBD depends on the maximum collection time. However, the intrinsic parameters of μ_h and E_{max} have changed significantly which can be attributed to the radiation induced damage.

Figure 4.47 illustrates the mean noise as a function of bias voltage for detectors p7 and p20. The noise is almost constant over the full measurement range and has thus no influence on the form of the S/N curve shown in figure 4.46.

Compared to detector p20 the S/N ratio has decreased from 17:1 to 14:1. Assuming that the ¹⁰⁶Ru source emits only MIPs which produce 22500 e-h pairs, a S/N of 17:1 corresponds to 1324 ENC. This value is most likely overestimated due to several reasons explained in chapter 4.5.1. In this case

it will only be used for a relative comparison. The S/N ratio of 14.2:1 then corresponds to 1585 ENC. The leakage current of the detector at 460 V is 1.8 μA per channel. The contribution of the detector leakage current is 720 e^- . Assuming an increase of the interstrip capacitance of $\approx 20\%$ (see also chapter 3) the ENC of the irradiated detector is calculated using the following equation [44]:

$$\text{ENC}_{\text{irrad}} = \sqrt{(\text{ENC}_{\text{non-irrad}} + \Delta C(33e^-/pF)) + \text{ENC}_{\text{leak}}^2} \quad (4.28)$$

The ENC of the irradiated detector is therefore calculated to be 1565 e^- . This value is in good agreement with 1585 e^- of the measurement.

The decrease in S/N after irradiation can therefore at high over depletion voltage be accounted for by the increased leakage current and the increase in load capacitance. A signal loss is not visible above $V_{od}=240$ V. Figure 4.48 displays the cluster S/N histograms of the irradiated and the non-irradiated detector at the highest measured bias voltages.

4.7 Conclusions

The silicon detectors in the ATLAS experiment will be operated in a very harsh radiation environment, and have to be read out using fast frontend electronics. To account for the high occupancy expected in silicon strip detectors and parallel noise increase from leakage current after irradiation readout electronics with around 25 ns peaking time has to be used. This is in the order of typical charge collection times in 300 μm silicon detectors.

A simple model describing the charge collection in silicon as a function of over depletion V_{od} [52] is presented and the induced current and charge is calculated using ATLAS detector parameters. These results illustrate that only at voltages much bigger than V_{od} the typical charge collection time becomes much shorter than 25 ns. Values of V_{od} of 100 V and more are necessary to decrease the collection time to less than 10 ns.

If the charge collection time is in the order of the peaking time of the shaper response of the readout electronics not all the charge is registered in the amplifier due to ballistic deficit. An exact solution for a CR-RC shaper developed by [61] is presented.

Source tests are carried out using an ATLAS prototype detector and fast frontend electronics developed for LHC. The SCT32A chip is an analog frontend chip with 25 ns peaking time. The source tests have shown that the readout trigger has to be accurately timed with respect to the 40 MHz clock of the chip in order to readout at the peak of the pulse. Delayscans are carried out at different bias voltages of the detector showing the evolution of the convolution of the current pulse and the shaper response. The S/N ratio is measured at optimum trigger delay as a function bias voltage. The

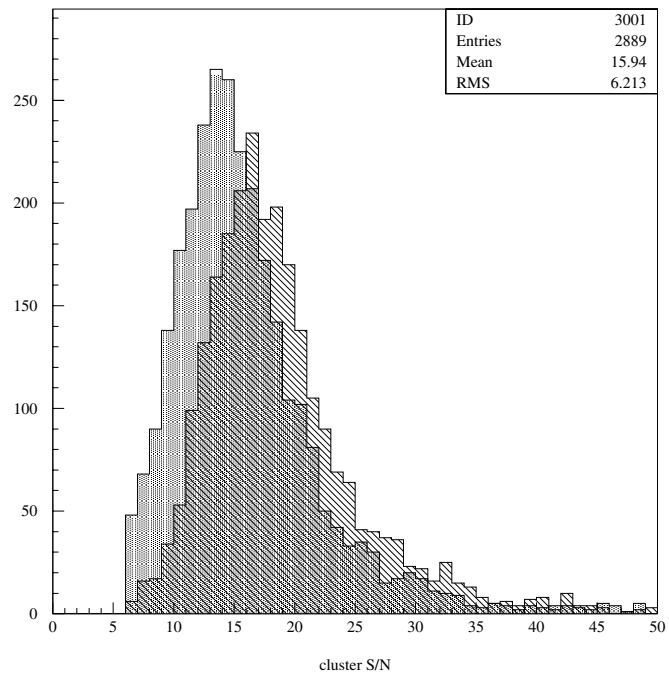


Figure 4.48: Cluster S/N histograms of detector p20 at 300 V and detector p7 at 480 V. The measurement of detector p7 contains 5000 events more which leads to more entries in this histogram.

ballistic deficit is calculated according to the definition given in section 4.1.2. A general approximation of the relative ballistic deficit (RBD) developed by [72] and further discussed by [61] is combined with the description of the charge collection time given in chapter 4.1. In this way it is possible to model the RBD as a function of charge collection time and furthermore as a function of over depletion. The data taken in the source tests are in good agreement with this description. An important consequence of these results is that using LHC electronics the detector has to be almost hundred percent over depleted in order to suppress the ballistic deficit.

A testbeam carried out with the non-irradiated prototype detector and the SCT32A used for the source tests showed the excellent performance of this module. A S/N of 21:1 could be obtained, corresponding to an ENC of 1176 e⁻. This value is in very good agreement with the calculated ENC taking into account channel noise and leakage current contributions. The analysis shows that mainly one-strip hits are registered. This is reflected in the resolution which is found to be in the order of the binary resolution. Analysis of the two-strip hits shows that hits on two adjacent strips due to charge diffusion only occur for tracks which hit in the middle between the strips in a $\pm 10 \mu\text{m}$ wide region.

Source tests are also carried out using an irradiated prototype detector. This detector was annealed over 18.3 days at 25 °C and thus has reached approximately the amount of anti-annealing expected after 10 years of LHC (compare results presented in chapter 3). The measurements are carried out in a freezer at ≈ -6 °C, which is close to the foreseen ATLAS operational temperature at -7 °C. The S/N as a function of bias voltage shows a similar behaviour as before irradiation reflecting the ballistic deficit. At high V_{od} the lower S/N than before irradiation can be attributed to the higher leakage current, while at lower V_{od} additional charge loss is observed. Possibly this can be accounted for to by trapping of charges by radiation induced defects.

The results from a testbeam using binary electronics show that the efficiency of p-in-n detectors decreases below depletion, while n-in-n detectors maintain high efficiency. The SINTEF p-in-n detector in the binary testbeam reaches a plateau in efficiency at about 200-250 V. This is consistent with the results from the source tests where the irradiated SINTEF detector reaches a plateau in charge collection efficiency above 300 V bias.

The full functionality of an irradiated and annealed ATLAS prototype detector using LHC analog electronics (not irradiated) at ATLAS operational temperature could be shown. Attention has to be paid to the degrading effect of the ballistic deficit. By substantially over depleting the detector the ballistic deficit can be decreased. However, for highly damaged detectors with a depletion voltage of a few hundred volts this will lead to an even higher operational voltage thus enforcing the negative side-effects of operation at high voltages, such as breakdown and cooling requirements.

Appendix A

Basic Properties of Silicon Detectors

In a silicon crystal each atom forms *covalent bonds* with its four nearest neighbours by sharing the four electrons in its outermost shell. At low temperatures all the electrons participate in the covalent bonding and are not available for conduction. At higher temperatures thermal vibrations can break up covalent bonds and the freed electrons can participate in conduction. Electrons are then missing in the bonds which can be filled by neighbouring electrons, resulting in a transfer of the electron deficiency to another bond. This deficiency is referred to as a hole and can be regarded as a positive charge [13]. Displayed in Figure A.1 is the position of silicon atoms in the unit cell of the crystal and a schematic drawing of the covalent bond between a silicon atom and its four neighbours.

The energy levels of the electrons are split into two levels, forming two energy bands separated by a forbidden gap. The upper band is referred to as the conduction band and the lower to as the valence band. The band gap E_g is actually used to classify solids into insulators, semiconductors and conductors. Semiconductors such as silicon take an intermediate place between insulators, where the conduction band is separated from the valence band by a large gap (~ 9 eV), and conductors, where the bands are either overlapping, or the valence band is partially filled. At room temperature the band gap energy of silicon is 1.12 eV [13]. However, the energy needed to move an electron from the valence band to the conduction band is about three times larger than the band gap energy. An average energy of 3.6 eV is needed where about two thirds of it is used for exciting lattice vibrations.

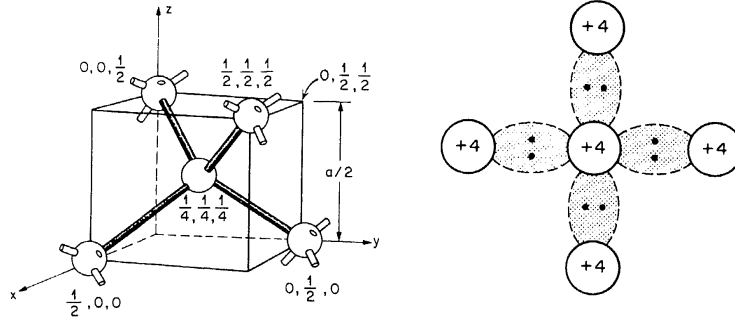


Figure A.1: Unit cell of a silicon lattice and schematic drawing of the covalent bond of one silicon atom to its nearest neighbours [13].

A.1 Intrinsic and Doped Silicon

In intrinsic silicon the amount of impurities is small compared to the thermally generated electrons and holes. Thermal excitation depends on the band gap energy and the temperature. The probability that an electronic state with energy E is occupied by an electron is described by the Fermi-Dirac distribution, see equation A.1.

$$F(E) = \frac{1}{1 + \exp((E - E_f)/kT)} \quad (\text{A.1})$$

k is the Boltzmann constant and T the absolute temperature. E_f is the Fermi-level at which the probability of occupation by one electron is exactly one half. Using the Fermi-Dirac distribution and the density of allowed energy states per unit volume, the density of electrons (n) is given by A.2 and the density of holes (p) in the valence band by A.3, respectively.

$$n = N_C \exp(-(E_C - E_f)/kT) \quad (\text{A.2})$$

$$p = N_V \exp(-(E_f - E_V)/kT) \quad (\text{A.3})$$

E_C is the lowest energy in the conduction band and E_V is the highest energy in the valence band. N_C and N_V denote the effective densities of

states in the conduction band and the valence band. In equilibrium the electron density is equal to the hole density, $p=n=n_i$, where n_i is called the intrinsic carrier density.

The Fermi level for intrinsic silicon is generally very close to the middle of the band gap. The intrinsic carrier concentration can then be described as, [13]:

$$n_i = \sqrt{N_c N_v} \exp(-E_g/2kT) \quad (\text{A.4})$$

The intrinsic carrier concentration of silicon at room temperature is $1.45 \times 10^{10} \text{ cm}^{-3}$. Noting that there are about $10 \times 10^{22} \text{ atoms cm}^{-3}$ in silicon, this leads to approximately every 10^{12} th silicon atom to be ionised [14]. Thus the concentration of free carriers is relatively low. Figure A.2 (a) shows a schematic drawing of the band structure of intrinsic silicon.

To increase the number of free charge carriers silicon can be doped with impurity atoms. The lattice atoms are replaced with the impurity atoms which then form covalent bonds with the neighbouring atoms. In the case of phosphorus doped silicon four of the five phosphorus valence atoms are bound in covalent bonds, the fifth is only loosely bound. Impurity atoms with more valence electrons than the semiconductor atoms are referred to as *donors*. The silicon becomes *n-type* due to the surplus of negative charge carriers. The donor introduces an energy level very close to the conduction band. The loosely bound electron can be moved to the conduction band easily by thermal excitation leaving an ionised phosphorus atom. At room temperature all donors are ionised and thus the electron density n is equal to the concentration of donors N_D .

Similarly, if a silicon atom is replaced by a boron atom with only three valence electrons, the silicon becomes *p-type*. One electron is now missing in the covalent bonds to the neighbours and a hole is created. An energy close to the valence band is introduced which can be filled with a thermally excited electron. A hole is then created in the valence band and the impurity atom becomes negatively charged. Atoms with less valence electrons than the semiconductor are referred to as *acceptors*. At room temperature the acceptor atoms are completely ionised and the concentration of holes p is equal to the acceptor concentration N_A .

In Figure A.2 (b) and (c) the energy levels of n-doped and p-doped silicon are schematically displayed. Note that the Fermi level is shifted to the conduction band for n-type silicon and to the valence band for p-type silicon.

The resistivity of silicon ρ , depends on the concentration of free charge carriers and their mobilities, μ_e and μ_h .

$$\rho = \frac{1}{q(\mu_e n + \mu_h p)} \quad (\text{A.5})$$

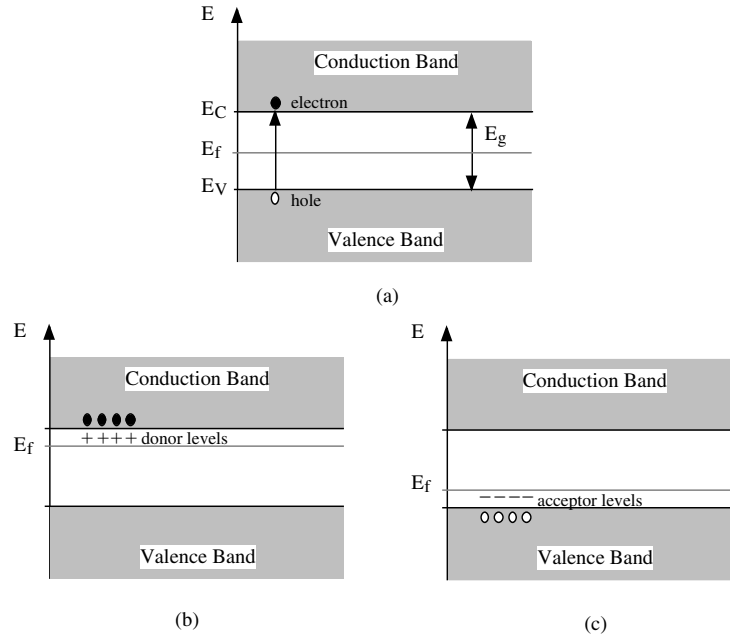


Figure A.2: Schematic illustration of the energy levels in intrinsic (a), n-doped (b) and p-doped (c) silicon.

Intrinsic silicon has a resistivity of about 235 k Ω cm. The resistivity of detector grade silicon varies between 4 and 6 k Ω cm.

If no electric field is applied the charges will be moving randomly in all directions resulting in a zero net displacement over long enough times. If an electric field is applied to the semiconductor the carriers motion will be a combination of thermal motion and the drift along the electric field lines. At low electric fields the drift velocity is proportional to the applied field both for electrons and holes. The proportionality constant is called the mobility. For intrinsic silicon at room temperature the mobility of electrons μ_e is 1350 cm²/Vs and for holes μ_h 480 cm²/Vs. μ_e and μ_h are constant for fields less than a few kV/cm. At high fields the drift velocity saturates at a value of about 10⁷ cm/s and becomes independent of further increasing the field. Due to the high mobility the time needed to collect the charge in a typical well depleted silicon detector of 300 μ m thickness is in the order of 8 ns for electrons and 25 ns for holes [11]. A more detailed discussion on the charge collection can be found in chapter 4.

A.2 The p-n Junction

A p-n junction is created by combining p-doped silicon with n-doped silicon. Depending on the production one can distinguish between abrupt and graded junctions. In abrupt junctions the transition between p and n-type material is sharp as for example in epitaxially grown junctions. In graded junctions the transition between p and n-type is occurring slowly over many atomic spacings as for example in thermally diffused junctions [77].

The large carrier concentration gradients at the junction causes charge carrier diffusion. Electrons diffuse into the p-doped silicon and holes diffuse into the n-doped silicon. The diffusing carriers recombine with their counterparts leaving space charges in the diffusion region. This leads to an electric field which counteracts the diffusion and eventually halts the process. The corresponding potential is called the built in voltage V_{bi} . The space charge region is referred to as the depleted region due to the absence of free charge carriers. Furthermore any charge entering this zone will be moved out by the electric field. To ensure a continuous transition of energy bands between p and n material the band structure must be bent. In figure A.3 a sketch of a p-n junction and its energy levels is displayed.

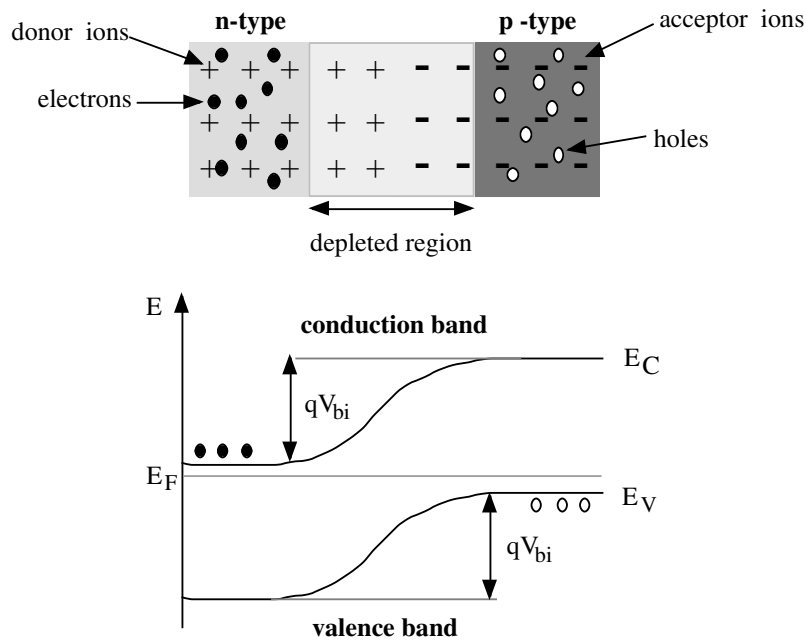


Figure A.3: Schematic sketch of a p-n junction and its energy levels.

In the case of an abrupt junction formed between a p-layer and an n-bulk, Poissons equation simplifies to

$$\frac{d^2V}{dx^2} = \frac{dE}{dx} = +\frac{qN_A}{\epsilon_S} \text{ for } -x_p \leq x < 0 \quad (\text{A.6})$$

$$\frac{d^2V}{dx^2} = \frac{dE}{dx} = -\frac{qN_D}{\epsilon_S} \text{ for } 0 < x \leq x_n. \quad (\text{A.7})$$

x_p and x_n are the depletion regions extending into the p and the n-region, respectively. The total depletion width W is given by the sum of x_p and x_n . ϵ_S is the product of the relative permittivity of silicon and the permittivity of vacuum. By integrating A.6 and A.7 one obtains the electric field.

$$E(x) = \frac{-qN_A(x + x_p)}{\epsilon_S} \text{ for } -x_p \leq x < 0 \quad (\text{A.8})$$

$$E(x) = \frac{qN_D(x - x_n)}{\epsilon_S} \text{ for } 0 < x \leq x_n. \quad (\text{A.9})$$

The maximum field exists at $x=0$ and is given by equation A.10. The built-in voltage V_{bi} can be obtained by integrating equations A.8 and A.9, and using equation A.11 [13].

$$E_{max} = \frac{qN_D x_n}{\epsilon_S} = \frac{qN_A x_p}{\epsilon_S}. \quad (\text{A.10})$$

$$V_{bi} = \frac{1}{2} E_{max} W \quad (\text{A.11})$$

A schematic view of the abrupt p-n junction and the distributions of the doping concentration and the electric field is given in figure A.4. The difference of donor and acceptor concentration, $N_D - N_A$, is called the effective doping concentration N_{eff} .

The extension of the depletion region into the p and the n-type silicon is expressed in equations A.12 and A.13.

$$x_p = \sqrt{\frac{2\epsilon_S V_{bi}}{qN_A(1 + \frac{N_A}{N_D})}} \quad (\text{A.12})$$

$$x_n = \sqrt{\frac{2\epsilon_S V_{bi}}{qN_D(1 + \frac{N_D}{N_A})}} \quad (\text{A.13})$$

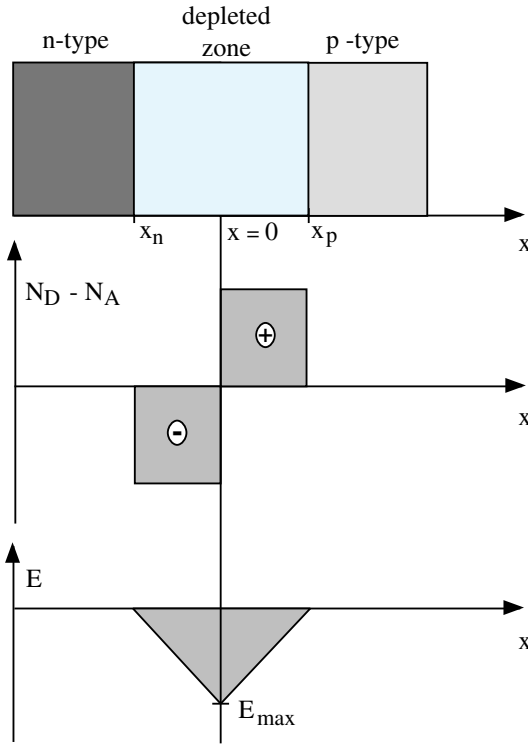


Figure A.4: Doping concentration and electric field of a pn junction.

The above described p-n junction in thermal equilibrium would not provide a sufficient intrinsic field for good charge collection. Furthermore the active volume represented by the depleted volume is too small to collect sufficient charge from ionisation by high energetic particles traversing the detector. The depletion width can be changed by applying an external voltage, which also changes the electric field.

As an example the most common type of silicon detectors is based on a junction formed between a thin highly p-doped (p^+) layer and an n-doped bulk. The depletion region extends much further into the n-side than into the p-side, according to equation A.12 and A.13. The depletion width W is approximated by x_n and W can be expressed for an external bias applied to be

$$W = \sqrt{\frac{2\epsilon_S(V_{ext} - V_{bi})}{qN_D}}. \quad (\text{A.14})$$

The depletion width varies with the square root of the applied voltage. Applying a negative voltage V_{ext} to the p-side, the junction becomes *forward*

biased. The potential across the junction is now $V_{bi}-V_{ext}$ and thus the depletion region decreases. This is referred to as forward biasing of the junction.

When *reverse biasing* the junction a positive voltage is applied to the n-side with respect to the p-side. The total potential is increased by the external potential and thus the depletion region will increase according to equation A.14. If sufficient bias is applied the whole bulk volume can be depleted. The voltage needed to fully deplete the silicon is called the *full depletion voltage* V_{fd} .

$$V_{fd} = \frac{e}{2\epsilon_S} N_{eff} d^2 \quad (\text{A.15})$$

In figure A.5 the depletion width for a pn junction with and without external bias is displayed. Note that for the p^+ -n junction the depletion region extends further into the n-bulk material than into the p^+ side.

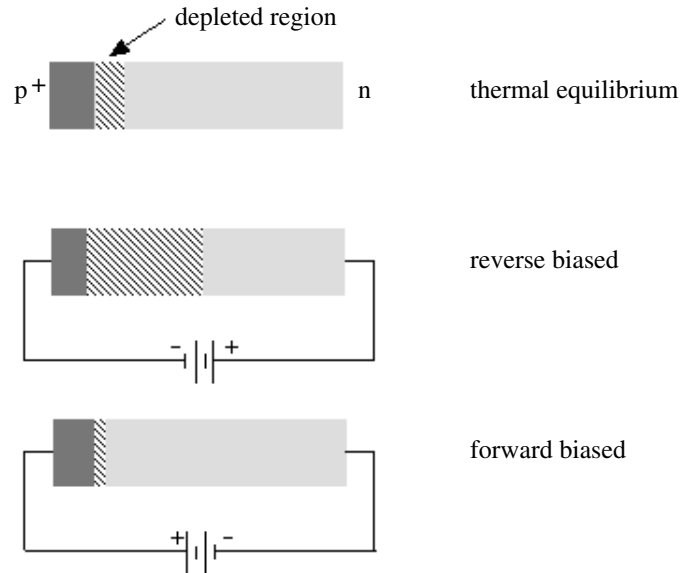


Figure A.5: Schematic of the depletion width for thermal equilibrium and applied bias.

Appendix B

Source Tests with Small Test Detectors

As well as the measurements on ATLAS prototype detectors described in chapter 4, measurements were carried out on small test detectors using the SCT32A. The detectors were produced together with the ATLAS detectors by SINTEF. Their strip pitch is $50\ \mu\text{m}$ and the strips are 1 cm long. One detector (p16) was irradiated in T7 under the same conditions as the full size detectors to a fluence of $3 \times 10^{14}\ \text{p}/\text{cm}^2$. It was then annealed for 21 days at $25\ \text{°C}$ before being connected to an SCT32A. A second detector (p24) was measured non-irradiated.

Displayed in figure B.1 are the total I-V curves of detector p16 and p24. The measurements were carried out after the detectors were connected to the chips.

Both detectors were tested in the same source-setup as the prototype detectors described in chapter 4. Figure B.2 displays the mean cluster signal as a function of trigger delay. Comparing this figure with figure 4.41 shows a very similar behaviour. C-V measurements could not be carried out on the mounted detector. From the Zioc parameterisation for this fluence and an annealing temperature of $25\ \text{°C}$ an increase of V_{fd} between 18 days and 21 days of annealing of $\approx 5\%$ is expected. Compared to detector p7 one expects therefore a V_{fd} of approximately 230-260 V. The trigger delay scans above this estimated V_{fd} show an increasing slope on the right-hand side, similar to the ones on detector p7. At the two highest voltages the delay scan shows a steep slope of around 20-30 ns.

Figure B.3 shows the S/N as a function of bias voltage for detectors p16 and p24 at optimum trigger delay. The behaviour is very similar to that of the full size detectors shown in figure 4.29 and 4.46. As observed there, the S/N increases even beyond V_{fd} . While for the non-irradiated detector the S/N seems to level off at high voltages, it continues to increase slowly for

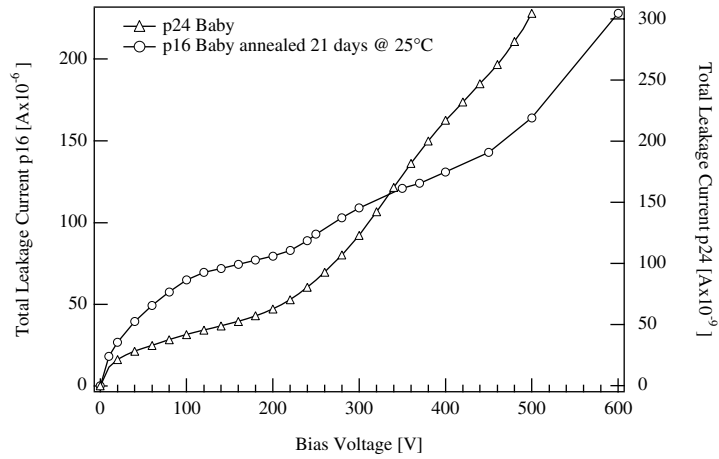


Figure B.1: Total leakage current of detectors p16 and p24. for the annealed detector the current increases to hundreds of μA , while for detector p24 the current is nA.

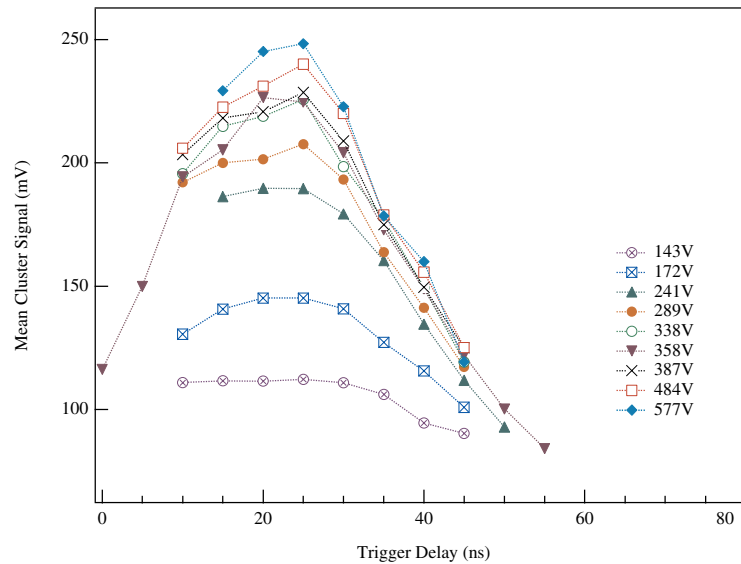


Figure B.2: Delay scans of detector p16 at different bias voltages.

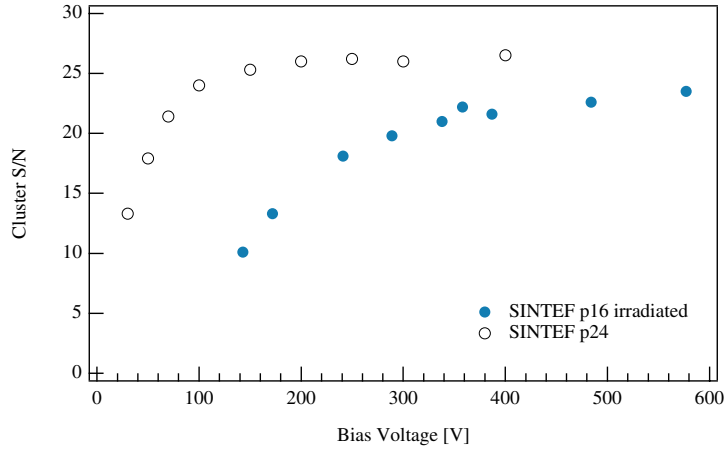


Figure B.3: Cluster S/N as a function of bias voltage for detectors p16 and p24. The errors on the data are of the size of the markers.

the irradiated detector.

Finally, in figure B.4 are shown the S/N of the full size prototype detector p7 and of the baby detector p16 as a function bias showing the similar behaviour. The baby detector could be measured to higher bias voltages due to the smaller overall leakage current. The errors on the points are of the size of the markers.

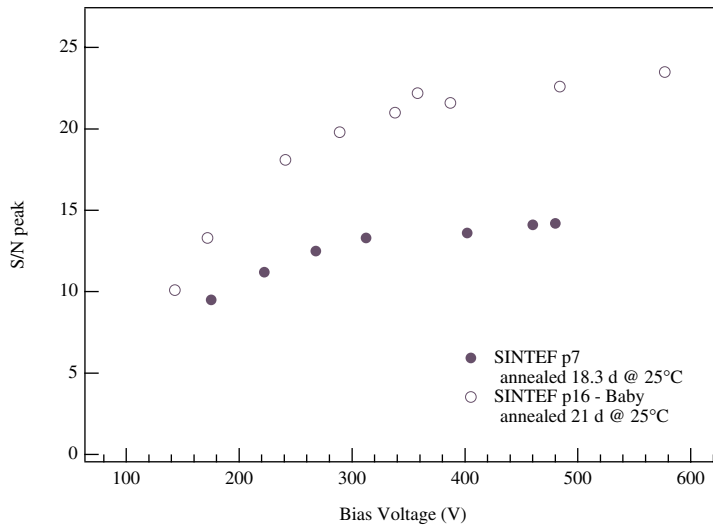


Figure B.4: Cluster S/N as a function of bias voltage of the two irradiated detectors.

Bibliography

- [1] *Technical Proposal for CMS*, 1995. 1.1, 1.3
- [2] *ATLAS Technical Proposal*, 1994. 1.1
- [3] N.V. Krasnikov and V.A. Matveev. Physics at LHC. *INR RAS*, 117312, 1997. 1.1, 1.1
- [4] H.J. Hilke and T. Nakada. *Presentation of the Technical Proposal for LHC-B to the LHCC*, 1998. 1.1, 1.3
- [5] *ALICE Technical Proposal*, 1997. 1.1, 1.3
- [6] P. Weilhammer. Double-sided Si strip sensors for LEP vertex detectors. *Nuclear Instruments and Methods A*, 117312, 1997. 1.2, 1.3, 2.3.1, 2.3.1
- [7] C. Colledani, W. Dulinski, R. Turchetta, F. Djama, A. Rudge, and P. Weilhammer. A submicron precision silicon telescope for beam test purposes. *Nuclear Instruments and Methods A*, 372:379–384, 1996. 1.2, 4.5.2, 4.5.2
- [8] *ATLAS Inner Detector Technical Design Report*, 1997. 1.3, 1.2, 1.3, 3.3.2, 3.1, 3.5.1, 3.5.1, 3.5.3, 3.5, 3.5.4, 4.2
- [9] G. Gorfine and G. Taylor. Particle fluxes and damage to silicon in the ATLAS inner detector. *ATLAS-INDET Note*, 30, 1993. 1.3
- [10] S. Sotthibandhu. *Radiation Damage Studies of Silicon Detectors*. PhD thesis, Imperial College London, 1994. 1.3
- [11] R.M. Barnett et al. Review of particle physics. *Physical Review*, D54, 1996. 1.3, 4.1, A.1
- [12] A. Van Ginneken. Non ionizing energy loss deposition in silicon for radiation damage studies. *Fermi National Accelerator Note*, 522, 1989. 1.3
- [13] S.M. Sze. *Semiconductor Devices*. John Wiley and Sons, 1985. 2.1, 2.1, 2.1, 2.2, A, A, A.1, A.1, A.2

- [14] W.R. Leo. *Techniques for Nuclear and Particle Physics Experiments*. Springer-Verlag, 1987. 2.1, 4.1, A.1
- [15] A. Peisert. Silicon microstrip detectors. *DELPHI Note*, 143, 1992. 2.2, 2.3.1, 4.1.3
- [16] G. Hall, D. Vite, and R. Wheadon. Calculation of the geometrical capacitance of silicon microstrip structures using a variational approach. *Nuclear Instruments and Methods A*, 326:228–233, 1993. 2.2, 4.5
- [17] J. Kemmer. Fabrication of low noise silicon radiation detectors by the planar process. *Nuclear Instruments and Methods*, 169:499–502, 1980. 2.3.1
- [18] P.P. Allport, J.R. Carter, V. Gibson, M.J. Goodrick, J.C. Hill, S.G. Katvars, M.A. Bullough, N.M. Greenwood, A.D. Lucas, C.D. Wilburn, A.A. Carter, T.W. Pritchard, L. Nardini, P.Seller, and L.S. Thomas. FOXFET biased microstrip detectors. *Nuclear Instruments and Methods A*, 310:155–159, 1991. 2.3.1
- [19] M. Laasko, P. Singh, E. Engels, and P.F. Shepard. Operation and radiation resistance of a FOXFET biasing structure for silicon strip detectors. *Nuclear Instruments and Methods A*, 326:214–221, 1993. 2.3.1
- [20] N. Bacchetta, D. Bisello, G. Bolla, C. Canali, P.G. Fuochi, and A. Paccagnella. Radiation effects on ac-coupled microstrip silicon detectors. *Nuclear Instruments and Methods A*, 326:381–385, 1993. 2.3.1
- [21] P. Azzi, N. Bacchetta, G. Bolla, D. Glensinski, C. Haber, J. Incandela, E. Kajfasz, M.D. Peters, N.M. Shaw, F.P. Snider, J. Spalding, L. Spiegel, and D. Stuart. Radiation damage experience at CDF with SVX'. *Nuclear Instruments and Methods A*, 383:155–158, 1996. 2.3.1
- [22] L. Evensen, A. Hanneborg, B.S. Avset, and M. Nese. Guard ring design for high voltage operation of silicon detectors. *Nuclear Instruments and Methods A*, 337, 1993. 2.3.1
- [23] G.A. Beck, A.A. Carter, J.R. Carter, N.M. Greenwood, A.D. Lucas, D.J. Munday, T.W. Pritchard, D. Robinson, C.D. Wilburn, and K.H. Wyllie. Radiation-tolerant breakdown protection of silicon detectors using multiple floating guard rings. *Nuclear Instruments and Methods A*, 396:214–227, 1997. 2.3.1
- [24] S. Roe and P. Weilhammer. Feasibility of Si strip detectors with capacitive charge division and deconvolution front-end electronics in the ATLAS Si tracker. *ATLAS-INDET Note*, 41, 1994. 2.10

- [25] H. Feick. *Radiation Tolerance of Silicon Particle Detectors for High Energy Physics Experiments*. PhD thesis, University of Hamburg, 1997. 3, 3.4, 3.4.1, 3.1, 3.4.1, 3.5.4
- [26] E. Fretwurs, H. Feick, M. Glaser, C. Goessling, E.H.M. Heijne, A. Hess, F. Lemeilleur, G. Lindstroem, K.H. Maehlmann, A. Rolf, T. Schulz, and C. Soave. Reverse annealing of the effective impurity concentration and long term poerational scenario for siliocn detectos in future collider experiments. *Nuclear Instruments and Methods A*, 342:119–125, 1994. 3, 3.7, 3.4.1
- [27] H.J. Ziock, K. Holzscheiter, A. Morgan, A.P.T. Palounek, J. Ellison, A.P. Heinson, M. Mason, S.J. Wimpenny, E. Barberis, N. Cartiglia, A. Grillo, K. O’shaughnessy, J. Rahn, P. Rinaldi, W.A. Rowe H.F.-W. Sadrozinski, A. Seiden, E. Spencer, A. Webster, R. Wichmann, M. Wilder, M.A. Frautschi, J.A.J. Matthews, D. MacDonald, D. Skinner, D. Coupal, and T. Pal. Temperature dependence of the radiation induced change of depletion voltage in silicon pin detectors. *Nuclear Instruments and Methods A*, 342:96–104, 1994. 3, 3.4, 3.4.2, 3.5.3, 3.5.3, 3.8, 3.5.4
- [28] R. Wunstorf. *Systematische Untersuchungen zur Strahlenresistenz von Silizium Detektoren für die Verwendung in Hochenergiephysik-Experimenten*. PhD thesis, Universität Hamburg, 1992. 3.1, 3.1, 3.2, 3.3, 3.3.1, 3.5.3, 3.5.3
- [29] G.P. Mueller, N.D. Wilsey, and M. Rosen. The structure of displacement cascades in silicon. *IEEE Transactions on Nuclear Science*, NS-29:1493–1497, 1982. 3.1, 3.1
- [30] The ROSE collaboration. RD48 status report. *CERN/LHCC*, 39, 1997. 3.3.1, 3.3.2, 3.6, 3.4.1, 3.5.4
- [31] D. Pitzl, N. Cartiglia, B. Hubbard, D. Hutchinson, J. Leslie, K. O’Shaughnessy, W. Rowe, H.F.-W. Sadrozinski, A. Seiden, E. spencer, H.J. Ziock, P. Ferguson, K. Holzscheiter, and W.F. Sommer. Type inversion in silicon. *Nuclear Instruments and Methods A*, 311:98–104, 1992. 3.3.2
- [32] G. Davies et al. A model for radiation damage effects in carbon-doped crystalline silicon. *Semiconductor Science Technology*, pages 524–532, 1987. 3.3.2
- [33] B. MacEvoy, G. Hall, and K. Gill. Defect evolution in irradiated silicon detector material. *IC/HEP Imperial College*, 8, 1995. 3.3.2
- [34] B.C. MacEvoy. Investigations using a simple model for defect kinetics in silicon. *RD20 Technical Note*, 41, 1995. 3.3.2

- [35] RD20 Collaboration. Radiation tolerance of single sided silicon microstrips. *CERN-PPE*, 137, 1993. 3.3.3, 3.3.4
- [36] H.J. Ziock, C. Milner, W.F. Sommer, N. Cartiglia, J. DeWitt, D. Dorfman, B. Hubbard, J. Leslie, K.F. O'Shaughnessy, D. Pitzl, W.A. Rowe, H.F.-W. Sadrozinski, A. Seiden, E. Spencer, P. Tennenbaum, J. Ellison, S. Jerger, C. Lietzke, S.J. Wimpenny, P. Ferguson, and P. Giubellino. Tests of the radiation hardness of VLSI integrated circuits and silicon strip detectors for the SSC under neutron, proton and gamma irradiation. *IEEE Transactions on Nuclear Science*, 38, 1991. 3.3.5
- [37] A. Chilingarov. Presentation in ATLAS SCT week 01/1998. 3.4.2, 3.5.3, 3.5.4
- [38] SINTEF, Forskningsveien 1, PO Box 124 Blindern, N-0314 Oslo. 3.5.2
- [39] C.Furetta et al. Fluence and dosimetric measurements for π^\pm irradiation facility. *CERN - ECP/95-2*, 1995. 3.5.2
- [40] F. Lemeilleur, S.J. Bates, A. Chilingarov, C. Furetta, M. Glaser, E.H.M. Heijne, P. Jarron, C. Soave, C. Leroy, and I. Trigger. Study of characteristics of silicon detectors irradiated with 24 GeV protons between -20°c and $+20^\circ\text{c}$. *Nuclear Instruments and Methods A*, 360, 1995. 3.5.2
- [41] H.F.-W. Sadrozinski. Annealing of irradiated SCT detectors. *Presentation at the ATLAS SCT Week*, September, 1997. 3.5.3
- [42] Z. Li and H.W. Kraner. Studies of frequency dependent C-V characteristics of neutron irradiated p^+ -n silicon detectors. *IEEE Transactions on Nuclear Science*, 38:244–250, 1991. 3.5.3
- [43] L. Beattie, A. Chilingarov, P. Ratoff, and T. Sloan. Dependence of depletion voltage and capacitance on temperature and frequency in heavily irradiated silicon diodes. *ROSE Technical Note*, 97-4, 1997. 3.5.3, 3.5.3
- [44] V. Cindro, G. Kramberger, M. Mikuz, D. Zontar, J. Kaplon, P. Riedler, S. Roe, P. Weilhammer, and W. Dabrowski. Readout of non irradiated and irradiated strip detectors with fast analog electronic, 1998. 3.5.3, 4.6
- [45] F. Lemeilleur. Private communications, 1997. 3.5.3
- [46] W.H. Press. *Numerical Recipes in C*. Cambridge University Press, 2nd edition, 1992. 3.5.3
- [47] D. Morgan, P. Riedler, P.P. Allport, C.M. Buttar, J.R. Carter, M. Hanlon, G. Lutz, C. Raine, R.H. Richter, D. Robinson, S. Roe, T. Rohe,

- H.F.-W. Sadrozinski, S. Stapnes, Y. Unno, and P. Weilhammer. Annealing study of irradiated ATLAS prototype silicon microstrip detectors. *ATLAS-INDET Note*, 199, 1998. 3.5.4
- [48] P. Riedler, D. Morgan, P.P. Allport, C.M. Buttar, J.R. Carter, M. Hanlon, G. Lutz, C. Raine, R.H. Richter, D. Robinson, S. Roe, T. Rohe, H.F.-W. Sadrozinski, S. Stapnes, Y. Unno, and P. Weilhammer. Analysis of irradiated and annealed ATLAS prototype silicon detectors. *ATLAS-INDET Note*, 209, 1998. 3.5.4
- [49] D. Morgan, P. Riedler, P.P. Allport, C.M. Buttar, J.R. Carter, D. Robinson, S. Roe, T. Rohe, H.F.-W. Sadrozinski, S. Stapnes, Y. Unno, and P. Weilhammer. Annealing of irradiated silicon strip detectors for the ATLAS experiment at CERN. *submitted to Nuclear Instruments and Methods, A*, 1998. 3.5.4
- [50] E. Gatti and P.F. Manfredi. *Processing the Signal from Solid State Detectors in Elementary Particle Physics*. La Rivista Del Nuovo Cimento della Societa Italiana di Fisica, 1986. 4.1
- [51] C. Damerell. Applications of silicon detectors in high energy physics and astrophysics. *Nuclear Instruments and Methods*, 226:26–33, 1984. 4.1
- [52] W. Snoeys. *A New Integrated Pixel Detector for High Energy Physics*. PhD thesis, Stanford, 1992. 4.1, 4.7
- [53] P. Horowitz and W. Hill. *The Art of Electronics*. Cambridge University Press, 1989. 4.1.1
- [54] P.F. Manfredi and F. Ragusa. Low noise electronics in elementary particle physics. *Nuclear Instruments and Methods A*, 235, 1985. 4.1.1, 4.1.1
- [55] F. Anghinolfi, W. Dabrowski, E. Delagnes, J. Kaplon, U. Koetz, P. Jarron, F. Lugiez, C. Posch, S. Roe, and P. Weilhammer. SCTA- a rad-hard BiCMOS analogue readout ASIC for the ATLAS semiconductor tracker. *IEEE Transactions on Nuclear Science*, 44:298–302, 1997. 4.1.1, 4.4, 4.19
- [56] V. Radeka. Semiconductor position-sensitive detectors. *Nuclear Instruments and Methods A*, 226, 1984. 4.1.1
- [57] E. Nygard. *ASICs and Electronic Systems for Readout of Radiation-sensitive Semiconductor Detectors*. PhD thesis, University of Oslo, 1996. 4.1.1

- [58] H. Spieler. Presentation. *SLAC B-Factory Detector Meeting*, 1993. 4.1.1
- [59] P. Aspell, R. Boulter, A. Czermak, P. Jalocha, P. Jarron, A. Kjensmo, W. Lange, E. Nygard, A. Rudge, O. Toker, M. Turala, H. Von Der Lippe, U. Walz, P. Weilhammer, and K. Yoshioka. CMOS low monolithic frontends for Si strip detector readout. *Nuclear Instruments and Methods A*, 315, 1992. 4.9, 4.1.3, 4.5.1
- [60] C. Posch. *Analog Readout for the ATLAS Semiconductor Tracker*. PhD thesis, University of Technology Vienna, 1998. 4.1.1
- [61] B.W. Loo, F.S. Goulding, and D. Gao. Ballistic deficit in pulse shaping amplifiers. *IEEE Transactions on Nuclear Science*, 35:114–118, 1988. 4.1.2, 4.1.2, 4.5.1, 4.7
- [62] R. Hofmann, R. Klanner, G. Lutz, G. Luetjens, and A. Wylie. High resolution silicon detectors - status and future developments of the MPI/TU-Munich group. *Nuclear Instruments and Methods in Physics Research*, 225:601–605, 1984. 4.1.3, 4.1.3
- [63] J.B.A. England, B.D. Hyams, L. Hubbeling, J.C. Vermeulen, and P. Weilhammer. Capacitive charge division readout with a silicon strip detector. *Nuclear Instruments and Methods*, 185:43–47, 1981. 4.1.3
- [64] U. Koetz, K.U. Poesnecker, E. Gatti, E. Belau, D. Buchholz, R. Hofmann, R. Klanner, G. Lutz, E. Neugebauer, H.J. Seebrunner, A. Wylie, and J. Kemmer. Silicon strip detectors with capacitive charge division. *Nuclear Instruments and Methods A*, 235:481–487, 1985. 4.1.3
- [65] E. Belau, R. Klanner, G. Lutz, E. Neugebauer, H.J. Seebrunner, A. Wylie, T. Boehringer, L. Hubbeling, P. Weilhammer, J. Kemmer, U. Koetz, and M. Riebesell. Charge collection in silicon strip detectors. *Nuclear Instruments and Methods*, 214:253–260, 1983. 4.1.3
- [66] <http://hepunix.rl.ac.uk/atlasbinary/index.html>. 4.12
- [67] W. Dabrowski. Development of readout chips for the ATLAS semiconductor tracker. *Nuclear Instruments and Methods A*, 383:179–188, 1996. 4.3, 4.3.1
- [68] J. Straver, O. Toker, P. Weilhammer, C. Colledani, W. Dulinski, R. Turchetta, and L. Bosisio. One micron spatial resolution with silicon strip detectors. *Nuclear Instruments and Methods A*, 348, 1994. 4.3.1, 4.5.2
- [69] A.R. Alvarez. *BiCMOS Technology and Applications*. Kluwer Academic Publishers, 1989. 4.4

- [70] W. Dabrowski and P. Weilhammer. private communication, 1997. 4.4.1
- [71] M. Morrissey. Rutherford Appelton Laboratory, UK. 4.4.3
- [72] E. Baldinger and W. Franzen. *Advances in Electronics and Electron Physics*. Academic Press, 1956. 4.5.1, 4.5.1, 4.7
- [73] Norway IDE AS, NO-1342 Hovik. 4.5.2
- [74] D. Meier. *CVD Diamond for Particle Detection and Tracking*. PhD thesis, University of Heidelberg, 1998. 4.5.2
- [75] P.P. Allport, L. Andricek, C.M. Buttar, J.R. Carter, L.M. Drage, T. Dubbs, J.C. Hill, M.J. Goodrick, A. Greenall, G. Moorhead, D. Morgan, V. O'Shea, P.W. Philips, C. Raine, P. Riedler, D. Robinson, H.F.-W. Sadrozinski, J. Sanchez, N.A. Smith, S. Stapnes, and Y. Unno. A comparison of the performance of irradiated p-in-n and n-in-n silicon microstrip detectors read out with fast binary electronics (to be published), 1998. 4.6, 4.40
- [76] F. Lemeilleur, M. Glaser, E.H.M. Heijne, P. Jarron, C. Soave, C. Leroy, J. Rioux, P. Roy, M. Siad, and I. Trigger. Charge transport in silicon detectors. *CERN/ECP*, 21, 1993. 4.6, 4.6
- [77] G.W. Neudeck. *The pn Junction Diode*. Addison-Wesley Publishing Company, 1989. A.2

Acknowledgements

In January 1996 I started my PhD in the ATLAS SCT group at CERN. Throughout the following two and a half years I got to know many people to who I am very grateful for their help, encouragement and sympathy. I have spent many wonderful and sometimes very busy hours with them and would like to express my deep appreciation to all of them.

I would like to thank Peter Weilhammer, my group leader at CERN, for offering me the chance to work in his group. I am very grateful for his constant interest, encouragement and help. I learnt from him about the fun one can have with silicon detectors and that they are not always that simple as they might seem.

I am also indebted to Shaun Roe for his help, support and supervision. He generously shared office with me during my stay in the ATLAS SCT group.

Special thanks are dedicated to Alan Rudge for his patient help with electronics problems. I am very grateful for his kindness and help.

I am also very grateful to Jan Kaplon and Wladek Dabrowski for their constant help and advises with the SCTA chip. Jan patiently explained to me the features of the chip and was always helpful when nothing was working.

Carlos Lacasta generously left to me his analysis program and kindly offered me help whenever I encountered problems.

I would like to thank Debbie Morgan from Sheffield University for a great even though sometimes very hectic time we had together when annealing detectors.

In addition I would like to express my appreciation for constant help and support to: Bob Boulter, Craig Buttar, Lars Evensen, Richard Fortin, Maurice Glaser, Sue Holland, Uli Koetz, Francois Lemeilleur, Christoph Posch, Rainer Richter, Steinar Stapnes, Trond Westgaard, ...

Finally, I would like to thank my supervisor in Austria, Prof. Gerald Badurek who constantly encouraged and supported me.

Curriculum Vitae

Mag. Petra Riedler
Bacherplatz 9/8
A-1050 Wien
Austria

- Place and date of birth** Vienna, 26 March 1971
- University education**
- Oct. 1995–Oct. 1998 Doctoral thesis in physics, University of Vienna
 - Oct. 1989–July 1995 Basic courses and master in physics, University of Vienna
 - Oct. 1994–June 1995 Additional courses and labs in nuclear solid state physics, University of Technology, Vienna
 - Oct. 1991–July 1994 Courses and teaching training in physics and mathematics for teachers
 - Oct. 1989–Feb. 1991 1. Studienabschnitt Lehramt Physik/Mathematik. Basic courses in physics and mathematics for teachers
- Qualifications received**
- 5 July 1995 Magister der Naturwissenschaften (Master Degree in Physics) with honours: *Neutron Depolarisation in Ferromagnetic Materials* carried out at the Atomic Institute of Austrian Universities
 - 26 June 1989 Reifeprüfung (A levels) with honours